UNIVERSITY OF SOUTHAMPTON
FACULTY OF PHYSICAL SCIENCES AND ENGINEERING
School of Electronics and Computer Science
Nano Research Group

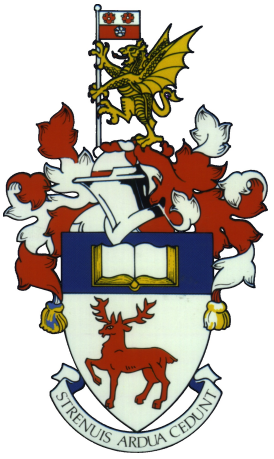

Micro-Sensors Utilising the Mode-Localisation Effect in Electrostatically Coupled MEMS Resonators

by

Graham Stewart Wood

Doctor of Philosophy
April 2016

UNIVERSITY OF SOUTHAMPTON

ABSTRACT

FACULTY OF PHYSICAL SCIENCES AND ENGINEERING
School of Electronics and Computer Science

Doctor of Philosophy

MICRO-SENSORS UTILISING THE MODE-LOCALISATION EFFECT IN ELECTROSTATICALLY COUPLED MEMS RESONATORS

by Graham Stewart Wood

In response to a perturbation, the stiffness or mass of a MEMS resonator can change and previous research has utilised the resonant frequency shift to characterise the perturbation, be it strain or acceleration altering the resonator stiffness or the attachment of a biological element altering the resonator mass. More recently, research has focused on developing MEMS resonator sensors based on the mode-localisation effect, which is the name given to the effect where the mode shapes of an electrostatically coupled system are seen to 'localise' around one of the resonators when the stiffness or mass of one changes. By measuring the change in the mode shape of a coupled system, it is possible to achieve a greater sensitivity to a perturbation than by simply measuring the change in resonant frequency of a one degree-of-freedom system. Building on the previously reported work, the design, fabrication and characterisation of various designs and dimensions of coupled MEMS resonator devices has been performed, with the aim of experimentally determining the influence of the design and dimensions on the device sensitivity. A high-yield dicing-free silicon-on-insulator based process has been used to fabricate electrostatically-coupled MEMS resonator pairs with a thickness of 50 μm. For a design consisting of two 410 μm long rectangular clamped-clamped beams, the sensitivity of the amplitude ratio at the in-phase mode shape has been increased up to 12 times by increasing the beam width from 10 μm to 20 μm. A second design, featuring a larger 310 $\times$ 60 μm rectangular block at the centre of the resonator, has shown a sensitivity up to 3.26 times greater than for the clamped-clamped beams and up to 9 times greater than the state-of-art, with reducing the anchor beam lengths down to 55 μm proving to be critical. Other devices fabricated with an alternative SOI-based process showed stiffness sensitivity up to 46 times greater than the state-of-the-art, but with the drawback that the fabrication process is of a much lower yield. Finally, through removal of up to 3.39 ng of material with a focused ion beam, mass sensing has been demonstrated with a coupled-resonator device, with a 5.4 times greater amplitude ratio response compared to the best value in the literature.

Contents

List of Figures

List of Tables

Declaration of Authorship

I, Graham Stewart Wood, declare that this thesis and the work presented in this thesis are both my own, and have been generated by me as the result of my own original research. I confirm that:

- this work was done wholly or mainly while in candidature for a research degree at this University;
- where any part of this thesis has previously been submitted for a degree or any other qualification at this University or any other institution, this has been clearly stated;
- where I have consulted the published work of others, this is always clearly attributed;
- where I have quoted from the work of others, the source is always given. With the exception of such quotations, this thesis is entirely my own work;
- I have acknowledged all main sources of help;
- where the thesis is based on work done by myself jointly with others, I have made clear exactly what was done by others and what I have contributed myself.

Signed.....

Date.....

Acknowledgements

The production of this Ph.D thesis would not have been possible without the aid of others, and I would like to acknowledge those people here.

Firstly, I would like to thank my supervisor, Michael Kraft, for his direction and encouragement throughout the last four and a half years. Also, I would like to thank Suan Hui Pu for all of his help and guidance and Harold Chong for his advice and support.

Throughout all the work that has been performed to enable this thesis to be written, I have worked closely with my colleague and friend, Chun Zhao, and I am indebted to him for all his effort and help, particularly with regard to helping me understand the background theory and the design of the testing circuitry.

I also acknowledge all the help I received from other academic, research and administrative staff and fellow Ph.D students in the Nano Research Group. In particular, for their help and support with all the numerous problems and challenges that I encountered throughout my studies, I thank Sheng, Chi, David, Tess, Hwanjit, Ali and Ioannis.

The help from all the technicians and process engineers at the Southampton Nanofabrication Centre was invaluable throughout my research work, with Owain Clark and Kian Kiang deserving particular thanks.

I thank Jianbing Xie and Honglong Chang of Northwestern Polytechnical University, Xi'an, China, for their expertise and the production of a batch of devices created using their fabrication process, which allowed for an interesting section of this thesis. Also, I give thanks to Matt Himsworth for his advice regarding the design of the vacuum testing set-up.

Finally, I give thanks to my family, without whose support and encouragement this thesis simply would not have happened.

Chapter 1

Introduction

There are many applications that utilise microelectromechanical systems (MEMS) components. Vibrating microscale structures have been successfully implemented as mixer-filters in RF transceivers [1] and in timing and frequency control [2]. Devices such as gyroscopes, accelerometers, micromirrors, microswitches and pressure sensors have been developed using MEMS for use in applications as diverse as optics, biomedicine, telecommunications and the automotive industry [3, 4]. Quantum mechanical devices and energy harvesting are proposed applications for future MEMS devices [5, 6]. For sensing applications, previous research has shown that mass, force, stress, strain and acceleration can be measured by exploiting the mechanical properties of microscale structures such as cantilevers, bridges and rings, which are typically made of silicon. Thus far, one of the most researched areas of MEMS sensors has been the development of systems that utilise a shift in the resonant frequency to quantify a change in the mechanical properties of a structure. In response to a perturbation, the stiffness or mass of a resonator can change and previous research has utilised the resonant frequency shift to characterise the perturbation, be it strain or acceleration altering the resonator stiffness or the attachment of a biological element altering the resonator mass [7].

The future development of microsensors will focus on increasing their sensitivity. Accelerometers, strain sensors and pressure sensors are examples of sensors that can benefit from improved sensitivity. Ever more sensitive force detection is desired in the field of surface probe microscopy. Another example is biological mass sensors, which require increased sensitivity in order to discriminate between various viruses, bacteria and other pathogens. In addition, MEMS-based sensors are currently being developed that can detect DNA strands [8, 9]. For diagnostic tests at the point of care, faster measurement times are desired, in addition to improved sensitivity. A simple, hand-held device that does not require bulky apparatus and can be used by a person with little or no biomedical training can be realised by utilising MEMS resonators. However, while resonance-shift based sensors have been widely researched and developed, another resonator sensing technique has emerged that utilises two microstructures that are weakly coupled to-

gether with an electric field.

The phenomenon of mode-localisation has been observed previously in arrays of microresonators that are electrostatically coupled [10]. First described in 1958 [11], mode-localisation is the name given to the effect where the mode shapes of a coupled system are seen to "localise" around each of the resonators when an imbalance is introduced. The imbalance can be a change in the mass or the stiffness of one of the resonators. It has been found that, by measuring the change in the mode shape of a coupled system, it is possible to achieve a greater sensitivity to a perturbation than by simply measuring the change in resonant frequency of a one degree-of-freedom system.

The previous research into electrostatically coupled microresonators has proven the theory that a perturbation in the system causes a change in the mode shape. Mass sensing has been demonstrated with microcantilevers that are mechanically, rather than electrostatically, coupled together [12]. In the experiment, a microsphere has been attached to one of a pair of cantilevers and the resulting mode-localisation has been measured successfully. Another study introduced an imbalance into an electrostatically coupled pair of microresonators by applying an additional electrostatic force onto one of the beams, altering its stiffness. The change in mode shape has been measured successfully [10].

Additional advantages of mode-localised sensing over resonant frequency-shift sensing include an inherent common-mode rejection. Any environmental factors that can alter the behaviour of a resonator will affect both resonators in the coupled pair equally. Also, the strength of the electrostatic coupling can be altered by changing the applied bias voltages, allowing for the sensitivity of the device to be controlled in a way that is not possible with a resonant frequency-shift based device, or a mechanically-coupled system.

1.1 Motivation and objectives

This thesis outlines research that exploits the properties of electrostatically coupled microresonators to create ultra-sensitive stiffness and mass sensors. The mode-localisation effect has been used to measure a change in the stiffness or mass of one of a pair of MEMS resonators. The primary motivation of the research presented in this thesis is to improve the sensitivity of the coupled system's mode shape to a stiffness or mass perturbation. Altering the design and dimensions of a coupled resonator device will alter the mode frequencies and the mode shapes, which will influence the sensitivity of the device. This thesis will investigate how changing the design and dimensions can improve device sensitivity.

An additional motivation of the research in this thesis is to utilise a previously reported fabrication process [13] to create coupled MEMS resonators. Previously used to fabricate gyroscopes and accelerometers with large proof masses, the high-yield fabrication process

has been shown to create structures that do not suffer from stiction, where the movable part of the device becomes stuck to a fixed part. The suitability of the process for fabricating smaller coupled MEMS resonator devices will be investigated in this thesis. Comparison will be made to devices fabricated using a different fabrication process [14], in order to determine suitability for producing coupled MEMS resonator devices.

The specific objectives of the research that is presented in this thesis:

- Fabricate a mode-localised sensor based on a pair of electrostatically-coupled MEMS resonators.
- Demonstrate a high-yield (> 90 %) fabrication process to produce coupled resonator devices.
- Optimise the device design and dimensions to improve the relative stiffness change sensitivity and resolution up to the state-of-the-art value.
- Demonstrate mode-localised mass sensing with a sensitivity comparable to the state-of-the-art value, with a minimum detectable value of 10 pg.

1.2 Thesis overview

Chapter 2 contains a review of the current state-of-the-art of MEMS-based sensors. First, sensors based on the static deflection of a MEMS structure will be reviewed briefly. The main focus of the chapter will be on single resonator, one degree-of-freedom systems that quantify the mass or stiffness change of a structure through measurement of the resonant frequency-shift. The theory behind resonant frequency-shift will be detailed along with a review of the previous research. Chapter 3 will detail the technical theory behind the mode-localisation effect in a pair of coupled resonators. A literature review will be presented of previous research into both mechanically and electrostatically coupled MEMS resonator systems and their application as sensors.

Chapter 4 will outline the design and fabrication of the devices, including the microfabrication materials and technologies that have been employed. The silicon-on-insulator based fabrication process employed that promises a high yield will be explained. The additional fabrication process will also be outlined. Several device designs will be presented, with variations in certain dimensions, allowing for the effect on performance to be characterised during testing of fabricated devices. Theoretical calculations have been performed for all of the device designs, showing how the amplitude ratio of the two resonators at the mode frequencies should respond to an imbalance in the mass or stiffness. The fabrication of the devices will be detailed, including the challenges encountered.

Following on from the theoretical calculations, chapter 5 will present the results of finite-element simulations that have been performed using *CoventorWare*, a MEMS simulation software package. 3D models of the various device designs have been created including the anchors and the surrounding substrate. The mode frequencies and mode shapes have been simulated, including the response to a stiffness perturbation. The simulation results will be compared to the theory and later compared to the measured results.

Chapter 6 details the design and implementation of the testing set-up. The design of the output circuitry used to extract the amplitude ratio of the coupled resonator pair will be outlined. DC bias voltages have been used to create the coupling spring between the resonators and also to induce a stiffness change in one of the resonators. The equipment used to apply the DC voltages will be shown, as well as the application of the AC actuation signal. In addition, the devices have been tested under vacuum and the set up of the vacuum chamber will be shown. Also, the chapter details the initial characterisation of a coupled-device, confirming the mode-localisation behaviour, validating the experimental set-up.

Chapter 7 contains experimental results concerning the detection of stiffness change in electrostatically coupled MEMS resonator pairs. The testing of devices of different architectures and different fabrication processes will be presented. For each design, several devices of different dimensions have been tested, allowing for the influence of various structural parameters on the stiffness sensitivity to be characterised. Comparison will be made to previously reported mode-localised stiffness sensing in the literature, with the aim of showing an improvement.

Chapter 8 contains the experimental results and discussion concerning the detection of mass change in a pair of electrostatically coupled resonators. The design of the device has been chosen to enable its potential future use as a biological sensor. The mass of one of the resonators has been reduced using a focused ion beam and the chapter will detail the process. As with the stiffness change measurements, a comparison will be made to previously reported mode-localised mass sensing in the literature, with the aim of showing an improvement.

Chapter 2

Background to MEMS-based sensing

2.1 Introduction

This chapter presents previously published research concerning sensors based on MEMS structures. First, several examples of the measurement of the static deflection of a MEMS structure are presented, which mainly comprise pressure sensors. Then, examples from the literature of the detection of the stiffness change of a MEMS structure, utilising resonant frequency-shift, are analysed. The various sensors that utilise resonant frequency-shift stiffness sensing are explored.

An outline of the mechanical theory that describes the resonant behaviour of microscale structures is presented. The relationship between resonant frequency and the stiffness and mass of a structure is theoretically derived using a simple mass-spring model.

The detection of a mass change of a MEMS resonator has been demonstrated in the literature, and this chapter will detail previous research in the field. A particular area of mass sensing that has been explored in more detail is biological sensing, where the mass of a biological element that has been immobilised on a MEMS structure is detected.

Current biosensor technology takes the form of paper-based tests such as lateral flow assays (LFAs). Another popular method is the enzyme-linked immunosorbent assay (ELISA). The current methods are capable of the detection of various analytes, such as proteins, hormones or antigens.

There is a range of sensor applications where greater concentration sensitivity to biological elements is desirable including medical diagnostics. Biomedical scientists increasingly need to be able to measure the interaction between proteins, antibodies and antigens in test samples with concentrations as low as the fg/ml range [15]. In addition to improved

sensitivity, faster measurement times are also needed, particularly for medical diagnostic tests for use at the point of care. Having a sensor that does not require extensive laboratory apparatus would be advantageous and can be realised through the use of MEMS-resonator based sensors.

At the end of the chapter, Tab. 2.1 and Tab. 2.2 summarise all the literature presented and show the state-of-the-art stiffness and mass sensitivities that will be used in the next chapter for comparison with reported examples of mode-localised sensing in the literature.

2.2 MEMS sensors based on static deflection measurement

2.2.1 Force and pressure sensing

The static deflection of a MEMS structure can be used to determine the magnitude of the force that it is subject to. It is possible to determine the pressure experienced by a MEMS device by measuring the resulting deflection of the structure. A great deal of research has been performed into the development of MEMS-based pressure sensing over the last decade and a brief summary is presented now.

A quasi-concertina MEMS device [16] has been characterised and has been shown to possess a high linear range with deflections up to 1080 μm, caused by a force of up to 200 μN.

An example of a MEMS pressure sensor has been demonstrated [17, 18], which incorporates piezoresistive sensing of the deflection of a silicon membrane. A Wheatstone bridge has been formed consisting of two piezoresistors and two MOSFETs on the membrane, as shown in Fig. 2.1. The output voltage from the Wheatstone bridge varies in response to the deflection of the membrane, allowing the pressure to be determined. Other studies have used capacitive transduction to measure the membrane deflection [19].

Additional designs for static deflection based MEMS pressure sensors have been fabricated and characterised by others in the literature. A variation on the simple membrane design is to incorporate an additional movable structure that is suspended below the membrane [20], resulting in a greater sensitivity (61 %) of the capacitance change in response to a given pressure on the membrane. In addition, there are many examples of research concerning MEMS pressure sensors where the deflection of the structure is determined optically. One such example [21] demonstrates a device based on optical inspection of the deformation of hollow parylene tubes in response to pressure.

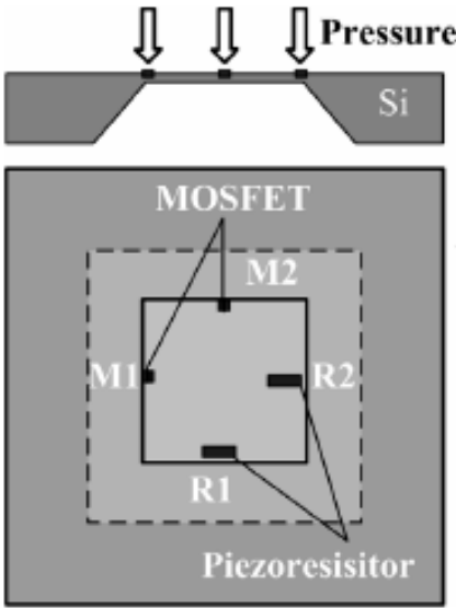

FIGURE 2.1: Schematic of a previously reported MEMS pressure sensor [17].

2.2.2 Mass sensing

The same principle demonstrated for pressure sensing has been used for mass sensing. The most widely reported research into mass sensing based on the the static deflection of a MEMS structure is biological and chemical sensing. MEMS biosensors typically consist of a microstructure that is coated, or "functionalised", with a biological material that will readily form bonds with the target analyte [22]. A summary of various examples of MEMS static-deflection biological and chemical mass sensing is now presented.

A study has reported on a diaphragm consisting of a 4 μm thick layer of nickel titanium (NiTi) that has been fabricated to allow for the deposition of a biosensitive hydrogel on its underside [23]. The hydrogel has been utilised in a previous study [24] for the detection of glucose with a magnetoelastic thin-film sensor. The diaphragm is the bottom plate of a two-plate capacitor, as can be seen in Fig. 2.2. In the presence of a solution of calcium nitrate tetrahydrate the hydrogel swells and causes a change of capacitance as the diaphragm is forced towards the other capacitor plate, allowing for a measurement of the solution concentration. The device has been tested as part of a LC circuit and showed a shift in the electrical resonant frequency of the circuit of 33 MHz for an applied pressure of 32 kPa, which would correspond to a shift of 66 Hz/μM for concentration values up to 0.5 μM.

MEMS devices have been demonstrated that detect a chemical reaction by measuring optically the deflection of a cantilever [25, 26]. The deflection is a result of a bimetallic cantilever (Si coated with Al) heating up due the chemical reaction. The system is capable of detecting a change in temperature as small as approximately 10^{-5} K. Another study measured optically the differential deflection of a cantilever array in response to

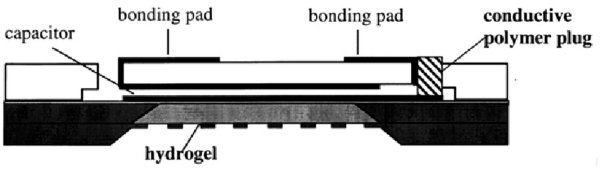

FIGURE 2.2: Cross section of microsencor for detection of calcium nitrate tetrahydrate [23]

adsorption of hydrogen onto a layer of platinum on the surface [27].

A previous study reports on a biosensor based on a micromechanical cantilever that has been functionalised with a layer of biotin [28, 29]. Biotin is a vitamin B complex and demonstrates great affinity towards a protein known as avidin. Biotin will also bind with streptavidin (SA), a related protein that is widely used in bioresearch. One side of a microscale silicon nitride cantilever has been coated with biotin and then exposed to a flow of solution containing 6 μg/ml of SA. The resulting deflection of the cantilever is measured optically with a laser using the "beam bounce" technique. The cantilever bends away from the functionalised surface as a result of compressive stress, as shown in the results presented in Fig. 2.3. In addition, the device showed sensitivity to bovine serum albinum (BSA), a protein derived from cows. BSA does not bind to biotin as readily as SA, so a higher concentration has been used (100 μl/ml).

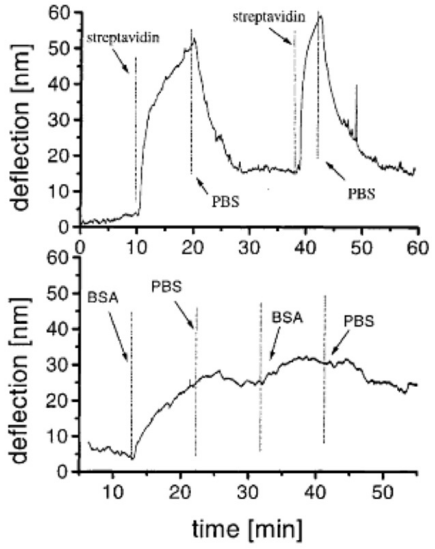

FIGURE 2.3: Deflection response of biotinylated cantilever to SA and BSA [29].

Similar studies [30, 31] have been published where an interferometric sensor has been used to determine the differential bending of a pair of microcantilevers, one of which has been functionalised with a layer of biotinylated BSA. Biotin-streptavidin binding has been measured when the structure is submerged in a solution containing SA (700 μg/ml). The measured deflections are shown in the graph of Fig. 2.4. Another study [32] features the optically sensed differential bending of a pair of cantilevers, with the cantilevers being

functionalised with a layer of DNA molecules. The cantilever bending occurs when the DNA molecules bond with its complimentary DNA sequence, after the cantilevers have been immersed in a solution containing the complementary DNA molecules. The device demonstrated the ability to distinguish between two DNA molecules that differ by only a single base sequence.

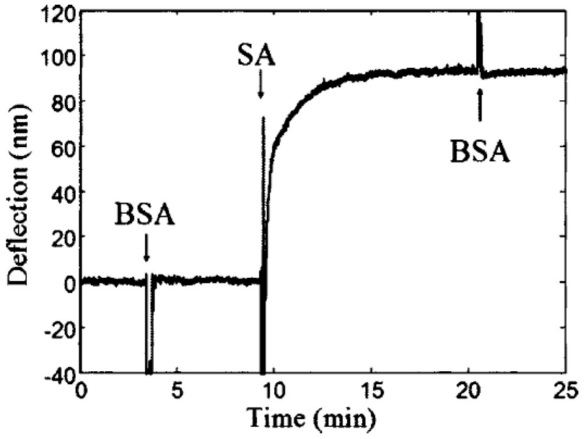

FIGURE 2.4: Differential deflection response of cantilevers to SA [30]

Another biosensor based on a commercial atomic force microscope (AFM) cantilever has been demonstrated [33], but with a different analyte. In this case, a concentration of 20 mM of glucose in a solution has been detected by coating the top of the cantilever with glucose oxidase, an enzyme. As with the other studies, compressive stress induced by the extra mass attracted to the cantilever causes the bending.

The studies that have just been analysed demonstrate the basic principle of MEMS-based biological mass sensing with functionalised microstructures. Combined with the studies on pressure sensing, it can be seen that sensing based on the static deflection of a MEMS structure has been well characterised. The remainder of this chapter will focus on the theory, and the previous research conducted into, sensors based on resonant frequency-shift.

2.3 Theoretical analysis of MEMS resonant frequency-shift sensing

The next evolution in MEMS-based sensing after static deflection measurement has been resonant frequency-shift measurement. It has been shown previously [34] that the advantages of resonant frequency-shift include its quasi-digital nature, which contrasts with the necessity to employ analogue-to-digital conversion with the output from a static-deflection based system. This section presents a study of the fundamental theory of resonant frequency-shift based sensing.

Any structure, including a MEMS resonator, can be represented by a simple lumped-element model, as shown in Fig. 2.5, consisting of a mass, m, and a spring with a stiffness, k. If the mass is subject to force, F, then a displacement, x, will result in the same direction.

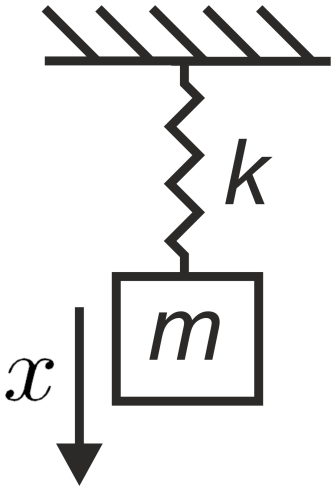

FIGURE 2.5: Lumped-element model of a simple 1-DOF resonator.

The one degree-of-freedom (1-DOF) system is analysed using Newton's second law ($F = m\ddot{x}$) to describe the behaviour of the mass and Hooke's law ($F = -kx$) to describe the behaviour of the spring. The two forces act in opposite directions (as indicated by the minus sign in Hooke's law), so the mass-spring system can be described by the following equation of motion

$$m\ddot{x} - kx = 0 \tag{2.1}$$

The acceleration can be described in terms of the angular frequency, ω_0, as follows

$$\ddot{x} = {\omega_0}^2 x \tag{2.2}$$

If (2.2) is substituted into (2.1), the following derivation of frequency can be performed

$$\begin{aligned} {\omega_0}^2 mx - kx &= 0 \\ {\omega_0}^2 m &= k \\ {\omega_0}^2 &= \frac{k}{m} \\ \omega_0 &= \sqrt{\frac{k}{m}} \end{aligned} \tag{2.3}$$

The frequency derived in (2.3) is the natural frequency of the structure represented by

the mass-spring system of Fig. 2.5. Expressed in hertz, the natural frequency of the system, f_0, is given by

$$f_0 = \frac{1}{2\pi}\sqrt{\frac{k}{m}} \tag{2.4}$$

In the absence of damping, a structure set in motion by an external force will oscillate at its natural frequency. However, in reality, all structures are subject to various types of damping, which will shift the frequency at which the oscillations are at their largest. The frequency at which the largest oscillation amplitude occurs is known as the resonant frequency, which tends towards the natural frequency if the damping reduces. Consequently, for the remainder of this thesis, f_0 will be used to represent the resonant frequency.

Sources of damping for MEMS resonators can be classified into three categories: structural, material and atmospheric [35]. Structural damping is the mechanism whereby vibration energy is lost from the resonator to the surrounding substrate through the anchors. Material damping is the vibration energy that is lost through heat generation that is a result of atomic level movement. The third source of damping, the surrounding atmosphere, is the most significant for micro-scale structures such as the resonators that are considered in this thesis. The damping is due to the flow of the surrounding gas around the resonating structure.

The quality (Q)-factor of a MEMS resonator describes the level of damping, with a higher value of Q-factor indicating lower damping. For a MEMS resonator, the Q-factor describes the relationship between the bandwidth and the resonant frequency, f_0, according to the following equation

$$Q = \frac{f_0}{\Delta f_{3dB}} \tag{2.5}$$

where Δf_{3dB} is the 3 dB bandwidth of the resonant peak and is defined as the frequency range where the vibration amplitude of the resonator has not dropped from the peak value by more than -3 dB.

In most practical applications, resonant frequency-shift based sensors are designed to minimise the damping. For example, atmospheric damping is minimised by operating the resonator in a vacuum, thus eliminating the flow of gas around the microstructure. If a structure is continuously actuated with an alternating force that is swept through a frequency range, the amplitude of the oscillations will be at a maximum at the resonant frequency. If the damping is minimised, identifying the resonant frequency becomes easier, as the maximum vibration amplitude at resonance is increased and the bandwidth of the resonant peak is narrower.

However, for certain applications, particularly biosensing, it may be desirable to operate a MEMS resonator in a liquid. For example, to determine the presence of a contaminant in a solution. Operating in a liquid will result in greater viscous damping than operating in air, lowering the Q-factor. A solution to the problem that is widely reported is to immerse the device in the solution and allow the adsorption of the analyte onto the functionalised surface to occur before removing and allowing to dry and then measuring the resonant frequency in atmosphere or vacuum. While the approach solves the problem of Q-factor, it does not allow for real-time measurement and there is a risk of stiction occurring during the drying stage.

In addition to the resonant frequency, the structure possesses additional harmonics where the oscillations will be increased, though to a lesser degree than the resonant frequency. At the resonant frequency and each of the additional harmonics, the structure will oscillate with a particular shape, known as a "mode shape". A simple method of visualising mode shapes is to consider a string fixed at both ends, as shown in Fig. 2.6. The mode shapes of the first four harmonics can be seen, with the first harmonic being the resonant frequency.

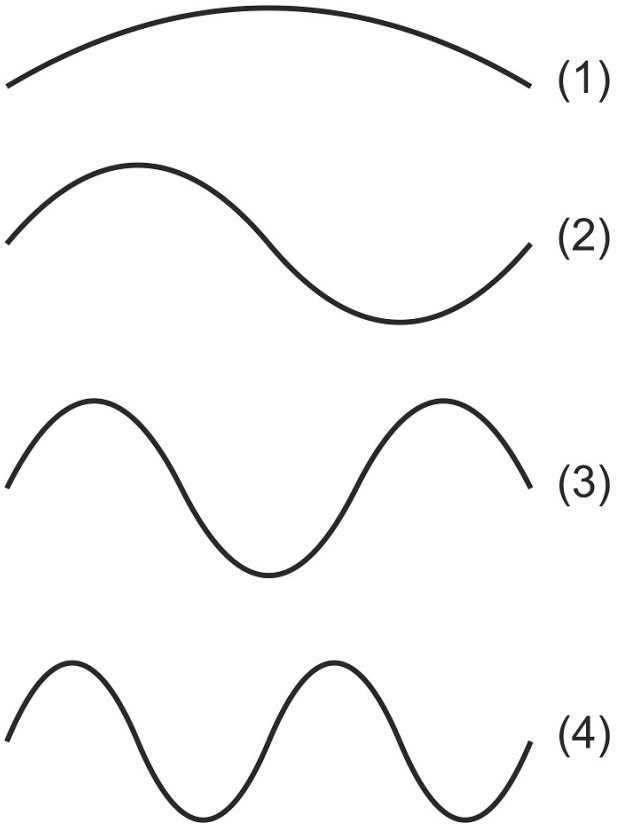

FIGURE 2.6: First four mode shapes for a string fixed at each end.

Simple MEMS structures, such as rectangular beams that are fixed at each end, possess the mode shapes seen in Fig. 2.6. An example of MEMS clamped-clamped beams from the literature is shown in Fig. 2.7. More complex structures, such as rings or discs, have more complex mode shapes, but the resonant frequency can always be calculated using

(2.4), provided that a calculation of its effective mass, m, and stiffness, k, can be made and that damping can be neglected.

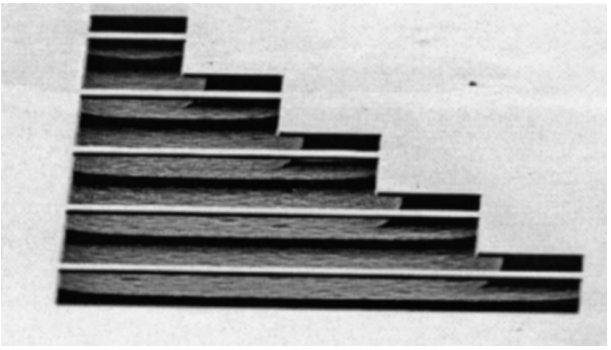

FIGURE 2.7: Example of MEMS clamped-clamped beams with lengths from 50 μm up to 250 μm [36].

From (2.4), it can be seen that altering the value of the mass or stiffness of a structure will alter its resonant frequency, allowing for the realisation of resonant frequency-shift based sensing. The sensitivity, S_k, of the resonant frequency of a structure to a stiffness change is defined as

$$S_k = \frac{\Delta f_0/f_0}{\Delta k/k} \tag{2.6}$$

where $\Delta f_0/f_0$ is the relative shift in the resonant frequency and $\Delta k/k$ is the relative shift of the stiffness in response to the quantity being measured. The sensitivity, S_m, to a mass change has a similar expression

$$S_m = \frac{\Delta f_0/f_0}{\Delta m/m} \tag{2.7}$$

where $\Delta m/m$ is the relative shift in the mass of the structure.

While the theory describes the sensitivity of the resonant frequency to a change in the stiffness or mass of the resonator, it is important to note that an important parameter of a MEMS resonant frequency-shift sensor is its resolution. The resolution is defined as the minimum change in the stiffness or mass of the resonator that is detectable by the frequency-shift. As well as the frequency bandwidth, the minimum resolvable shift is determined by the noise, which is the random fluctuation of the measured resonant frequency when the stiffness and mass of the structure is not being altered.

Both the mechanical and electrical components of a MEMS-based sensor will contribute to the noise present in the output signal [35]. Thermal noise in the mechanical part of the system is caused by the random fluctuation of electrons, atoms and molecules in the same plane as the resonator's oscillation. In addition to the thermomechanical noise, there is the noise associated with the electrical circuitry that is used to actuate and

sense the resonators, leading to errors with any frequency-counting circuits that may be employed to compare the resonant-frequency with a reference.

Previous research [37] has produced a well-established formula to define the theoretical minimum detectable change of mass of a MEMS resonator as follows

$$\delta m = 2m\sqrt{\left(\frac{\Delta f_{3dB}}{2\pi Q f_0}\right)\left(\frac{k_b T}{E_{max}}\right)} \tag{2.8}$$

where k_b is Boltzman's constant, T is the temperature and E_{max} is the maximum mechanical energy stored in the resonator. The influence of temperature on the noise can be seen as well as the influence of the Q-Factor.

2.4 Actuation and sensing methods

In order to determine the resonant frequency of a MEMS resonator, it is necessary to actuate it through a range of frequencies. Then, the resulting vibration amplitude of the structure needs to be measured.

A widely used method of actuation is electrostatic, where electrodes are positioned below (for out-of-plane oscillation) or alongside (for in-plane oscillation) the resonator [38]. A force is experienced by the resonator if two different potentials are applied to the resonator and the electrode. The force can be calculated as follows

$$F = \frac{V^2 \varepsilon A}{2g^2} \tag{2.9}$$

where V is the potential difference, ε is the permittivity, g is the gap between the electrodes and A is the area of the two faces of the beam and electrode on either side of the gap. If an AC signal is applied, the resonator will be attracted by varying degrees to the electrode as the input signal oscillates. Therefore, the resonator will oscillate at the frequency of the input signal. To detect the oscillations of a resonator, the reverse of the actuation process can be performed. The capacitance between the resonator and the electrode will vary as the resonator oscillates and can be measured in order to determine the frequency with the highest oscillation amplitude.

A large body of previously published research uses an optical method for detecting the oscillation frequency of the resonator, utilising a laser Doppler vibrometer. A laser beam is bounced off the resonator and by detecting the Doppler shift of the reflected beam, the frequency and amplitude of a structure's oscillations can be determined. The resonator is usually placed on a plate or disc that vibrates and is swept through a range of frequencies, allowing the resonant frequency to be determined.

Another set of relatively recent literature focused on the use of piezoelectrically actuated and sensed resonators as biosensors. Piezoelectric actuation of a resonator is achieved by depositing and patterning a layer of piezoelectric material on top of the resonator structure. Examples of piezoelectric material include zinc oxide (ZnO) and lead zirconate titanate (PZT). When an AC signal is applied across a piezoelectric material, the alternating electric field shifts the dipole moments of the crystal domains, resulting in alternating compressive and tensile strain in the direction of the electric field. The amplitude of vibration of the structure can be extracted by measuring the impedance of the piezoelectric layer. A frequency sweep can be performed in order to determine the resonant frequency.

In addition, piezoelectric transduction for MEMS resonating structures has been demonstrated previously for strain sensors [39], where the resonant frequency of a suspended microstructure will shift if it is subjected to strain.

2.5 Literature review of resonant frequency-shift stiffness change sensing

This section will present a review of the current state of research regarding MEMS devices that utilise a stiffness change of a microscale structure as a sensing mechanism.

2.5.1 Accelerometers

MEMS-based resonant accelerometers measure the resonant frequency shift of an oscillating structure in response to an acceleration. A micromachined proof mass is designed so that any force experienced due to acceleration is transferred to a smaller resonator, causing a shift in the resonator's resonant frequency.

Fig. 2.8 shows a previously reported [40, 41, 42] design of a MEMS accelerometer, with actuation and sensing performed using capacitive transduction. When the proof mass moves in-plane in response to an acceleration, an axial force is transferred to a resonating beam, resulting in a resonant frequency shift. The sensitivity of the device is 430 Hz/g, described in terms of the shift in resonant frequency (Hz) in response to acceleration (g). If the sensitivity of the resonator beam is calculated according to (2.6), a value of 2.05 is obtained.

A great deal of research [43, 44, 45, 46] has been performed with accelerometers, varying design architectures and readout circuitry in order to optimise device sensitivity. The out-of-plane sensitivity has been optimised with an alternative design [47], with a reported sensitivity of 584 Hz/g.

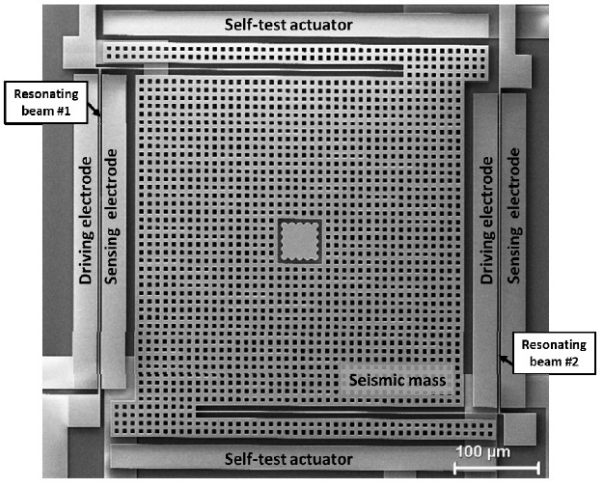

FIGURE 2.8: Example of MEMS accelerometer [40]. The large proof mass and smaller resonating beams can be seen.

The continuing research into MEMS accelerometers demonstrates the appetite for a method that will improve the sensitivity of a MEMS resonator to a change in stiffness.

2.5.2 Strain sensors

Another widely reported use of MEMS resonators is as strain sensors. If a MEMS resonator is subject to a deformation induced by strain in the object being measured, the stiffness of the resonator will change. Consequently, the response of the resonant frequency can be utilised to determine the strain. Potential applications for MEMS strain sensors include torque sensors for the automotive industry [48].

A doubled-ended tuning fork (DETF) resonator design (example shown in Fig. 2.9) has been reported as a design architecture for MEMS strain sensors [49, 50, 51], with the capability to detect a deformation of 6.6 pm in a resonator with a length of 200 μm, a strain of 33 nε. Additional research has been published by others concerning strain sensors incorporating MEMS resonators of the DETF design [52, 53], with sensitivities of up to 0.11 $\mu\varepsilon$ reported.

Additional examples in literature regarding MEMS resonant strain sensors have been found, including further examples of DETF resonators [54, 55]. As with the research that has been published for MEMS accelerometers, it has been found that, for strain sensors, increasing the sensitivity of the MEMS resonator to a change in stiffness is a major goal.

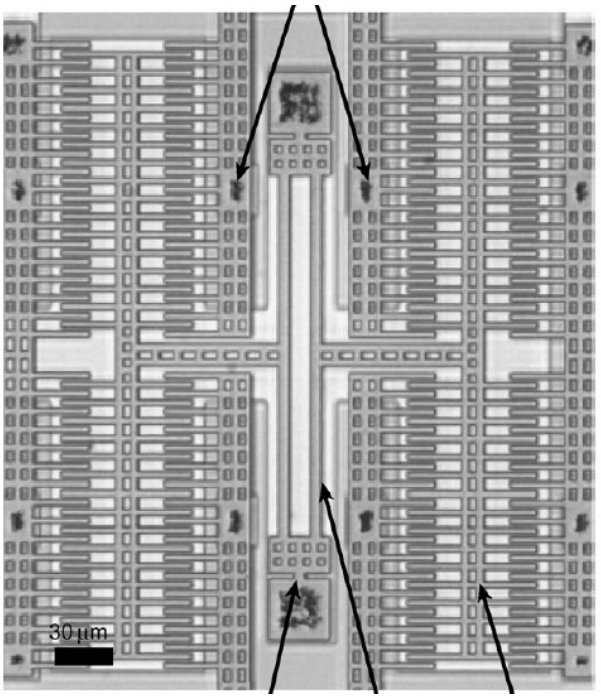

FIGURE 2.9: Example of MEMS strain sensor utilising a DETF resonator [53]. Comb drives on either side of the DETF resonator are used for capacitive actuation and sensing.

2.5.3 Pressure and force sensors

Previously reported examples of pressure sensing utilising the static deflection response of MEMS membranes have been discussed earlier in this chapter in section 2.2. Previous research has also focussed on the use of the resonant frequency response for pressure sensing using MEMS. The typical design consists of a relatively large membrane coupled to additional smaller resonators [56, 57], so that any pressure on the membrane will alter the resonant frequency of the resonators.

More recent studies [58, 59] have shown a MEMS pressure sensor with clamped-beams, in an "H" style arrangement, anchored on the frame of a rectangular diaphragm. Deflection of the diaphragm, caused by an external pressure, results in a strain being experienced by the resonators. The resulting shift in resonant frequency of the MEMS resonators is used as the output signal for the pressure sensor. The resonators have been boron-doped so that they can act as piezoresistors to provide the output signal. A sensitivity of 81.7 Hz/kPa has been reported.

In addition to pressure sensors, MEMS resonant structures can serve as force and displacement sensors. A recently reported design for a displacement sensor uses acoustic signals from a whistle-type MEMS structure [60] to detect displacements down to a few microns. The more mature technology of resonant frequency-shift based sensing shows superior performance, with recently reported research showing that MEMS structures of different designs can be used to detect forces down to the nanonewton scale [61, 62].

2.5.4 Atomic force microscopy

A major area of application for MEMS resonators is atomic force microscopy (AFM), used for characterising the surface topography of a sample. In addition, the technique has been used for measuring surface potential or the hardness or charge of biological samples.

When operating in non-contact mode, a sharp tip at the end of a MEMS cantilever is scanned across the sample surface. The cantilever is actuated such that it oscillates at its resonant frequency. As the tip approaches the sample surface, it experiences van der Waals forces, lowering the stiffness of the cantilever, which lowers the resonant frequency. A feedback loop maintains the resonant frequency of the cantilever by adjusting the tip-to-sample distance during scanning. By monitoring the change in z-axis position of the tip, a topographical picture of the sample surface is created.

The precursor to AFM was scanning tunnelling microscopy (STM), which determines surface topography by measuring the current between the tip and the surface that results from quantum tunnelling [63, 64].

Previously published research concerning AFM has focussed on improving the sensitivity, in order to improve the imaging resolution or to measure ever smaller forces, potentials or biological samples. Methods for improving the sensitivity include operating in vacuum [65], improving the Q-factor of the cantilever. Other developments in AFM technology include the detection of voltages on integrated circuits or semiconducting materials [66].

Utilising the higher resonant modes of an AFM cantilever has been demonstrated [67] and it has been found that at higher order modes, overlap between hydrodynamic and attractive interactions is avoided, resulting in a 7 times improvement in sensitivity for the second harmonic compared to the fundamental mode.

As well as AFM systems based on cantilevers, additional designs have been developed and characterised such as an axial probe [68], which can detect a force of 9 nN. An additional design architecture demonstrated is a W-shaped cantilever [69].

Research aimed at improving the sensitivity and resolution of AFM continues with more recent examples in the literature investigating new piezoelectric materials such as Langasite [70].

2.6 Literature review of resonant frequency-shift mass sensing

A review of existing research into MEMS resonant frequency-shift based mass sensors is presented in this section. As seen in (2.4). a change in the mass of a resonator will cause a shift in its resonant frequency. A widely reported utilisation of the MEMS resonant frequency-shift sensing mechanism is biological sensors, where it is necessary to detect a change in mass of a resonator, caused by the attachment of a target analyte.

2.6.1 Current state-of-the-art resonant mass sensors

Previously reported research has demonstrated the detection of the mass change of micro and nano-scale resonators down to the zeptogram (10^{-21} g) scale [71]. The adsorption of nitrogen molecules onto a silicon carbide (SiC) clamped-clamped beam has been measured successfully with an optical reflection scheme, while the temperature and pressure has been maintained at 37 K and below 10^{-10} mbar, respectively. Pulses of nitrogen gas are directed towards the device through a nozzle and the mass flow rate is monitored allowing for a direct measurement of the mass that will attach to the resonator. From an unloaded resonant frequency of 190 MHz, a decrease of 200 Hz has been measured in response to a mass increase of 100 zg. A calculation of the minimum resolvable mass change, which is determined by the frequency fluctuation noise, has been performed, with a measurement of 7 zg being possible.

Additional studies have demonstrated the resonant detection of ever smaller masses, with the smallest resolution being in the yoctogram (10^{-24} g) range [72]. The mass measurement has been demonstrated with a resonator, with $f_0 = 1.86$ GHz, consisting of a single carbon nanotube suspended over a trench that is 150 nm wide. As with the previously discussed research [71], the measurements have been performed in a cryogenically cooled (4 K) vacuum environment (0.3^{-10} mbar). The adsorption of naphthalene ($C_{10}H_8$) molecules onto the nanotube resonator has been detected, by measuring the resulting shift of the resonant frequency, with a resolution of 1.7 yg.

The subsequent sections of this chapter will focus on research to develop biological sensors based on MEMS resonant frequency-shift mass sensing.

2.6.2 Mechanically actuated and optically sensed MEMS resonant mass sensors

The successful detection of a single virus particle of vaccinia, which forms the basis of the vaccine for smallpox, has been reported [73]. A silicon cantilever has been fabricated [74] to be approximately 5 μm long, 2 μm wide and 30 nm thick. The cantilever has been

submerged in a solution containing particles of vaccinia virus and left for 30 minutes. The device is then removed from the solution and dried. The resonant frequency of the cantilever is measured optically before and after its exposure to the virus solution. In addition, the number of virus particles that had attached to the cantilever has been counted using a scanning electron micrograph (SEM), as seen in Fig. 2.10. The same measurements have been carried out for several cantilevers enabling the graph of Fig. 2.11 to be plotted. The detection of a single virus particle with a mass of 9.5 fg has been achieved by measuring a resonance decrease of 60 kHz. It should be noted that the structure is not functionalised and the test solution is simply vaccinia virus in deionised water.

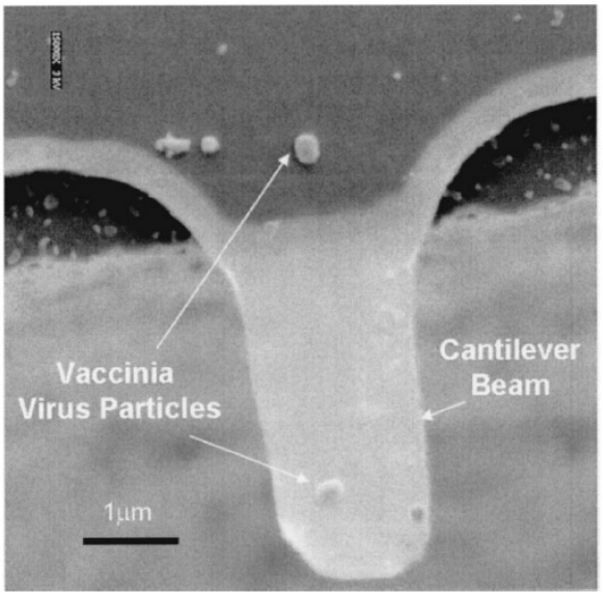

FIGURE 2.10: Scanning electron micrograph (SEM) image of silicon cantilever with attached virus particles [73]

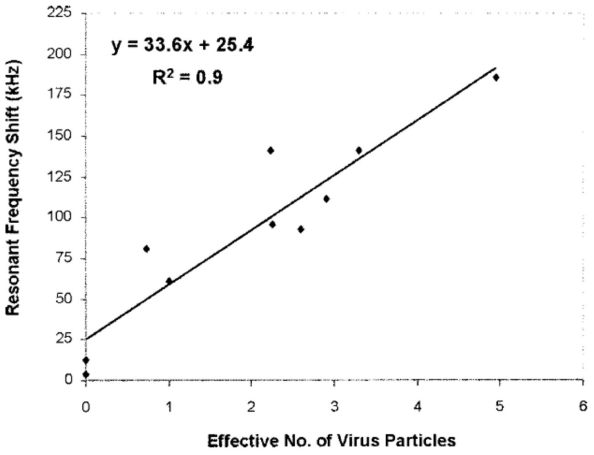

FIGURE 2.11: Resonant frequency shift vs number of vaccinia virus particles on microcantilever with intial $f_0 = 1.27$ MHz [73]

The same authors then reported results of a device that measured the presence of the

bacterium *Listeria innocua* in a solution [75]. In order to attract *Listeria innocua* bacteria, the silicon microcantilever has been functionalised with the antibody. Bovine serum albinum (BSA) has been used as a blocking agent, which prevents the bacteria binding to the structure where there is no antibody coating. The antibody and the BSA have been deposited on to the cantilever surface using micropipettes, which dispense 10-15 μl of solution. After the device has been cleaned and dried, it is immersed in a solution containing *Listeria innocua* at an approximate concentration of 5×10^8 cells/ml for 15 minutes. The resonant frequency has been measured before and after the exposure to the virus. The resonance decreased by around 500 Hz from a starting f_0 of 78.4 kHz (see Fig. 2.12), representing a mass change of 5.3 pg.

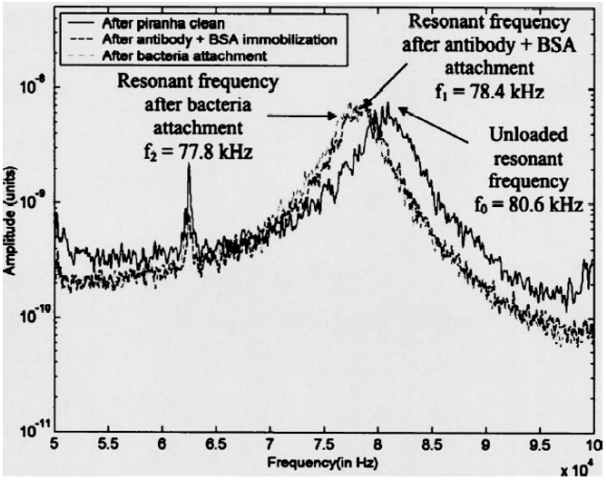

FIGURE 2.12: Resonant frequency measurement of cantilever showing attachment of *Listeria innocua* bacteria [75]

Another study designed a MEMS resonant frequency-shift biosensor that detected the growth of *Escherichia coli* on a microcantilever [76, 77]. The structure has been functionalised with agarose, a primary hydroxyl group. The cantilever has been inserted into a microcapillary (see the example in Fig. 2.13) containing the agarose solution for 10 seconds and then removed and allowed to dry. Then, the cantilevers are coated with an *E. coli* suspension using the microcapillaries and immediately placed in a box where the temperature and relative humidity are maintained at 37 °C and 93 %, respectively.

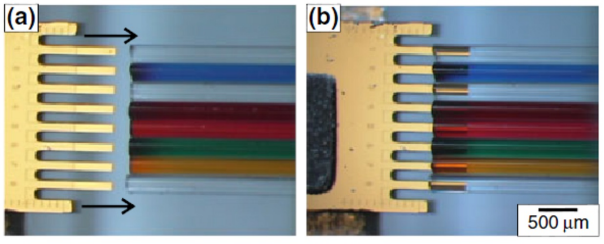

FIGURE 2.13: Example of functionalising microcantilevers with microcapillaries [78]

The resonant frequency of the cantilever has been measured periodically (along with a non-functionalised reference cantilever) over a period of 8 hours. As can be seen in

Fig. 2.14, the resonant frequency decreases as the *E. coli* grows on the cantilever surface. Multiple runs of the experiment found the average frequency shift over 8 hours to be 700 Hz. The frequency-shift represents a sensitivity of 50 pg/Hz.

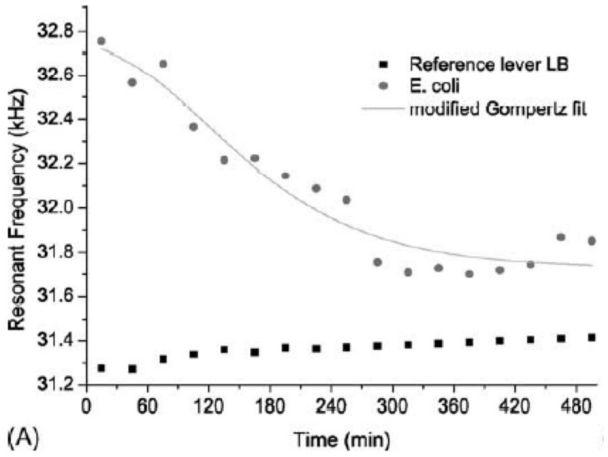

FIGURE 2.14: Resonant frequency shift caused by growth of *E. coli* on microcantilever [76]

In other studies, polycrystalline silicon cantilevers of the design shown in Fig. 2.15 have been fabricated [7, 79]. The devices have been designed to detect the baculovirus *Autographa californica* [7] or *E. coli* [79]. The structures have been functionalised by immersing the device in a solution containing either AcV1 antibodies that will readily bind with the baculovirus or antibodies to *E. coli*. The device is removed from the solution and dried. Then, the devices are immersed in a solution containing the baculovirus or *E. coli* for 1 hour before being removed and dried. At each stage in the process, the resonant frequency of the cantilever is measured using a laser Doppler vibrometer. The results for the baculovirus detection are shown in Fig. 2.16. It can be seen that the resonant frequency decreases by 50 kHz, which corresponds to an increase in mass of 2.29 fg. For *E. coli*, the smallest detectable amount has been found to be 6 pg.

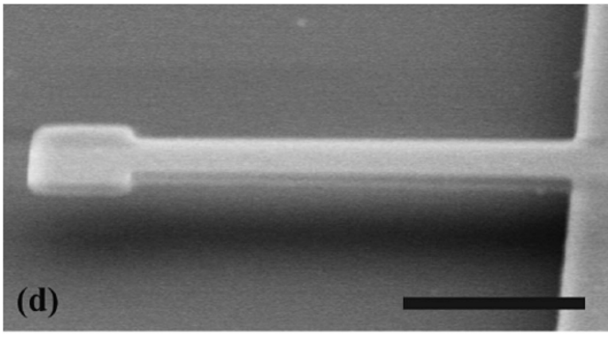

FIGURE 2.15: Cantilever fabricated with length of 6 μm, width of 0.5 μm and thickness of 0.15 μm [7].

An interesting structural design for a biosensor has been reported previously [80], where a microcantilever has been fabricated to contain a microchannel. A representation of the structure is shown in Fig. 2.17.

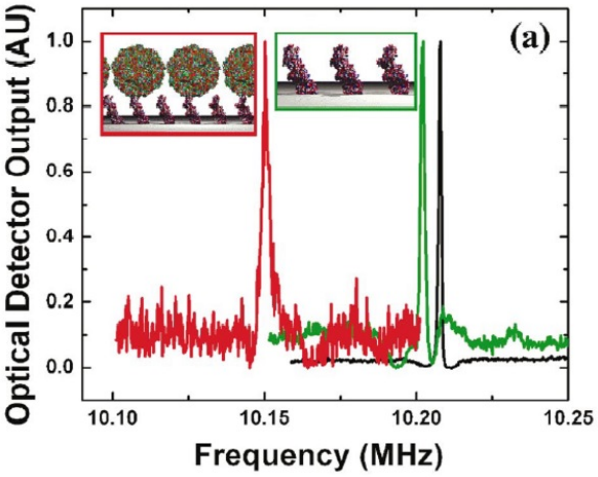

FIGURE 2.16: Resonant peak of cantilever before functionalisation (black) after deposition of antibody layer (green) after exposure to baculovirus (red). The insets depict the functionalisation and the antibody-virus binding [7]

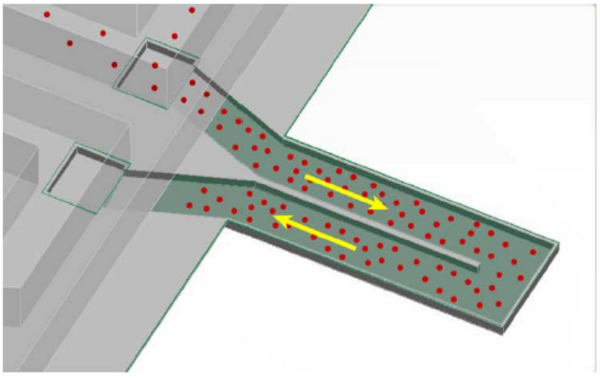

FIGURE 2.17: Suspended microchannel cantilever structure [80] The fabricated cantilever had a length of 300 μm and the microchannel is completely enclosed with inlets for injected fluid situated away from the anchor.

The interior surface of the microchannel has been functionalised with avidin by injecting a solution containing avidin into the channel. The channel has been rinsed out before a solution of biotinylated-BSA has been injected. Avidin-biotin bonding then took place and after the channel has been rinsed out, a 60 ppm change (about a 2 Hz decrease from a resonant frequency of 32 kHz) in the resonant frequency has been measured optically, attributable to BSA remaining in the microchannel, as illustrated in Fig. 2.18.

In another study utilising microcantilevers, the detection of spores of *Bacillus anthracis* has been reported [81]. In the study, the cantilevers have been fabricated from silicon and functionalised with a layer of *Bacillus anthracis* antibody. As has been used before [73], BSA has been deposited on the cantilever as a blocking agent to prevent bacteria binding on the surface where there is no antibody. After functionalisation, the cantilever has been submerged in 20 μl of *Bacillus anthracis* solution for 20 hours. Then, the device has been removed from the solution and dried. The resonant frequency has been measured before and after the exposure to the *Bacillus anthracis* solution and the shift noted. The

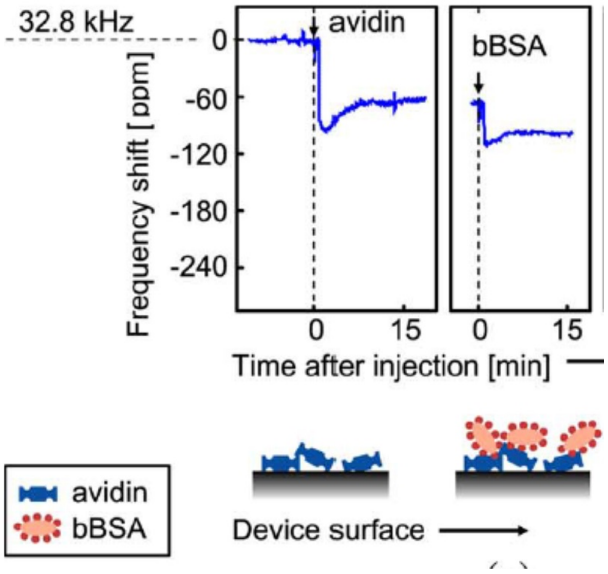

FIGURE 2.18: Frequency shift optical measurements [80]

results are shown in the graph of Fig. 2.19. The minimum mass detected in this study was 740 fg.

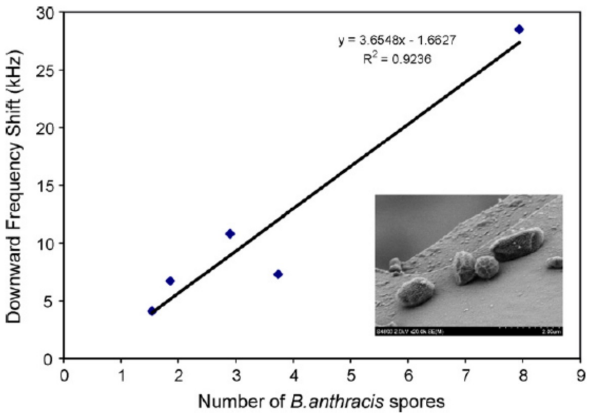

FIGURE 2.19: Frequency shift optical measurements [81]. Inset: SEM image of *Bacillus anthracis* spores on cantilever surface.

All the studies that have been reported with optical sensing utilised a laser Doppler vibrometer. The necessity to use a large piece of equipment means that, while impressive sensitivity has been reported in some cases, a great deal more development is needed to create practical sensing platforms.

2.6.3 Piezoelectrically actuated and sensed MEMS resonant mass sensors

A previous study [82] has detailed the fabrication of a Si cantilever on top of which a layer of PZT sandwiched between two layers of platinum (Pt), which acted as electrodes, has

been positioned (see Fig. 2.20). Multiple cantilevers have been functionalised to detect human insulin and different sequences of deoxyribonucleic acid (DNA). An anti-insulin binding protein has been immobilised on the tip of a cantilever and when the tip is dipped in a solution of insulin, protein-insulin binding occurs. The real and imaginary impedance of the PZT layer are extracted to find the resonant frequency and a shift of 217 Hz has been attributed to the protein-insulin binding. The calculated mass of the attached insulin is 0.46 fg.

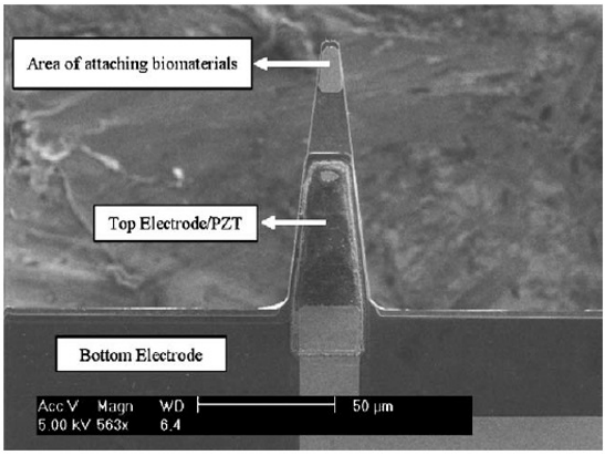

FIGURE 2.20: SEM image of piezoelectrically actuated/sensed cantilever biosensor [82]

A study [83] has reported on the fabrication of a piezoelectric device with the ability to detect the antigen to the antibody immunoglobulin G (IgG) and the antibody to the hepatitis B surface antigen (HBsAg). IgG is part of the immune system and for this study, goat IgG has been used. HBsAg is found on the surface of the hepatitis B virus envelope and detecting it can indicate whether a sample (e.g. blood) contains the hepatitis B virus (HBV).

The device that has been fabricated is a membrane structure comprised of three layers of Pt/PZT/Pt. The underside of the membrane, below the Pt/PZT/Pt layers, consists of a layer of oxide and a layer of gold. The thickness of the membrane is about 3.5 μm and the its area is 0.25 mm^2. The surface of the membrane underside is functionalised with either anti-IgG (from a goat) or anti-HBsAg, as shown in Fig. 2.21. Then, a blocking agent has been coated on the surface to prevent adsorption of the target element on non-functionalised areas of the membrane.

The device has been immersed in a solution containing either goat anti-IgG or anti-HBsAg. Then, antigen-antibody binding has taken place (Fig. 2.21d). The resonant frequency is piezoelectrically measured before the immersion in the solution and again after the device has been removed and dried. The shift in resonant frequency is illustrated in Fig. 2.22. It can be seen that the frequency decreases after the membrane is functionalised and again after exposure to either (a) goat anti-IgG or (b) anti-HBsAg.

The behaviour of the devices have been further characterised by using different solution

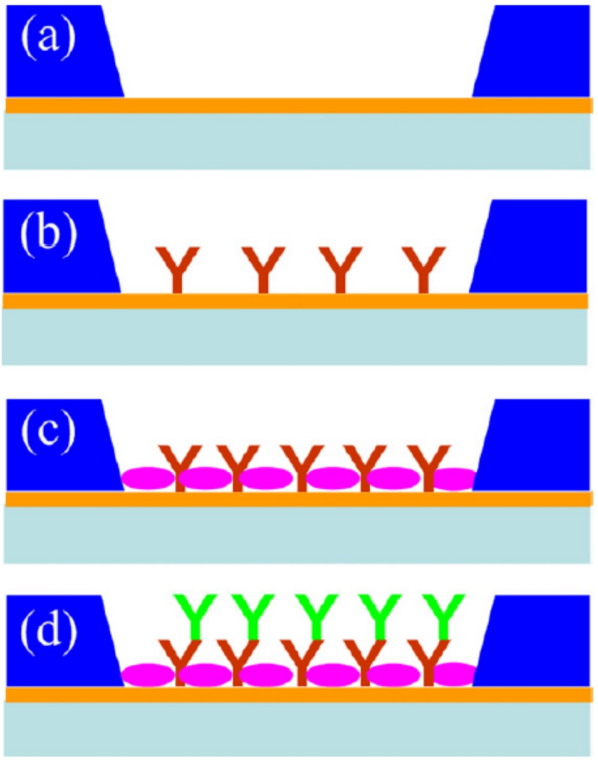

FIGURE 2.21: Schematic of piezoelectric membrane biosensor [83]: (a) membrane with gold underside (b) functionalised with goat IgG (c) uncovered gold has been blocked with a blocking agent (d) anti-IgG bonds with the IgG

concentrations when functionalising the membrane. Fig. 2.23a shows the decrease in resonant frequency measured after the membrane has been functionalised with goat IgG with concentrations ranging from 25 - 200 μg/ml. The graph suggests that using a higher concentration results in a greater quantity of IgG being immobilised on the surface. It has been found that if the membrane is functionalised with a higher concentration of goat IgG, a larger frequency change is measured after exposure to the anti-IgG solution (Fig. 2.23), probably as a result of greater antibody-antigen binding occurring. The masses of anti-IgG that have been adsorbed have been calculated to range from 16.1 ng up to 108 ng. From Fig. 2.23, the sensitivity of the device has been calculated to be 6.25 Hz/ng.

A piezoelectric biosensor based on lead magnesium niobate-lead titanate (PMN-PT), a piezoelectric material, has been demonstrated [84]. The sensor consists of a 400 μm thick patterned layer of PMN-PT with a 200 nm thick layer of gold deposited on either side, patterned into circular shapes with a diameter of 5 mm to act as electrodes and the functionalisation surface. As with a previous study [83], the sensor has been designed to detect goat anti-IgG by immobilising a layer of goat IgG on the gold surface. In addition, a protein has been used to aid the immobilisation of the anti-IgG.

Experiments have been conducted to determine the influence of varying concentrations of anti-IgG in a test solution that is dropped on to the sensor surface. The resonant

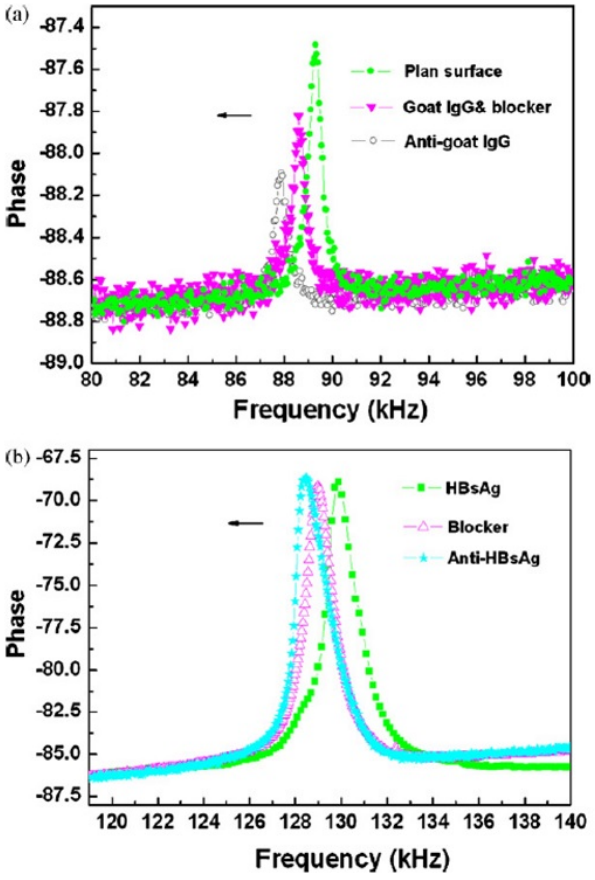

FIGURE 2.22: Shift in resonant frequency during biosensing of piezoelectric membrane [83]

frequency of the PMN-PT slab is determined before the test solution is dropped on the sensor surface and measured again after the sensor is dried. It has been found that the amount of anti-IgG that remains bonded to the sensor surface increases linearly as a function of the solution concentration, as shown in Fig. 2.24. The sensitivity of the device has been calculated to be 6.72 ng/Hz.

2.6.4 Mass sensor based on bulk acoustic resonance

A variation on the piezoelectric sensing method that has been outlined in the previous section is utilising flexural plate wave (FPW) resonators. The structure of the device fabricated is shown in Fig. 2.25 [85]. A 2 μm thick silicon membrane has a layer of piezoelectric aluminium nitride (AlN) of thickness 0.5 μm deposited on top. Then two sets of interdigitated metal electrodes are patterned on top of the AlN layer. One set is the drive electrodes and the other set is the sense electrodes.

An AC signal is applied to the drive electrodes and the piezoelectric effect causes a energy wave to travel to the sense electrodes. Then, the sense electrodes can be used to measure the vibrations of AlN at their end of the structure. The system will possess

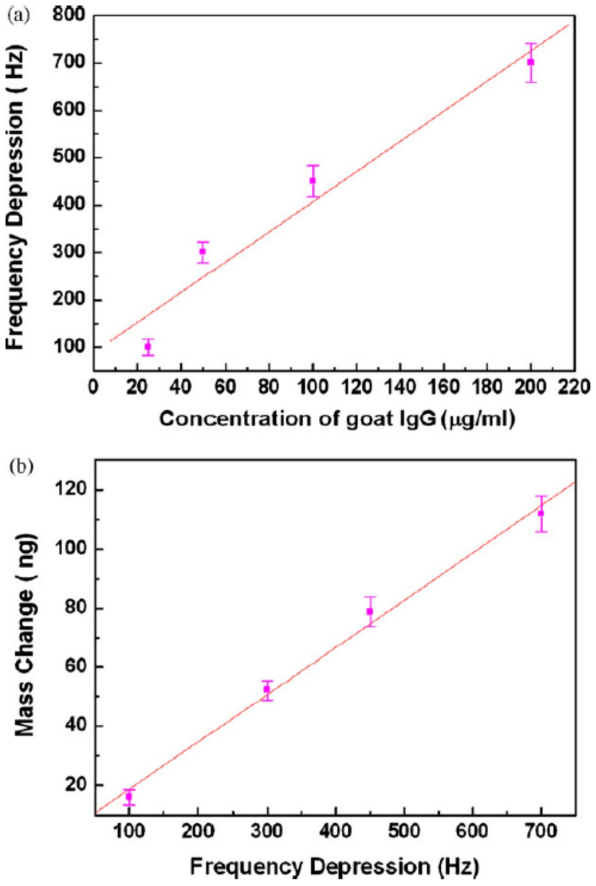

FIGURE 2.23: (a) Effect of goat-IgG concentration on the resonant frequency decrease during functionalisation (b) Calculated relationship between the change in frequency and the change in mass during biosensing [83]

a resonant frequency that is dependent on the membrane dimensions and the width, length and spacing of the electrodes. An SEM image is shown in Fig. 2.26.

The back side of the sensor (i.e. the opposite side to the electrodes) has been functionalised in order to detect various elements including the antibody IgG, interlukin 6 and the bacteria *Borrelia burgdorferi*, the agent of Lyme disease.

Interlukin-6 (IL-6) is a cytokine that is expressed by white blood cells and an increased concentration in blood has been associated with the likelihood of multiple organ failure in trauma patients. In order to detect IL-6, the membrane back side has been coated with an antibody that will readily bind with IL-6. Experiments have demonstrated a decrease in resonant frequency of the device when it is exposed to an IL-6 solution, with larger frequency decrease measured for a higher concentration of IL-6 solution. The ability to detect the concentration of an IL-6 solution down to the order of ng/ml has been achieved.

The surface of *B. burgdorferi* expresses a particular protein (OspA) that will readily bind with the antibody anti-OspA. An experiment exposed a membrane with a layer of

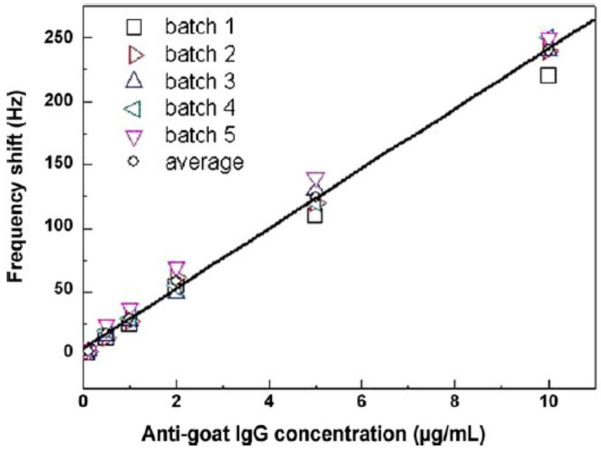

FIGURE 2.24: Resonant frequency shift as a function of the concentration of the goat anti-IgG solution [84]

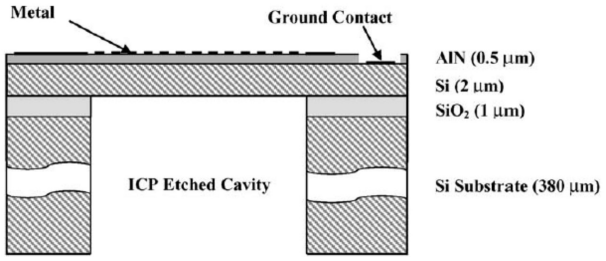

FIGURE 2.25: Cross section diagram of flexural plate wave structure [85]

OspA to a 200 ng/ml solution of anti-OpsA and a 50 kHz decrease is frequency has been measured. The same device design has been used to detect full intact *B. burgdorferi* by using an anti-OpsA functionalised membrane surface.

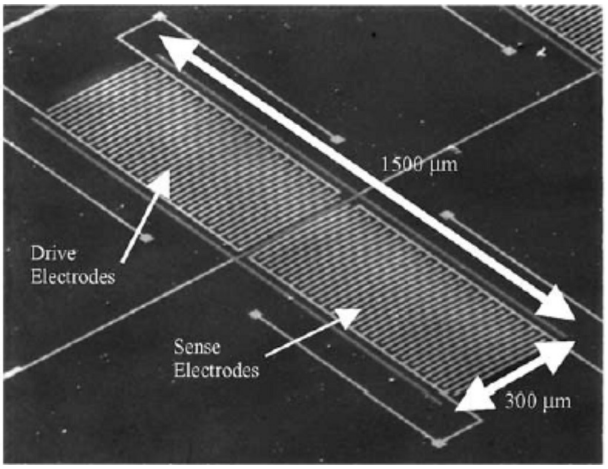

FIGURE 2.26: SEM image of flexural plate wave structure [85]

2.6.5 Mass sensors based on atomic force microscopy

There are several examples in the literature of biosensing based on atomic force microscopy (AFM), with the probe being used to measure interactions between biomolecules [86]. The AFM tip can be used to measure the force of a biotin-streptavidin interaction [87, 88] or an antibody-antigen interaction [89, 90, 91]. The AFM tips are functionalised (with biotin, for example) and force-distance measurements are performed on a surface that has been incubated in a solution containing the target analyte (avidin, for example). Where interactions take place, the force experienced by the AFM cantilever is measured and biosensing is realised.

The necessity of utilising an AFM system to perform these measurements limits their practical possibility. However, the measurement principle of functionalising the surface of a resonant structure is applicable to systems where it is desired that the analyte bonds to the resonant structure surface.

2.7 Summary

In this chapter, the existing published research concerning MEMS-based sensing has been outlined. In addition, the background theory concerning resonant frequency-shift based sensing has been detailed, along with a further literature review detailing existing research into stiffness change and mass sensing. In particular, it has been found that a large body of current MEMS-based mass sensing is concerned with the detection of biological elements that attach to functionalised surfaces.

Tab. 2.1 lists sensors that are based on the stiffness change of a MEMS structure in order to detect either displacement, acceleration or strain. The devices listed in the table represent the highest sensitivities reported. The published literature does not always allow for a determination of the sensitivity, as defined by (2.6), to be made, but where possible the value has been listed in Tab. 2.1. It can be seen that sensitivity values between 1.5 and 2.05 have been demonstrated. In the next chapter of this thesis, comparison will be made between the device performances shown in Tab. 2.1 and the sensitivity of more recently developed MEMS sensors that are based on mode-localisation.

Device Design	Measurement Method	Limit of Detection	Sensitivity, S_k	Reference
Displacement sensor	Static deflection	200 μN	N/A	[16]
Accelerometer	f_0-shift	0.5 μN	2.05	[40]
Accelerometer	f_0-shift	0.2 g	1.53	[47]
Strain sensor	f_0-shift	33 nε	2	[51]

TABLE 2.1: Comparison of the limit of detection for previously reported stiffness change sensors.

Similarly, the review of the previous literature concerning mass sensing has been summarised in Tab. 2.2. A number of the published works detail the sensitivity of a sensor to the concentration of a solution and does not detail the mass that has been immobilised on the structure, preventing a determination of the mass sensitivity. Where possible, the sensitivity for the frequency-shift based devices has been calculated according to (2.7) and is listed. The highest sensitivity that has been reported is 5235 [82], which is from a piezoelectrically actuated and sensed cantilever. In addition, the minimum demonstrated mass or concentration detected by each device is given. In addition, if available, the theoretical smallest mass change that could be detected by the device is listed.

Analyte	Measurement Method	Demonstrated Detection	Limit of Detection	S_m	Ref.
Streptavidin	Static deflection	0.1 μM	N/A	N/A	[29]
BSA	Static deflection	1.6 μM	N/A	N/A	[29]
Streptavidin	Static deflection	12 μM	N/A	N/A	[30]
Glucose	Static deflection	20 mM	N/A	N/A	[33]
Calcium nitrate tetrahydrate	Static deflection	0.5 μM	N/A	N/A	[23]
Vaccinia	f_0-shift, optical	9.5 fg	160 ag	4	[73]
Listeria Innoccua	f_0-shift, optical	5.3 pg	2.12 pg	0.038	[75]
E. coli	f_0-shift, optical	50 pg	50 pg	0.04	[76]
Autographa californica	f_0-shift, optical	2.29 fg	50 ag	0.03	[7]
Anthrax	f_0-shift, optical	740 fg	423 fg	23	[81]
Insulin	f_0-shift	0.46 fg	N/A	5235	[82]
anti-IgG, Hepatitus B	f_0-shift	16 ng	N/A	0.536	[83]
anti-IgG	f_0-shift	670 μg	N/A	0.995	[84]
OspA protein	Bulk Acoustic Resonance	200 ng/ml	N/A	N/A	[85]

TABLE 2.2: Comparison of the demonstrated mass change detection and theoretical limit of detection for previously reported mass sensors.

From the literature review that has been performed, it has been concluded that different designs of mass or stiffness sensors yield different sensitivities. A large body of previous mass sensing relies on measuring the resonant frequency using a laser Doppler vibrometer, which suggests that there is scope for developing a sensor with both improved sensitivity and an integrated output readout implementation. The next chapter outlines the theory and previous research concerning mode-localisation based sensing, which provides a solution to improving the sensitivity of MEMS-based sensing.

Chapter 3

Background to mode-localisation

3.1 Introduction

Mode-localisation is a phenomenon that occurs in arrays of resonant structures that are coupled together. In this chapter, the background theory necessary to understand the phenomenon of mode-localisation will be outlined. Mathematical functions that can used to describe the mode frequencies and mode shapes of a coupled system will be derived and then used to model the response of coupled-resonator systems to stiffness or mass perturbations. In addition, a review of the existing literature dealing with mode-localisation based sensing will be presented.

3.2 Simple pendulum model

The simplest system that can be used to explain the mode-localisation effect is a pendulum. The pendulum model has been used to effectively explain the phenomenon [92]. Consider a pendulum consisting of a stretched string with a mass attached to the end (Fig. 3.1(a)). If the pendulum is set in motion, the period of the swing is determined by the length of the string.

Fig. 3.1(b) shows a periodic system consisting of two pendulums weakly coupled together with a spring. If the two pendulums have an equal length of string, then they will both have an equal period of oscillation. After the system has been set in motion the oscillation of each pendulum will synchronise with the other through the coupling spring.

However, if the string length of one of the pendulums is altered, the oscillation period of the two pendulums, if they were uncoupled, would be different. In a coupled system, if the periods of oscillation for the two pendulums are sufficiently different, the oscillation energy will become confined or "localised" to one of the pendulums. The energy

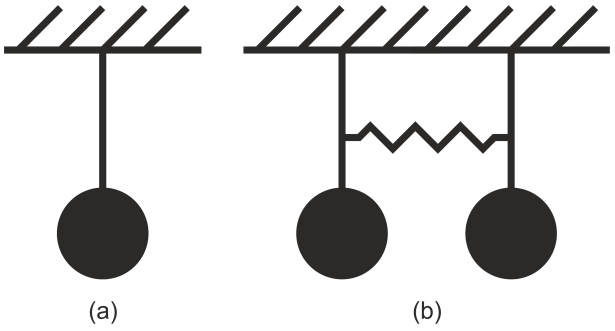

FIGURE 3.1: (a) A simple pendulum. (b) Two pendulums coupled together with a spring.

localisation results in the oscillation amplitude (or "mode shape") of each pendulum differing from the other, due to oscillation energy being coupled through the spring. The end result of introducing disorder to the system (i.e. changing the length of one of the pendulums) is that the ratio of the amplitudes (the mode shape of the coupled system) shifts away from 1:1 to become uneven.

3.3 Analysis of two degree-of-freedom model

Before this chapter introduces MEMS-based microresonator systems, a lumped-element representation of a two degree-of-freedom (2-DOF) system of two coupled resonators needs to be analysed. The model is shown in Fig. 3.2. Each resonator is represented by a mass, m_1 or m_2, and a stiffness, k_1 or k_2. The two resonators are coupled together with a coupling element represented by a spring k_c. The displacement of each resonator is given by x_1 and x_2.

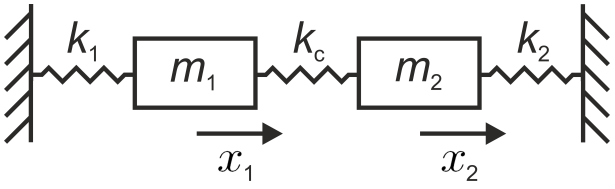

FIGURE 3.2: Lumped element model of a 2-DOF system consisting of two coupled resonators.

To describe the vibration response of the system the following equations of motion are used

$$\begin{aligned} m\ddot{x_1} + kx_1 + k_c(x_1 - x_2) &= 0 \\ m\ddot{x_2} + kx_2 + k_c(x_2 - x_1) &= 0 \end{aligned} \tag{3.1}$$

where $m_1 = m_2 = m$ and $k_1 = k_2 = k$ for a balanced system. The equations of motion can also be expressed in matrix form

$$\begin{bmatrix} m & 0 \\ 0 & m \end{bmatrix} \begin{bmatrix} \ddot{x}_1 \\ \ddot{x}_2 \end{bmatrix} = \begin{bmatrix} -k-k_c & k_c \\ k_c & -k-k_c \end{bmatrix} \begin{bmatrix} x_1 \\ x_2 \end{bmatrix} \tag{3.2}$$

Equation (3.2) can be expressed and rearranged as follows

$$\begin{aligned} M\ddot{u}_i &= -Ku_i \\ M\ddot{u}_i + Ku_i &= 0 \end{aligned} \tag{3.3}$$

where M and K represent the mass and stiffness matrices respectively and are given by

$$\begin{aligned} M &= \begin{bmatrix} m & 0 \\ 0 & m \end{bmatrix} \\ K &= \begin{bmatrix} k+k_c & -k_c \\ -k_c & k+k_c \end{bmatrix} \end{aligned} \tag{3.4}$$

To obtain the mode frequencies and the mode shapes (the ratio of x_1 and x_2 at the mode frequencies) for a 2-DOF system, the equations of motion need to be expressed as an eigenvalue problem of the form

$$Au_i = \lambda_i I u_i \tag{3.5}$$

where λ_i and u_i ($i = 1,\ 2$) represent the eigenvalues and eigenvectors, respectively. Therefore, (3.3) has been rearranged and transformed into the frequency domain as follows

$$\begin{aligned} M\ddot{u}_i + Ku_i &= 0 \\ -\omega^2 M u_i + Ku_i &= 0 \\ -\omega^2 I u_i + M^{-1}Ku_i &= 0 \\ M^{-1}Ku_i &= \omega^2 I u_i \end{aligned} \tag{3.6}$$

It can be seen from (3.6) that we need to solve the eigenvalue problem with $A = M^{-1}K$ and $\lambda_\mathrm{i} = \omega^2$. A has been calculated as follows

$$\begin{aligned} A &= M^{-1}K \\ &= \begin{bmatrix} \frac{1}{m} & 0 \\ 0 & \frac{1}{m} \end{bmatrix} \begin{bmatrix} k+k_c & -k_c \\ -k_c & k+k_c \end{bmatrix} \\ &= \begin{bmatrix} \frac{k+k_c}{m} & -\frac{k_c}{m} \\ -\frac{k_c}{m} & \frac{k+k_c}{m} \end{bmatrix} \end{aligned} \tag{3.7}$$

If the eigenvalue problem in (3.6) is solved for $A = M^{-1}K$, the following eigenvalues and eigenvectors are calculated

$$\begin{aligned} \lambda_1 &= \frac{k}{m}, u_1 = \begin{bmatrix} 1 \\ 1 \end{bmatrix} \\ \lambda_2 &= \frac{k+2k_c}{m}, u_2 = \begin{bmatrix} 1 \\ -1 \end{bmatrix} \end{aligned} \tag{3.8}$$

The eigenvalues give the mode frequencies ($\lambda_\mathrm{i} = {\omega_\mathrm{i}}^2$) and the corresponding eigenvectors give the mode shapes. A representation of the two fundamental mode shapes is shown in Fig. 3.3, with the in-phase and out-of-phase modes shown.

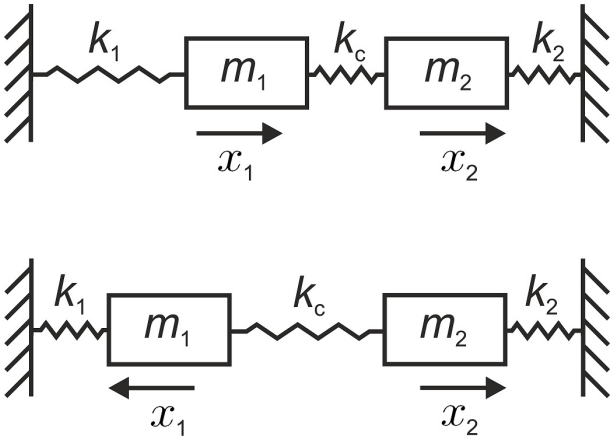

FIGURE 3.3: In-phase and out-of-phase mode shapes for 2-DOF system.

3.3.1 Analysis for electrostatic coupling

For the MEMS devices that have been fabricated and characterised in this thesis, the closely-spaced resonators have been coupled together electrostatically. A coupling spring is created by applying DC voltages to each resonator, so as to create an electric field between them. As has been reported previously [93], for electrostatic coupling, the system has a negative spring constant, given by

$$k_c = \frac{-(\Delta V)^2 \varepsilon_0 A}{g^3} \tag{3.9}$$

where ΔV is the potential difference between the resonators, ε_0 is the permittivity of free space, g is the spacing between the two resonators and A is the cross section area of the resonators at the coupling gap. The minus sign of the coupling spring results in an inversion of the mode-frequencies, with the eigenvalues and eigenvectors becoming

$$\lambda_1 = \frac{k - 2k_c}{m}, u_1 = \begin{bmatrix} 1 \\ -1 \end{bmatrix}$$
$$\lambda_2 = \frac{k}{m}, u_2 = \begin{bmatrix} 1 \\ 1 \end{bmatrix} \tag{3.10}$$

Compared to a fixed mechanical coupling, an electrostatic coupling spring possesses the advantage of being adjustable through variation of ΔV as governed by (3.9). It can seen from (3.9) that there is a non-linear relationship between the coupling gap, g, and the coupling spring constant, k_c. As a result, as the structures are resonating at one of the mode frequencies, the value of k_c will be changing. If the vibration amplitude is large enough relative to the gap between the resonators, then the spring will be non-linear. Therefore, to minimise non-linear behaviour for the coupling spring, a larger air gap should be designed.

In addition, the effective stiffness of a resonator, k_1 or k_2, can be softened by applying a DC bias to an adjacent fixed electrode. The electrostatic softening can be calculated according to (3.9). Altering the effective stiffness of one of the resonators using electrostatic spring softening can be used to introduce an imbalance into the 2-DOF system.

3.3.2 Effect of damping

A coupled resonator system will be subject to damping in the same way as a single resonator, with atmospheric damping dominating. The bandwidth, Δf_{3dB}, of both the out-of-phase and in-phase resonant peaks will increase if the damping increases, which will lower the Q-factor. Therefore, when adjusting the electrostatic coupling spring, k_c, it is important to ensure that the two peaks are kept apart sufficiently so that they are distinguishable from each other, thus allowing the amplitude of each to be determined accurately. From (3.10), it can seen that k_c determines the frequency spacing of the two modes. If the mode frequencies are too close together, then the resonant peaks will start to overlap, an effect known as mode-aliasing. If the following condition is satisfied then mode-aliasing is avoided [94]

$$\Delta f > 2 \times \Delta f_{3dB} \tag{3.11}$$

where Δf is the difference between the out-of-phase and in-phase mode frequencies. Provided that the anti aliasing condition is met, mode-localised sensing will be possible. For resonant frequency-shift sensing, any drop in Q-factor due to damping will impact on the minimum resolvable frequency-shift that can be measured, which is in contrast to

utilising amplitude ratios in a coupled system, which only needs the condition of (3.11) to be satisfied for successful measurement.

3.4 Response of a 2-DOF system to a stiffness perturbation

3.4.1 Mode frequencies of a perturbed system

For the 2-DOF system of Fig. 3.2, if a stiffness perturbation, Δk, due to the physical quantity to be measured, is added to resonator 1, and the coupling spring is electrostatic and, therefore, negative, then (3.7) becomes

$$\begin{aligned} A &= M^{-1}K \\ &= \begin{bmatrix} \frac{1}{m} & 0 \\ 0 & \frac{1}{m} \end{bmatrix} \begin{bmatrix} k - k_c + \Delta k & k_c \\ k_c & k - k_c \end{bmatrix} \\ &= \begin{bmatrix} \frac{k-k_c+\Delta k}{m} & \frac{k_c}{m} \\ \frac{k_c}{m} & \frac{k-k_c}{m} \end{bmatrix} \end{aligned} \tag{3.12}$$

The out-of-phase (λ_{op}) and in-phase (λ_{ip}) eigenvalues can be calculated as

$$\lambda_{op} = \frac{1}{m}\left(k - k_c + \frac{1}{2}\left[\Delta k - \sqrt{4{k_c}^2 + \Delta k^2}\right]\right) \tag{3.13}$$

$$\lambda_{ip} = \frac{1}{m}\left(k - k_c + \frac{1}{2}\left[\Delta k + \sqrt{4{k_c}^2 + \Delta k^2}\right]\right) \tag{3.14}$$

From the expressions (3.13) and (3.14), it can be seen that the out-of-phase and in-phase eigenvalues never intersect and will diverge if a stiffness imbalance, Δk, is introduced to the system. Fig. 3.4 demonstrates the eigenvalue response of a 2-DOF system to a stiffness perturbation, using nominal values of $k = 1$ and $m = 1$. It can be seen that the eigenvalues do not intersect and diverge in response to a stiffness perturbation. The influence of the coupling spring can be seen, with a weaker value for k_c resulting in a narrower veering zone (i.e. a smaller separation of the two eigenvalues for $\Delta k = 0$) and more severe eigenvalue divergence in response to a perturbation.

Remembering that $\lambda_{\mathrm{i}} = {\omega_{\mathrm{i}}}^2$, from (3.13) and (3.14) the following expressions for the out-of-phase (ω_{op}) and in-phase (ω_{ip}) mode frequencies can be calculated

$$\omega_{op} = \sqrt{\frac{1}{m}\left(k - k_c + \frac{1}{2}\left[\Delta k - \sqrt{4{k_c}^2 + \Delta k^2}\right]\right)} \tag{3.15}$$

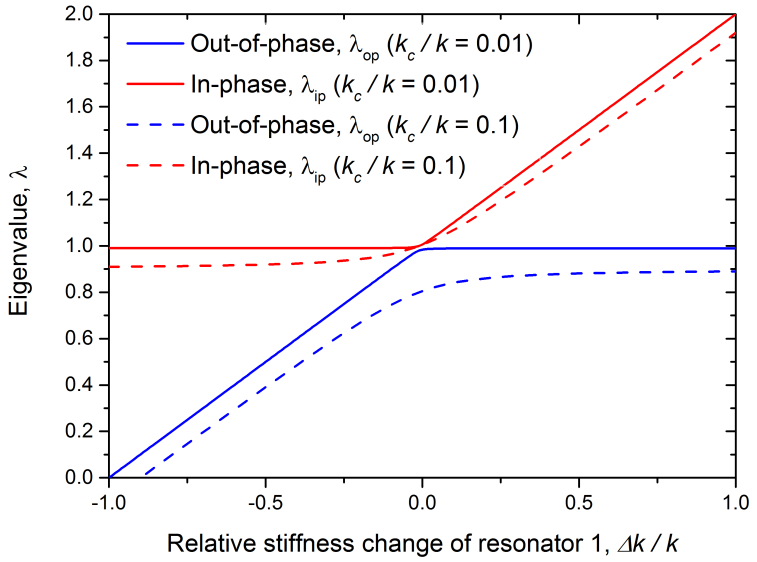

FIGURE 3.4: Out-of-phase and in-phase eigenvalues (λ_{op} and λ_{ip}) for 2-DOF system with relative stiffness perturbation, $\Delta k/k$. The response of two different coupling spring constants is shown.

$$\omega_{ip} = \sqrt{\frac{1}{m}\left(k - k_c + \frac{1}{2}\left[\Delta k + \sqrt{4{k_c}^2 + \Delta k^2}\right]\right)} \tag{3.16}$$

3.4.2 Amplitude ratios of a perturbed system

The amplitude ratio shift, as a function of stiffness perturbation, at the out-of-phase and in-phase modes has been derived from (3.1). A stiffness perturbation, Δk, has been added to resonator 1, which is driven by a force, F, and a minus sign has been included for the electrostatic coupling spring, k_c, so that the equations become

$$\begin{aligned} m\ddot{x_1} + (k + \Delta k)x_1 - k_c(x_1 - x_2) &= F \\ m\ddot{x_2} + kx_2 - k_c(x_2 - x_1) &= 0 \end{aligned} \tag{3.17}$$

A Laplace transform has been performed to obtain the following

$$\begin{aligned} X_1(s)H_1(s) + k_c X_2(s) &= F(s) \\ X_2(s)H_2(s) + k_c X_1(s) &= 0 \end{aligned} \tag{3.18}$$

where $H_1(s)$ and $H_2(s)$ are given by

$$\begin{aligned} H_1(s) &= ms^2 + (k + \Delta k) - k_c \\ H_2(s) &= ms^2 + k - k_c \end{aligned} \tag{3.19}$$

The response of the displacements as a function of the driving force have been derived

from (3.18) as follows

$$\frac{X_1(s)}{F(s)} = \frac{H_2(s)}{H_1(s)H_2(s) + {k_c}^2} \tag{3.20}$$

$$\frac{X_2(s)}{F(s)} = \frac{-k_c}{H_1(s)H_2(s) + {k_c}^2} \tag{3.21}$$

If (3.20) and (3.21) are combined, and an inverse Laplace transform performed, the following expression for the amplitude ratio is obtained

$$\frac{X_1(j\omega)}{X_2(j\omega)} = \frac{-m\omega^2 + k - k_c}{-k_c} \tag{3.22}$$

The expressions for ${\omega_{op}}^2$ and ${\omega_{ip}}^2$ are obtained from (3.13) and (3.14) respectively and are substituted into (3.22) to give the following

$$\frac{X_1(j\omega_{op})}{X_2(j\omega_{op})} = \frac{\Delta k - \sqrt{4{k_c}^2 + \Delta k^2}}{2k_c} \tag{3.23}$$

$$\frac{X_1(j\omega_{ip})}{X_2(j\omega_{ip})} = \frac{\Delta k + \sqrt{4{k_c}^2 + \Delta k^2}}{2k_c} \tag{3.24}$$

The relationship between stiffness perturbation and the amplitude ratio of a 2-DOF system described by (3.23) and (3.24) has been plotted in Fig. 3.5. Nominal values of $k = 1$ and $m = 1$ have been used. It can be seen that for each mode (out-of-phase and in-phase), the response of the amplitude ratio differs greatly depending on whether the stiffness change on resonator 1 is positive or negative. If it is desired to measure a positive stiffness perturbation, then the in-phase amplitude ratio should be measured, as a greater response is exhibited. Conversely, for a negative stiffness perturbation, the response of the out-of-phase amplitude ratio should be characterised. In order to measure a stiffness perturbation that could be either positive or negative, then it would be necessary to introduce an initial stiffness perturbation to the coupled system, as operating around the balanced state of $\Delta k = 0$ would result in a markedly different amplitude response for a positive or negative stiffness perturbation.

Fig. 3.5 demonstrates the influence of the coupling spring strength, k_c, on the response of the amplitude ratio to a stiffness perturbation, with calculations being performed with two different values for k_c, 0.1 and 0.01. It can seen clearly, that for a weaker electrostatic coupling spring, the amplitude ratio, $|x_1/x_2|$, is more sensitive to a given stiffness perturbation, $\Delta k/k$. Therefore, in the absence of other design restrictions, the weakest possible coupling should be used.

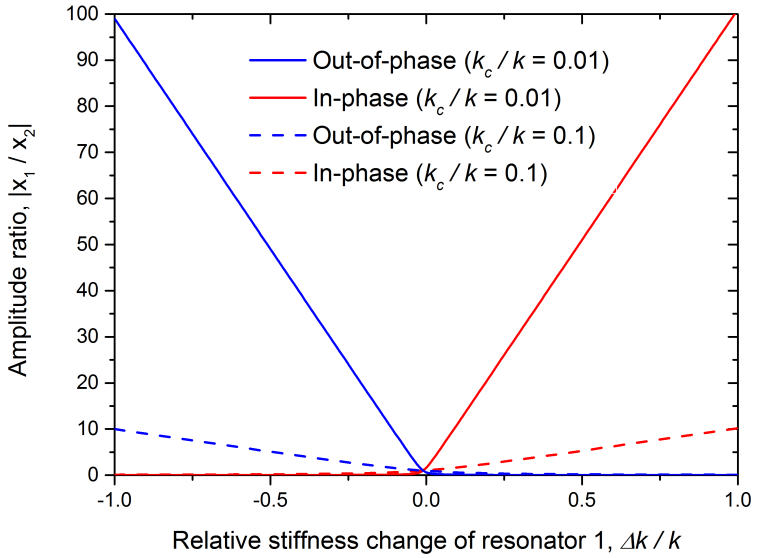

FIGURE 3.5: Response of the out-of-phase and in-phase amplitude ratios, $|x_1/x_2|$, of a 2-DOF system to a relative stiffness perturbation, $\Delta k/k$. The responses with two different coupling spring constants, $k_c = 0.1$ and $k_c = 0.01$, are shown.

However, for smaller perturbations ($\Delta k/k < 0.01$), the amplitude ratio response to either a positive or negative stiffness perturbation can be assumed to be linear, as shown in Fig. 3.6. Given that the aim of the research presented in this thesis is to detect the smallest stiffness perturbation possible, it is intended that fabricated devices will operate in this linear region.

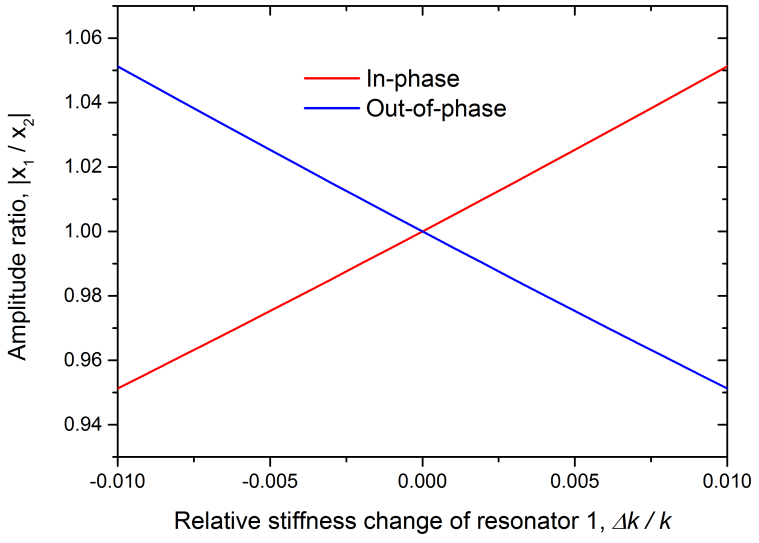

FIGURE 3.6: Response of the out-of-phase and in-phase amplitude ratios, $|x_1/x_2|$, of a 2-DOF system to a relative stiffness perturbation, $\Delta k/k$. ($k_c = 0.1$)

The sensitivity, S_k, of a device is defined as the change in the amplitude ratio of the resonators, $\Delta(x_1/x_2)$, as a function of the relative change in the stiffness of resonator 1, $\Delta k/k$, as shown in the expression

$$S_k = \frac{\Delta(x_1/x_2)}{\Delta k/k} \tag{3.25}$$

The definition for sensitivity to stiffness change in (3.25) will be used throughout this thesis to compare devices of different designs and to compare to devices that have been reported in the literature. It is noted from (3.23) and (3.24) that the amplitude ratio response as a function of the stiffness imbalance, Δk, will be the same regardless of the initial balanced stiffness, k, of the resonators. Therefore, the sensitivity to relative stiffness, S_k, will be greater for a coupled device with resonators with a higher initial balanced stiffness, k.

3.5 Response of a 2-DOF system to a mass perturbation

3.5.1 Mode frequencies of a perturbed system

Similar analysis can be performed using the mass-spring model of Fig. 3.2, with the effect of an additional mass, Δm, on resonator 1 modelled by altering the mass matrix. The mass matrix for a 2-DOF system with an additional mass of Δm added to resonator 1 can be expressed as follows.

$$M = \begin{bmatrix} m+\Delta m & 0 \\ 0 & m \end{bmatrix} \tag{3.26}$$

If a minus sign is given to the electrostatic spring, k_c, and the calculation in (3.7) is performed with the new mass matrix (3.26) the following is obtained

$$\begin{aligned} A &= M^{-1}K \\ &= \begin{bmatrix} \frac{1}{m+\Delta m} & 0 \\ 0 & \frac{1}{m} \end{bmatrix} \begin{bmatrix} k-k_c & k_c \\ k_c & k-k_c \end{bmatrix} \\ &= \begin{bmatrix} \frac{k-k_c}{m+\Delta m} & \frac{k_c}{m+\Delta m} \\ \frac{k_c}{m} & \frac{k-k_c}{m} \end{bmatrix} \end{aligned} \tag{3.27}$$

The out-of-phase (λ_{op}) and in-phase (λ_{ip}) eigenvalues as a function of mass perturbation to resonator 1, can be calculated as

$$\lambda_{op} = \frac{1}{2}\left[\frac{(k-k_c)(m_1+m_2)}{m_1 m_2} - \sqrt{\frac{(k-k_c)^2(m_1-m_2)^2 + 4m_1 m_2 {k_c}^2}{(m_1 m_2)^2}}\right] \tag{3.28}$$

$$\lambda_{ip} = \frac{1}{2}\left[\frac{(k-k_c)(m_1+m_2)}{m_1 m_2} + \sqrt{\frac{(k-k_c)^2(m_1-m_2)^2 + 4m_1 m_2 {k_c}^2}{(m_1 m_2)^2}}\right] \tag{3.29}$$

where $m_1 = m + \Delta m$, $m_2 = m$ and $k_1 = k_2 = k$. The response of the two eigenvalues to an increasing mass perturbation, Δm, has been plotted in Fig. 3.7. Again, nominal values of k = 1 and m = 1 have been used. A similar behaviour to that seen for a stiffness perturbation (Fig. 3.4) has been calculated, with divergence of the out-of-phase and in-phase eigenvalues resulting from an increasing mass perturbation, Δm. Similarly, a narrower veering zone is observed for a weaker electrostatic coupling spring, k_c, with a more abrupt eigenvalue divergence for a given mass perturbation, Δm.

Also, it is noted that for a positive mass perturbation, the out-of-phase eigenvalue decreases while the in-phase eigenvalue remains constant, whereas for a negative mass perturbation, the opposite is true. The behaviour is reversed for the response to a stiffness perturbation, as seen earlier (Fig. 3.4).

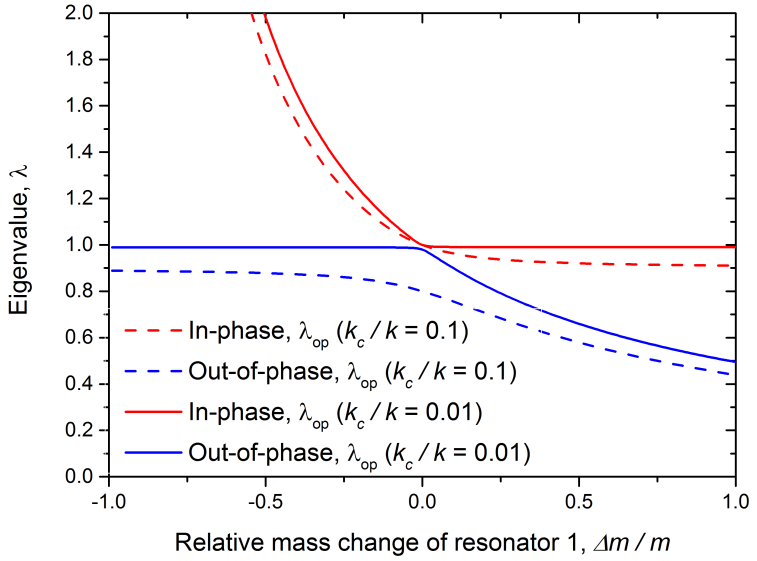

FIGURE 3.7: Out-of-phase and in-phase eigenvalues (λ_{op} and λ_{ip}) for 2-DOF system with relative mass perturbation, $\Delta m/m$. The response of two different coupling spring constants is shown.

3.5.2 Amplitude ratios of a perturbed system

The response of the amplitude ratio to a mass perturbation can be calculated from (3.1). Adding a mass perturbation, Δm, to resonator 1, which is driven by a force, F, results in the following

$$\begin{aligned} (m+\Delta m)\ddot{x_1} + kx_1 - k_c(x_1 - x_2) &= F \\ m\ddot{x_2} + kx_2 - k_c(x_2 - x_1) &= 0 \end{aligned} \tag{3.30}$$

The expression for the amplitude ratio derived previously (3.22) is valid for describing the response to mass perturbation, but it is important to specify that m is referring to m_2, so the equation becomes

$$\frac{X_1(j\omega)}{X_2(j\omega)} = \frac{-m_2\omega^2 + k - k_c}{-k_c} \tag{3.31}$$

The expressions for ${\omega_{op}}^2$ and ${\omega_{ip}}^2$ are obtained from (3.28) and (3.29) respectively and are substituted into (3.31) to give the following

$$\frac{X_1(j\omega_{op})}{X_2(j\omega_{op})} = \frac{1}{k_c}\left[k_c - k + \frac{m_2}{2}\left(\frac{(k-k_c)(m_1+m_2)}{m_1m_2} - \sqrt{\frac{(k-k_c)^2(m_1-m_2)^2 + 4m_1m_2{k_c}^2}{(m_1m_2)^2}}\right)\right] \tag{3.32}$$

$$\frac{X_1(j\omega_{ip})}{X_2(j\omega_{ip})} = \frac{1}{k_c}\left[k_c - k + \frac{m_2}{2}\left(\frac{(k-k_c)(m_1+m_2)}{m_1m_2} + \sqrt{\frac{(k-k_c)^2(m_1-m_2)^2 + 4m_1m_2{k_c}^2}{(m_1m_2)^2}}\right)\right] \tag{3.33}$$

where $m_1 = m + \Delta m$, $m_2 = m$ and $k_1 = k_2 = k$. (3.32) and (3.33) have been used to plot the response of the amplitude ratios at the two mode frequencies as a function of mass perturbation on resonator 1. If nominal values of $k = 1$ and $m = 1$ are used, then the relationship shown in Fig. 3.8 can be plotted. If a comparison is made with the amplitude ratio response to stiffness perturbation (Fig. 3.5), it can be seen that the response to a mass perturbation is the opposite, with the in-phase amplitude ratio showing a larger response if the mass of resonator 1 is decreased, and the out-of-phase amplitude ratio showing a larger response if the mass of resonator 1 is increased.

As explained in the previous section, the intention of the research presented in this thesis is to demonstrate the highest sensitivity possible, which will involve detecting very small changes in the mass of a resonator ($\Delta m/m < 0.01$). Fig. 3.9 shows that for mass perturbations across a narrower range, the response of the amplitude ratio, $|x_1/x_2|$, for both modes is linear, which is a desirable output for measurement applications.

The definition for sensitivity, S_m, for mass sensing is defined as the change in the amplitude ratio of the resonators, $\Delta(x_1/x_2)$, as a function of the relative change in the mass of resonator 1, $\Delta m/m$, as shown in the expression

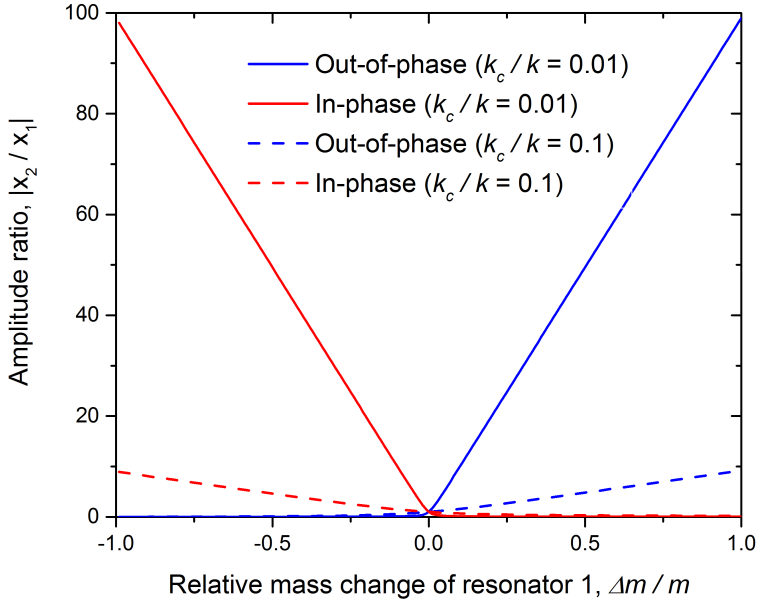

FIGURE 3.8: Response of the out-of-phase and in-phase amplitude ratios, $|x_1/x_2|$, of a 2-DOF system to a relative mass perturbation, $\Delta m/m$. The responses with two different coupling spring constants, $k_c = 0.1$ and $k_c = 0.01$, are shown.

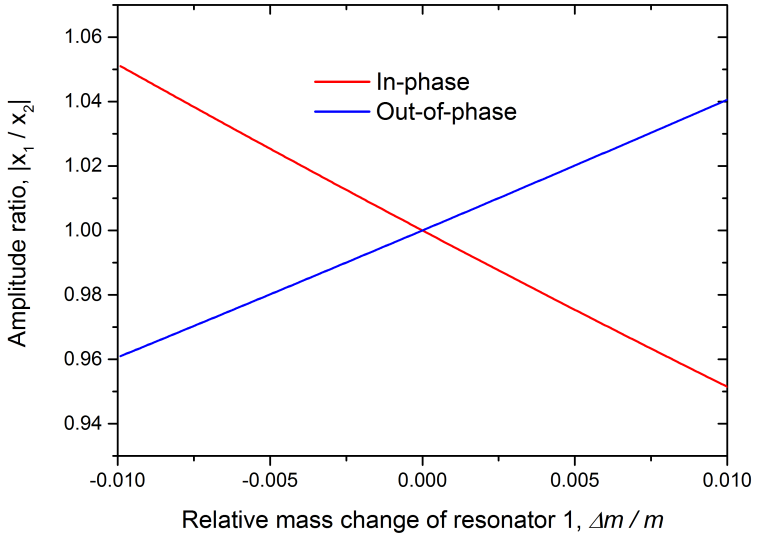

FIGURE 3.9: Response of the out-of-phase and in-phase amplitude ratios, $|x_1/x_2|$, of a 2-DOF system to a relative mass perturbation, $\Delta m/m$. ($k_c = 0.1$)

$$S_m = \frac{\Delta(x_1/x_2)}{\Delta m/m} \tag{3.34}$$

The definition for mass sensitivity is similar to (3.25) for stiffness sensitivity and allows for comparison between coupled-resonator devices of different designs and for comparison to previously reported mass sensing MEMS devices.

The next section of this chapter will detail previous research into how the change in mode shape can be exploited for sensing applications.

3.6 Previously published research into mode-localisation

This section will outline and discuss the published research concerning mode-localisation in coupled MEMS resonator systems. The first main area of previous research is the investigation of mode-localisation in MEMS structures that are mechanically coupled together. The other area that has been researched more recently is mode-localisation in MEMS resonators that are electrostatically coupled together.

A microscale mass sensor based on an array of microcantilevers has been demonstrated previously [12]. Two silicon cantilevers (length 500 μm, width 100 μm and thickness 10 μm) have been fabricated with a layer of gold on top and they have been mechanically coupled together with an overhang at the anchor, as shown in the SEM image of Fig. 3.10. The coupling overhang acts as the coupling spring, k_c, in a 2-DOF system that can be visualised using Fig. 3.2, with each cantilever possessing a mass, m, and a stiffness, k.

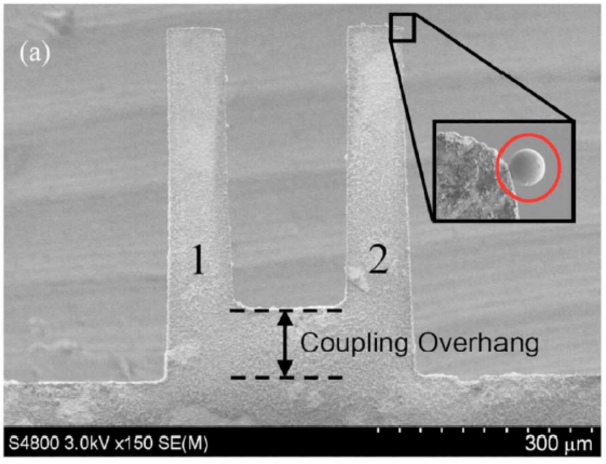

FIGURE 3.10: SEM image of mechanically coupled cantilever resonators [12]. Inset: attached microsphere.

The structure has been characterised with scanning probe microscopy where the frequency of vibration is swept from 12.5 kHz to 14.5 kHz and the vibration amplitude of each cantilever has been extracted across the frequency range. The results are presented in Fig. 3.11, with the peaks for the in-phase and out-of-phase modes being clearly identifiable, thus confirming mode-localisation behaviour.

To determine the sensitivity of the system to mass-induced disorder, microspheres made from borosilicate have been attached to one of the cantilevers (see inset of Fig. 3.10). The microspheres each had a mass of approximately 154 pg and the attachment of three to cantilever 2 induced mode-localisation. The ratio of vibration amplitude of the two cantilevers for both the in-phase and out-of-phase mode shifted as shown in the results of Fig. 3.12. The eigenstates (normalised vectors formed from the amplitudes of the two cantilevers) at each mode shifted up to 0.07 in response to the increase of mass on cantilever 2, giving a sensitivity of 30.43, defined as the change in eigenstate as a

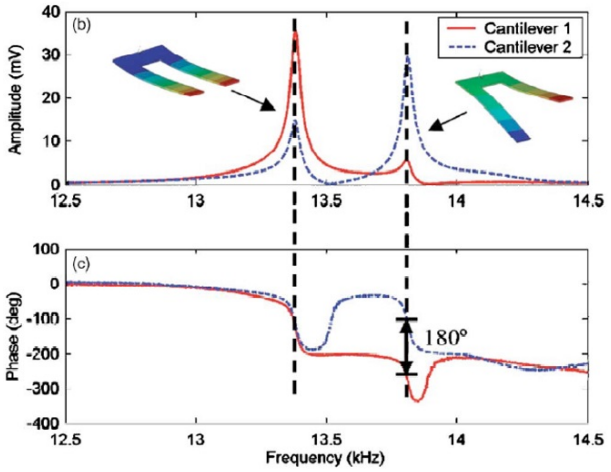

FIGURE 3.11: Amplitude/phase vs frequency for for each resonator in a mechanically coupled pair of MEMS cantilevers [12]. Representative 3D images of the in-phase and out-of-phase mode shapes are shown.

function of relative mass increase. For the same mass increase, the resonant frequency of the in-phase mode (equivalent to a 1-DOF cantilever) shifted by 0.01 %, giving a sensitivity of 0.43, which is two orders of magnitude lower than the eigenstate sensitivity, demonstrating the degree of improvement that is possible with coupled-resonator sensors.

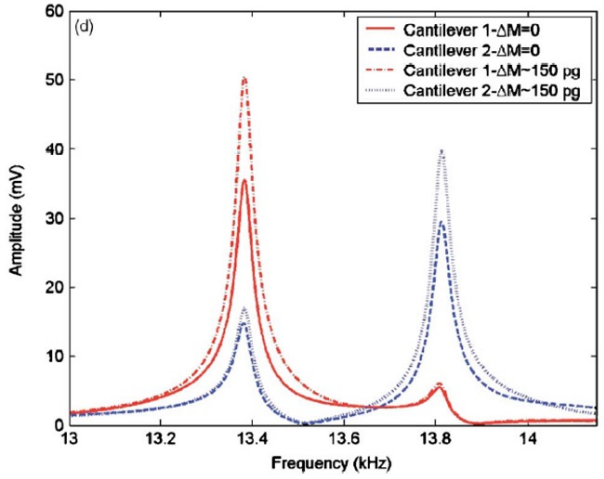

FIGURE 3.12: Amplitude vs frequency for mechanically coupled cantilever resonators before and after the addition of mass perturbation [12]

The same authors have fabricated a device consisting of an array of fifteen cantilevers all mechanically coupled together with overhangs at their anchors [95]. A single microsphere with a mass of 10 pg has been attached to one of the cantilevers and the mode shapes of the 15-DOF system have been measured optically with a laser Doppler vibrometer, as shown in Fig. 3.13. By observing the mode shape, it is not only possible to detect the attachment of the 10 pg mass to the resonator array, but also to determine which of the fifteen cantilevers the additional mass has attached to. The eigenstate shift of the 6th mode has been found to be the greatest and shows a sensitivity of 495, which is 16

times greater than that measured for the 2-DOF cantilever array [12].

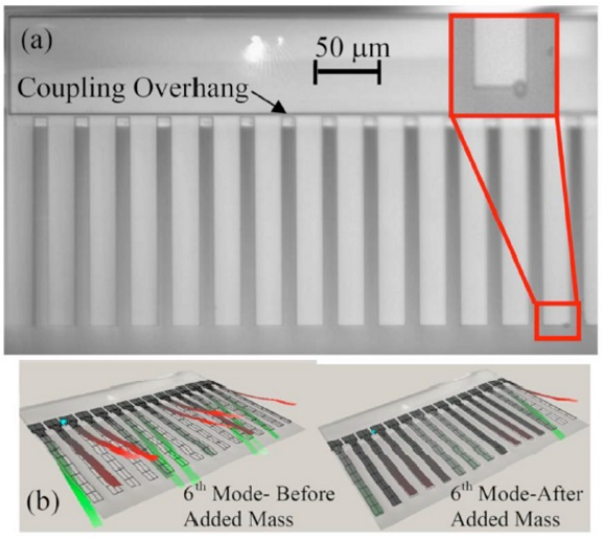

FIGURE 3.13: (a) Image of array of fifteen microcantilevers mechanically coupled together with anchor overhangs. Inset: attached microsphere. (b) Change in the 6th mode shape after the addition of mass [95]

More recently, published research has focused on the analysis of MEMS resonator arrays that are coupled together electrostatically, by biasing closely spaced (< 2 μm) resonators with DC voltages to create an electric field between them, as explained in section 3.3.1. A stiffness perturbation in an electrostatically-coupled resonator pair has been successfully measured [96], using devices of the two designs shown in Fig. 3.14. The devices have been fabricated using a silicon-on-insulator (SOI) process, with a structural layer thickness of 25 μm. While the DC voltage of the drive electrodes that are positioned alongside the resonators is held constant, the DC voltage of one of the resonators is decreased, resulting in a decrease of the potential difference between the resonator and its neighbouring drive electrode, which leads to a decrease in the electrostatic spring softening and an increase in the stiffness of the resonator. The coupled system has been actuated electrically by applying an AC signal to the drive electrodes and the mode shapes of the system have been measured using capacitive transduction while the stiffness of one of the resonators is varied.

The induced stiffness disorder causes the localisation of the mode shapes, as is shown in the graphs of Fig. 3.15, which show the measured amplitudes of each resonator. The two peaks on each graph represent the out-of-phase and in-phase modes. The experiments found that the relative shift in eigenstates (the normalised mode shapes) is larger than the shift in resonant frequency by about three orders of magnitude. The sensitivity of the amplitude ratio to relative stiffness change of 356, as defined by (3.25), has been demonstrated for the DETF design.

The same authors fabricated coupled resonators of a wine glass design and utilised them as stiffness change sensors [97, 98]. An optical image of the coupled device design is

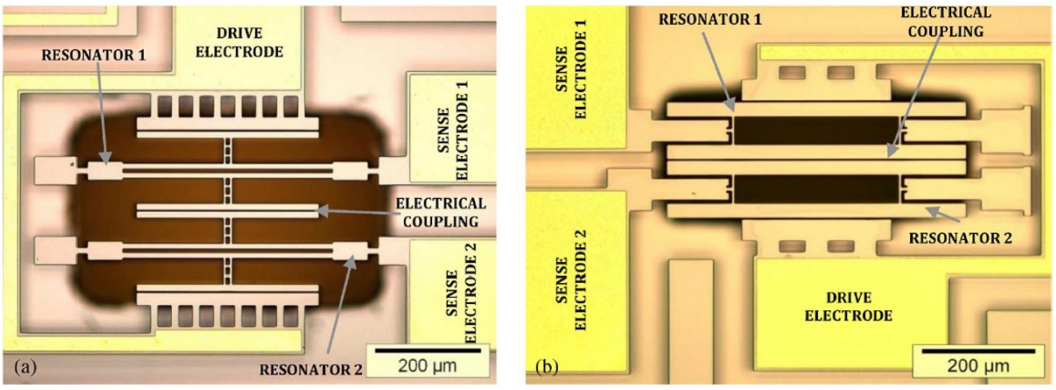

FIGURE 3.14: Optical images of electrostatically-coupled microresonators of two different architectures [96]. (a) Double-ended tuning fork (DETF). (b) Double free-free beam.

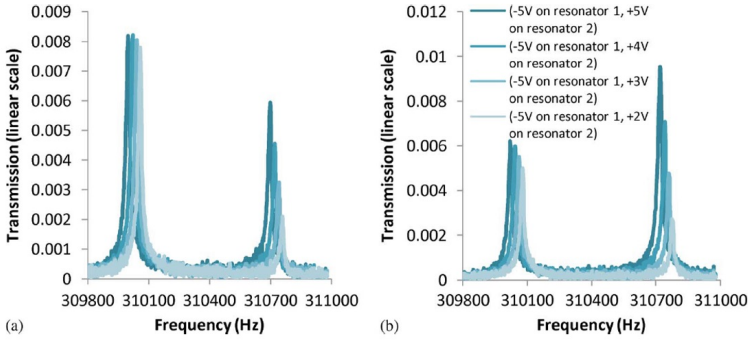

FIGURE 3.15: Frequency response of (a) resonator 1 and (b) resonator 2 while DC bias applied to resonator 2 is varied [96]

shown in Fig. 3.16, with the structural layer thickness being 10 μm.

The same actuation and sensing mechanism as before [96] has been used, with the sensitivity of the amplitude ratio to relative stiffness change determined to be 310, not as sensitive as the DETF resonator design.

A further study has employed a device of the wine-glass ring resonator design of Fig. 3.16 to demonstrate mode-localised mass sensing [99]. Patches of platinum have been deposited on one of the resonators using a focused ion beam (FIB), introducing a mass disorder to the system. The additional mass is approximately 13 pg. A change in the amplitude ratio resulted from the mass increase of resonator 1, with a sensitivity of 6367, which is superior to earlier studies, utilising mechanical coupling, that have been discussed [12, 95].

In addition, the reported work shows that the sensitivity of the device can been altered by tuning the DC voltages that determine the coupling spring, k_c. As has been predicted by the theory earlier in this chapter (Fig. 3.8), a weaker coupling spring resulted in a larger shift in amplitude ratio for same mass perturbation of 13 pg.

Other studies into the application of mode-localisation based sensing include the fabrica-

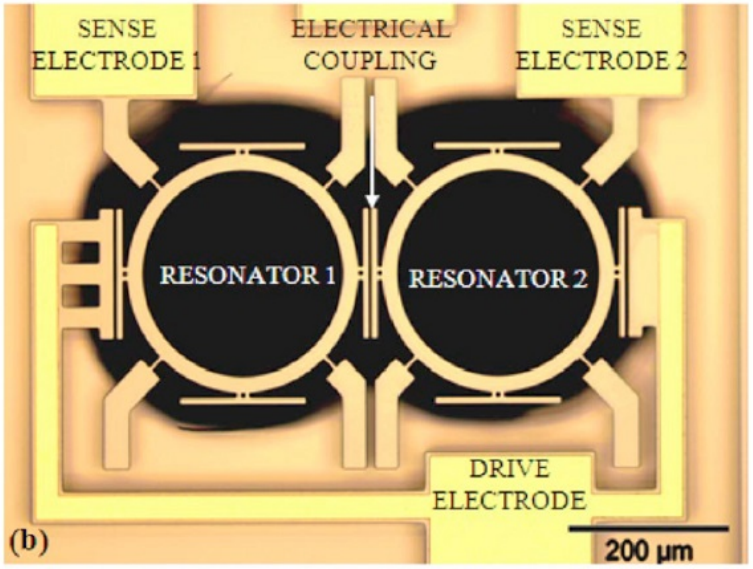

FIGURE 3.16: Optical image of coupled device of the wine glass ring resonator design [99, 97]

tion of an electrometer, a device capable of measuring precise quantities of charge [100]. The coupled device measured the stiffness change, induced by the electric charge, of one of a pair of mechanically coupled resonators of the DETF design shown in Fig. 3.14. The sensitivity of the amplitude ratio to stiffness change is 241. Also, electrostatically coupled DETF resonators have been used to detect the displacement of a proof mass [101]. A suspended silicon proof mass is positioned next to one of the resonators and is biased with a DC voltage, creating a potential difference with respect to the neighbouring resonator. Any displacement of the proof mass will change the gap between it and the resonator, altering the electrically induced spring softening. The stiffness disorder caused by the displacement has been measured through extraction of the amplitude ratio of the coupled resonator pair, with a sensitivity of 217.

Tab. 3.1 summarises all the mode-localised mass and stiffness sensing in the literature that has been discussed in this section. The values that are given for the minimum detected change refer to the minimum change that the researchers have been able to demonstrate, which would have been limited to the smallest mass that would be practical to attach or the smallest stiffness change that could be induced.

3.7 Summary

This chapter has explained the theory behind mode-localisation in coupled MEMS resonators and its application in detecting mass or stiffness change. Mode-localised sensing has been shown in the literature to be superior to resonant-shift based sensing in terms of sensitivity. Therefore, mode-localised sensing offers improvement over the devices discussed in chapter 2.

Reference	Design	Quantity measured	Sensitivity defined by (3.25) and (3.34)	Minimum detected change (Δm or $\Delta k/k$)
[12]	Cantilever	Mass	30.43	154 pg
[95]	Cantilever	Mass	495	10 pg
[99]	Wine glass ring	Mass	6367	13 pg
[96]	DETF	Stiffness change	356	0.000266
[97]	Wine glass ring	Stiffness change	310	0.000339
[100]	DETF	Stiffness change	241	0.0000141
[101]	DETF	Stiffness change	217	0.0000922

TABLE 3.1: Comparison of previously reported MEMS coupled-resonator sensors.

An additional advantage of mode-localised sensing is inherent common-mode rejection, as any environmental influence will affect both resonators equally. An advantage of electrostatically coupled resonators, rather than those that are mechanically coupled, is that weaker coupling is possible.

The theory and previously reported research in this chapter have shown that weaker coupling increases the sensitivity of the amplitude ratio to mass or stiffness perturbation. Also, in contrast to a mechanical spring, for electrostatically coupled resonators, the coupling spring stiffness is controlled by the applied bias voltages allowing for instantaneous adjustment.

From the studies that have been summarised in this chapter, it has been found that in the field of sensors based on electrostatically coupled MEMS resonators, only a handful of device designs have been explored. Therefore, there is need of some study into alternative design architectures and study into the influence of various device dimensions on sensor performance, which will be the focus of the rest of this thesis.

Chapter 4

Design and fabrication of devices

4.1 Introduction

This chapter will outline the two fabrication processes that have been used to create coupled-resonator devices. Fabrication has been performed using two different fabrication methods - one at the University of Southampton, the other in partnership with Northwestern Polytechnical University (NPU), Xi'an, China. An overview of the fabrication steps for each of the two fabrication processes will be outlined, along with the design rules that must be adhered to in order to produce coupled MEMS resonator structures successfully.

With the design rules established, theoretical calculations have been performed in order to establish the dimensions of the devices to be fabricated. Different device dimensions and architectures have been designed for different devices to allow for the effect of various dimension changes on the device sensitivity to stiffness or mass change.

After the designs of the coupled resonator devices have been established, the work that has been performed to produce a batch of functional devices will be detailed, including some of the challenges that had to be overcome.

4.2 Southampton fabrication process

The first fabrication process that has been used to fabricate coupled MEMS resonator devices has been reported previously [13], having been developed using the facilities of the Southampton Nanofabrication Centre. The process begins with a silicon-on-insulator (SOI) wafer of diameter 150 mm with a handle layer thickness of 560 μm. The wafer has a silicon structural layer of thickness 50 μm and a buried-oxide (BOX) layer of thickness 3 μm. The BOX layer separates the structural layer from the silicon handle wafer,

acting as an insulator. The MEMS structures are created by patterning and etching the structural layer and the handle wafer with deep reactive ion etching (DRIE) and then using hydrofluoric acid (HF) vapour to release the structural layer and handle wafer by etching the BOX layer. Also, the process allows individual devices to be separated from one another without dicing with a saw. The fabrication process is illustrated in Fig. 4.1.

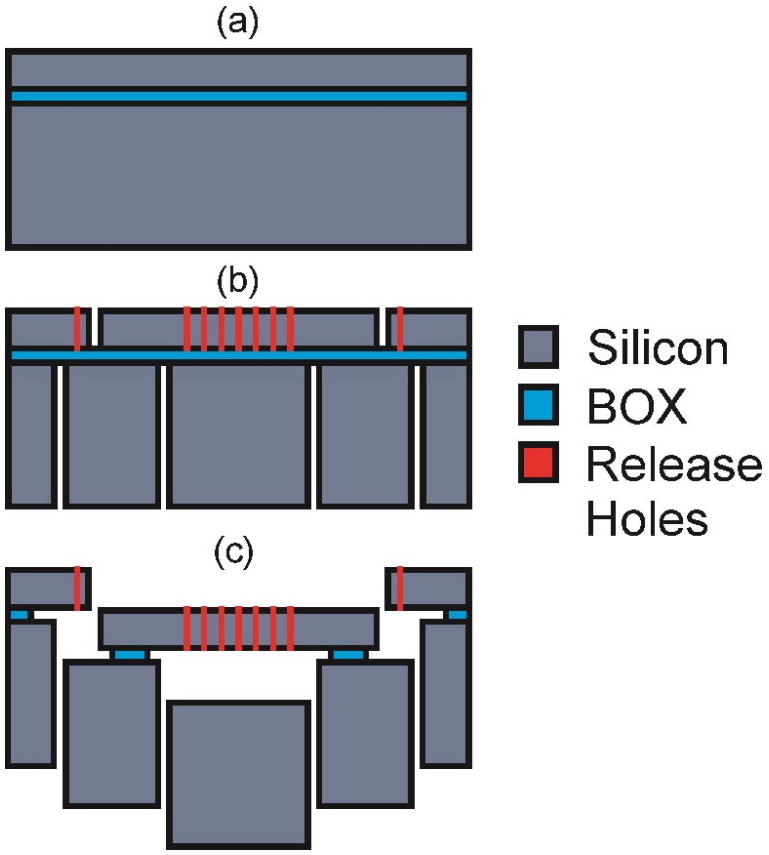

FIGURE 4.1: SOI fabrication process: (a) SOI wafer with 50 μm device layer, 3 μm BOX layer, and 560 μm handle wafer (b) DRIE of front and back side trenches and release holes (c) HF vapour etch of BOX resulting in release of resonators and device from the wafer grid, with no stiction.

The first step of the process is to deposit a 1 μm layer of silicon dioxide (SiO_2) on the device layer and a 3 μm layer on the handle layer, using plasma-enhanced chemical vapour deposition (PECVD). Then, the two oxide layers are patterned, one at a time, to form hard masks for the front and back DRIE steps. The oxide layers are each patterned, using photolithography, with a 6 μm layer of AZ9260 positive photoresist. Then, the pattern in the layer of SiO_2 is created by using inductively-coupled plasma (ICP) to etch away the parts of the oxide not protected by the photoresist. The remaining photoresist is removed in fuming nitric acid (FNA). After both of the oxide masks are patterned, DRIE is performed to create the trenches in the handle wafer (Fig. 4.1(b)). Next, DRIE is performed to create the resonator device features (Fig. 4.1(b)). An HF vapour phase etcher (VPE) is used to etch the buried oxide layer below the patterned structural layer (Fig. 4.1(c)). The oxide removal causes the handle wafer block below the released

resonator structures to fall away and the trenches are positioned in such a way that the entire device is separated from the rest of the wafer (Fig. 4.1(c)).

Any large area of the resonator structure needs to have release holes patterned through it to allow the HF vapour access to the BOX underneath (Fig. 4.1(b)). The size and spacing of he release holes is carefully designed to ensure that the resonators release first, followed by the handle block beneath the resonators. Finally, the oxide at the perimeter of the device is removed so that the entire device releases from the wafer grid.

4.3 Design of devices for the Southampton fabrication process

For the implementation of MEMS mode-localisation based sensors, several different device architectures have been designed. In this section, each design will be presented in turn. The layout of the coupled MEMS resonator structures is achieved through the design of the photomasks.

For the patterning of the oxide hard masks with photoresist, photomasks are used. A photomask is a transparent glass plate with a patterned layer of chrome on one side. First, a small amount of AZ9260 photoresist is dispensed onto the device layer side of the SOI wafer. Then, the wafer is spun at a speed of 4000 rpm to create an even 6 μm layer of photoresist across the wafer. After the photoresist layer has been spun, the wafer is placed on a hotplate at 110 °C. Now, the baked layer of photoresist is brought into contact with the photomask and is exposed to ultraviolet light. Only the photoresist in areas not protected by the chrome pattern on the mask is exposed to the UV light. After exposure, the wafer is placed in developer, which dissolves only the UV exposed photoresist, creating a patterned layer on top of the oxide. The patterned resist allows for the same pattern to be created in the oxide layer with ICP. Then, the same process is repeated for the handle layer side of the SOI wafer, resulting in patterned oxide hard masks for the front and back side DRIE.

In this section, the design of the photomasks will be outlined. The software used is Tanner Tools L-Edit.

4.3.1 Simple beams design

The initial design that has been chosen is that of two rectangular clamped-clamped beams positioned parallel to each other, separated by a coupling gap. As a result of their simple geometry, rectangular beams enable easier theoretical calculations to be performed to determine mode-localisation effects. A 3D representation of a device is

shown in Fig. 4.2 and shows the twin clamped-clamped beams along with actuation and sensing electrode positioned alongside.

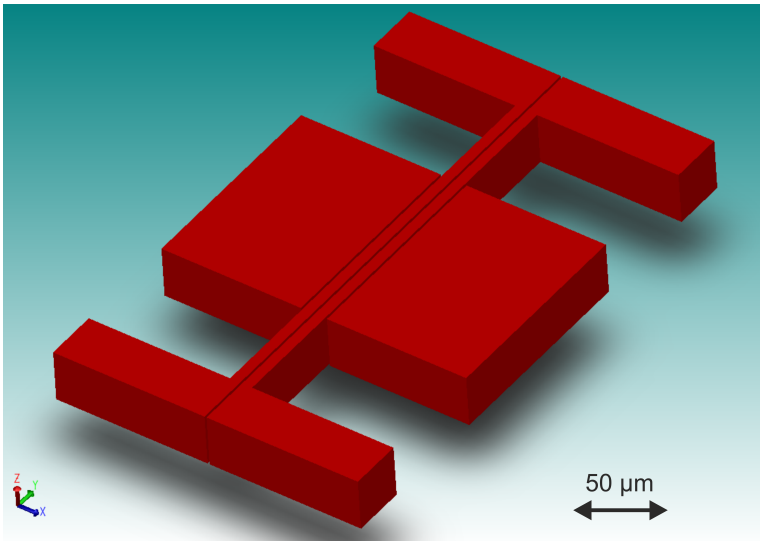

FIGURE 4.2: 3D representation of a simple two beam design. Electrodes are shown alongside the two resonators.

Fig. 4.3 shows a 3D representation of the complete device, including pads to enable wire bonding so that electrical connections can be made to the resonators and the electrodes. The beams are created by etching trenches through the device layer down to the buried oxide layer and then removing the oxide beneath the beams with HF vapour. For larger beam areas, release holes need to be etched to allow for the HF vapour to penetrate below the structure and remove the oxide. To ensure that the structures do not come into contact with the handle layer, a block of the handle layer is removed from below the structures, as shown in Fig. 4.4. The handle block shape is defined by DRIE etching of trenches through the handle wafer to the BOX.

The dimensions of the device have been optimised to allow for successful measurement of mode-localisation. As explained in chapter 3, the sensitivity of amplitude ratio to a stiffness or mass perturbation will be at its greatest when the strength of the coupling spring, k_c, is at its weakest. The lower practical limit for the coupling spring strength is the value at which there is no mode-aliasing, so it is still possible to discriminate between the out-of-phase and in-phase modes. As has been discussed in the last chapter, to avoid mode-aliasing, it is necessary to set the value of k_c such that the anti-aliasing condition of (3.11) is met. As specified in reported research [94], a value of coupling spring should be used that results in the two peaks being separated by a frequency span that is at least 2 times the value of the bandwidth of one peak.

A minimum length of 410 μm is necessary for the beam, a value determined by the design rules of the SOI process, where anchored areas require a minimum dimension of 300 μm to ensure that some underlying oxide remains after the device release with HF

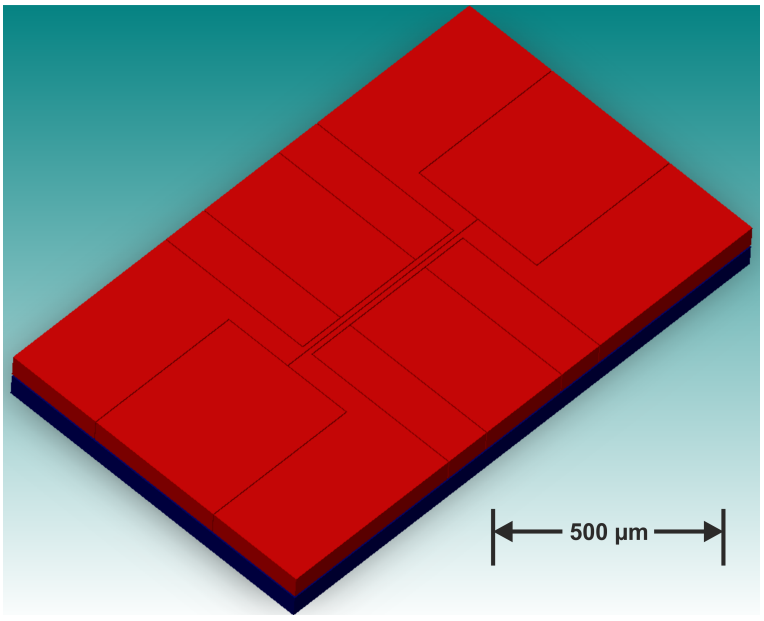

FIGURE 4.3: 3D representation of a complete device with bonding pads (red: device layer, blue: handle layer

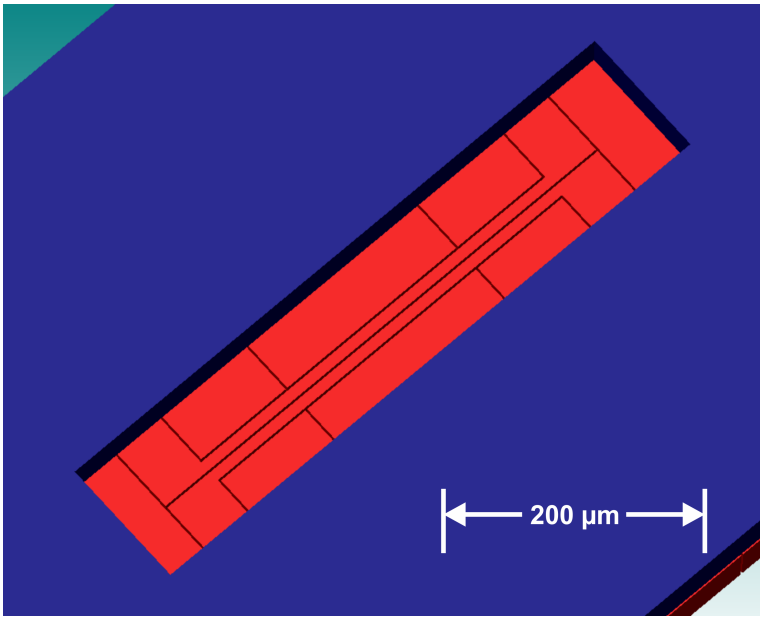

FIGURE 4.4: 3D representation of a complete device viewed from the back side (red: device layer, blue: handle layer)

vapour. The anchored area that supports the electrode will need to be at least 300 μm in length, resulting in the anchors of the beam being separated by at least 410 μm when adequate separation between the beam and electrode bonding pads is factored in.

For the beam width, the maximum value that is practically possible is determined by the maximum practical value of DC bias voltage that can be applied to the resonators

to create the coupling spring. For the equipment available, the maximum DC voltage that can be applied is ±120 V, so the maximum possible ΔV that can be implemented is 120 V. The minimum dimension that can be reliably fabricated using the SOI process is 5 μm.

For a clamped-clamped beam, its effective mass can be calculated using the following equation [35]

$$m_{1,2} = 0.4\rho AL \tag{4.1}$$

where ρ is the density of the beam material, A is the beam cross section and L is the beam length. As an example, taking a beam width of 10 μm, the effective mass, m_1 and m_2, of each beam can be calculated as follows

$$\begin{aligned} m_{1,2} &= 0.4\rho AL \\ &= 0.4 \times 2331 \text{ kg/m}^3 \times 10 \ \mu\text{m} \times 50 \ \mu\text{m} \times 410 \ \mu\text{m} \\ &= 191 \text{ ng} \end{aligned} \tag{4.2}$$

where ρ is the density of silicon (2331 kg/m^3). The effective spring constants of the beams, k_1 and k_2, have a mechanical and an electrostatic component. The mechanical stiffness is given by

$$k_{mech} = {\omega_0}^2 m \tag{4.3}$$

where the resonant frequency, ω_0, of each individual beam, is given by

$$\begin{aligned} \omega_0 &= 4.73^2 \sqrt{\frac{EI}{\rho AL}} \\ I &= \frac{1}{12} t w^3 \end{aligned} \tag{4.4}$$

where E is the Young's modulus and I is the moment of inertia of the beam. Substituting (4.4) and (4.1) into (4.3) results in the following expression for the mechanical spring constant

$$k_{mech} = \frac{16.7 E t w^3}{L^3} \tag{4.5}$$

For the example silicon beam with 410 μm length, 10 μm width and 50 μm thickness, the mechanical spring constant is calculated as

$$\begin{aligned} k_{mech} &= \frac{16.7Etw^3}{L^3} \\ &= \frac{16.7 \times 169 \text{ GPa} \times 50 \ \mu\text{m} \times (10 \ \mu\text{m})^3}{(410 \ \mu\text{m})^3} \\ &= 2047 \text{ N/m} \end{aligned} \tag{4.6}$$

From (3.10), the following expressions can be derived for the out-of-phase and in-phase mode frequencies

$$\begin{aligned} f_{op} &= \frac{1}{2\pi}\sqrt{\frac{k_{mech} - 2k_c}{m}} \\ f_{ip} &= \frac{1}{2\pi}\sqrt{\frac{k_{mech}}{m}} \end{aligned} \tag{4.7}$$

From (4.7), the in-phase mode frequency for the 10 μm wide beams can be calculated as

$$\begin{aligned} f_{ip} &= \frac{1}{2\pi}\sqrt{\frac{k_{mech}}{m}} \\ &= \frac{1}{2\pi}\sqrt{\frac{2047 \text{ N/m}}{191 \text{ ng}}} \\ &= 521.03 \text{ kHz} \end{aligned} \tag{4.8}$$

Next, a Q-factor of 10,000 is assumed, which is a safe estimate compared to previously reported values from similar devices of 13,000 and 21,000 [96]. Therefore, the bandwidth of the peak will be 52.1 Hz, so it should be separated from the out-of-phase peak by at least $2 \times 52.1 = 104.2$ Hz. Therefore, the out-of-phase frequency should be no higher than 520.926 kHz. The minimum coupling spring, k_c, that can be used is calculated from (4.7) as follows

$$
\begin{aligned}
f_{op} &= \frac{1}{2\pi}\sqrt{\frac{k_{mech} - 2k_c}{m}} \\
k_c &= \frac{k_{mech} - (2\pi f_{op})^2 m}{2} \\
&= \frac{2047 \text{ N/m} - (2\pi \times 520.926 \text{ kHz})^2 \times 191 \text{ ng}}{2} \\
&= 0.407 \text{ N/m}
\end{aligned}
\tag{4.9}
$$

The minimum trench width, g, that can be fabricated reliably using DRIE for our SOI process is 5 μm. The required potential difference, ΔV, between the two resonators is calculated from (3.9) as follows

$$
\begin{aligned}
k_c &= \frac{(\Delta V)^2 \varepsilon_0 A}{g^3} \\
\Delta V &= \sqrt{\frac{k_c g^3}{\varepsilon_0 A}} \\
&= \sqrt{\frac{0.407 \text{ N/m} \times (5\ \mu\text{m})^3}{8.85 \times 10^{-12} \times 410\ \mu\text{m} \times 50\ \mu\text{m}}} \\
&= 16.7 \text{ V}
\end{aligned}
\tag{4.10}
$$

For multiple beam widths, the value for k_c has been calculated as shown in (4.9) and the required voltage difference, ΔV, between the two resonators needed to create the necessary k_c has been calculated as shown in (4.10), producing the graph of Fig. 4.5, which shows how the required ΔV increases as a function of the beam width.

From Fig. 4.5, it can be seen that if the maximum practical value of ΔV is 120 V, and a Q-factor of 10,000 is assumed, then the maximum width of the beams that will result in the two modal frequencies being separated by at least 2 times the bandwidth of one of the peaks will be about 35 μm for devices with a coupling gap of 5 μm.

Within the limits that have been explained, variations of the dimensions of the simple two beam design have been designed to allow for the optimal dimensions to be determined during the characterisation of the fabricated devices. The layout design view from L-Edit is shown in Fig. 4.6. The dark red represents where the back side trenches are to be etched, which defines the handle block area that will be removed. The white areas show the front side trenches that define the device layer features, with the blue circles showing the release holes that allow the handle block to be released during HF vapour removal of the BOX. Fig. 4.7 shows a zoomed out image of the device complete with large areas suitable for wire bonding. The shape of the handle block can also be seen. The spacing of the release holes is designed so that the corners of the block release last,

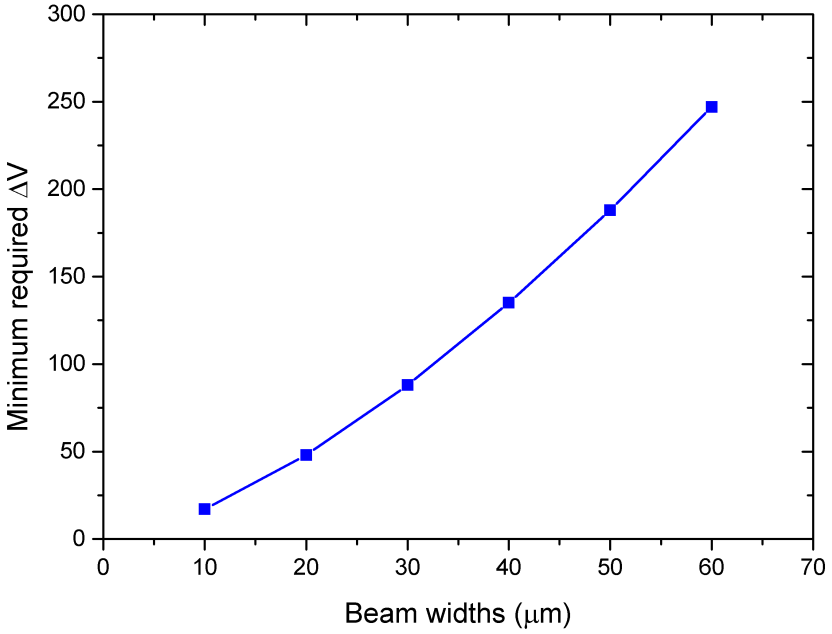

FIGURE 4.5: Minimum ΔV required to maintain adequate separation ($2 \times BW_{3dB}$) of two mode peaks for different beam widths.

protecting the resonator structures at the centre.

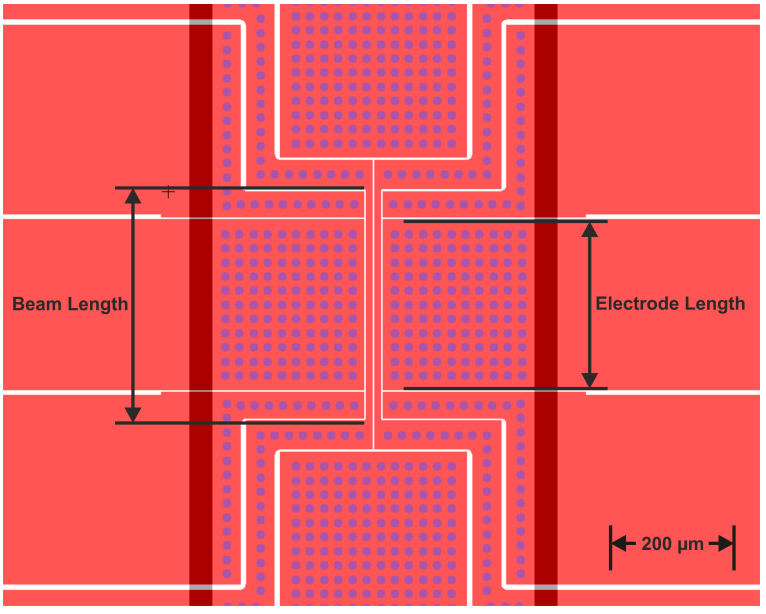

FIGURE 4.6: Photolithography mask layout for two beam coupled resonator design. White and blue: device layer. Dark red: handle layer.

Two different designs have been created by setting two different values for the beam width, 10 μm and 20 μm, while maintaining a beam length of 410 μm. An additional two designs have been created with beam lengths of 460 μm and 510 μm, while maintaining a beam width of 10 μm. All four designs are listed in Tab. 4.1.

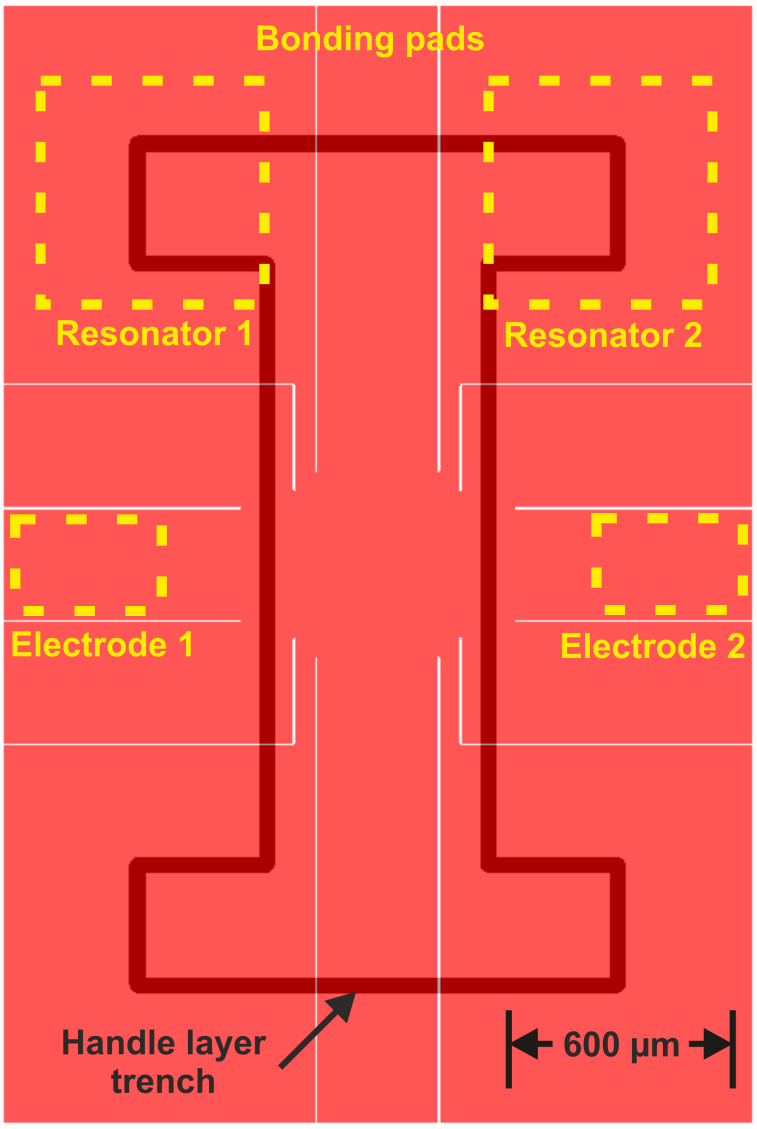

FIGURE 4.7: Photolithography mask layout showing handle block shape. The MEMS structures are located at the centre and are not visible in the zoomed out image. Locations for wire bonding are indicated by the dashed yellow boxes

For each of the device designs, the theoretical mechanical stiffness of the beams has been calculated using (4.6), with the values listed in Tab. 4.2. In addition, theoretically calculated mode frequencies are listed, assuming k_c = -20.9 N/m, which is the highest value for k_c achievable with the upper practical limit for ΔV being 120 V.

For the devices that have been designed, the effect of geometric non-linearities has been discounted. Geometric non-linearities occur as a result of the deformation of the structure during oscillation, which will change the mechanical spring constants of the resonators. However, provided that the amplitude is small enough relative to the dimensions of the resonator, which is the case for the devices that have been designed in this thesis, the non-linearities are negligible.

Device	Beam Width (μm)	Beam Length (μm)	Electrode Length (μm)
1	10	410	300
2	20	410	300
3	10	460	300
4	10	510	300

TABLE 4.1: List of two-beams device designs. Using device 1 as a reference, modifications are made to the beam width (device 2) and beam length (devices 4 and 5).

Device	k_{mech} (N/m)	f_{op} (kHz)	f_{ip} (kHz)
1	2032	513.584	518.949
2	16364	1041.31	1042.639
3	1434	411.53	417.481
4	1047	334.05	340.645

TABLE 4.2: Theoretical mechanical stiffness and mode frequencies of two-beams device designs.

4.3.2 Design of resonators with larger centre area

The second architecture that has been designed is shown in Fig. 4.8. The centre of each resonator has been widened to create a larger area that increases the utility of the device as a mass sensor, particularly a biological sensor. The design allows for a easier biological functionalisation of just one resonator and with more area, there is more opportunity for the analyte of interest to bind to the surface. As with the two beam design, the two resonators are positioned parallel to each other, separated by a coupling gap of 5 μm. Actuation and sensing electrodes are positioned alongside each resonator, with a similar gap of 5 μm.

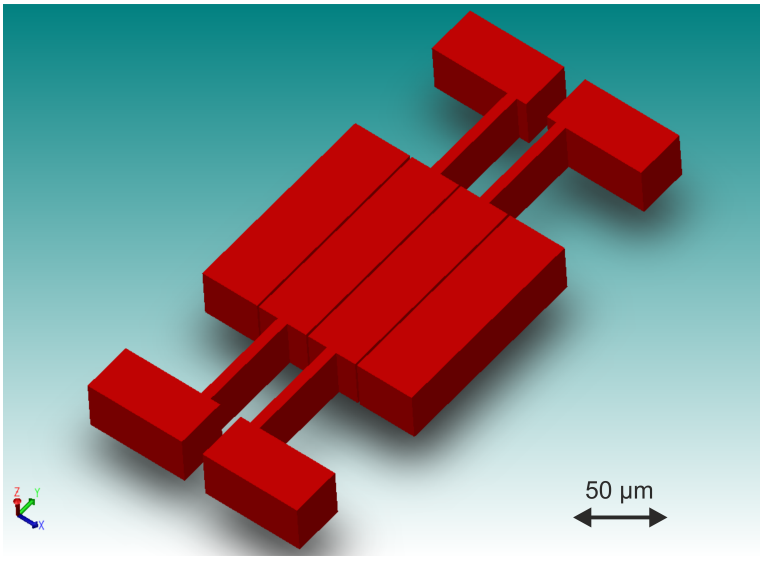

FIGURE 4.8: 3D representation of two beams with larger centre area design. Electrodes are shown alongside the two resonators.

The structures have been designed in the same way as for the two beams design. Fig. 4.9 shows the LEdit layout view of a device. As before, a minimum overall (centre area + both anchor beams) length of 410 μm is necessary, a value determined by the design rules of the SOI process. The width of the centre area will affect the ease with which biological functionalisation and mass sensing can be performed

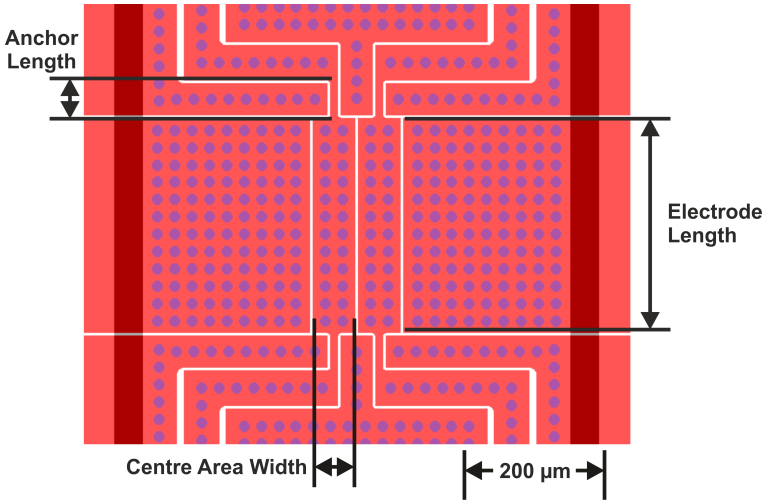

FIGURE 4.9: Photolithography mask layout for coupled resonators with a centre area design. White and blue: device layer. Dark red: handle layer.

In order to calculate the mechanical stiffness of the resonators, the centre area is assumed to be a point mass with the two anchor beams on either side, which allows for a calculation based on a simple beam. The mechanical stiffness can be calculated by modifying (4.6) to give

$$k_{mech} = \frac{16.7 E t {w_a}^3}{(2L_a)^3} \tag{4.11}$$

where L_a and w_a is the anchor beam length and width, respectively. As the anchor beams are short, relative to the overall length of the resonator, a width of 10 μm has been chosen to minimise the stiffness. Calculations have been performed in order to determine the optimal length of the anchor beams. The graph of Fig. 4.10 shows how the anchor length affects the minimum required ΔV necessary to maintain adequate separation of the two modal frequencies. As explained previously, the upper practical limit for ΔV is 120 V. From Fig. 4.10, it can be seen that, for devices with a 5 μm coupling gap, the minimum permissible anchor length is about 60 μm.

In order to experimentally determine the optimal structure dimensions, variations of the dimensions have been designed, within the limits that have just been discussed. Five different designs have been created by setting different values for centre area width (60,

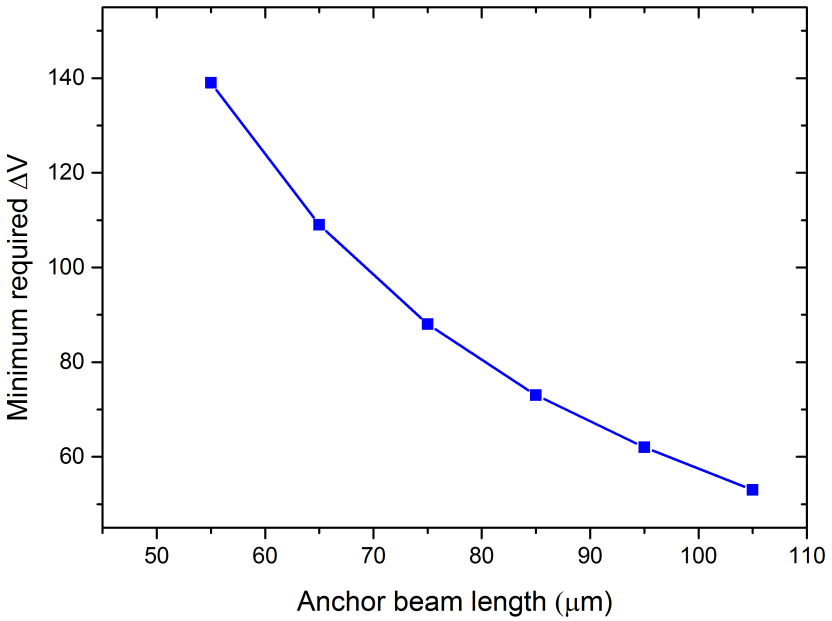

FIGURE 4.10: Minimum ΔV required to maintain adequate separation of two mode peaks for different anchor beam lengths.

85 and 110 μm) and anchor beam length (55, 80 and 105 μm). The centre area length has been held at 310 μm. The designs are listed in Tab. 4.3.

Device	Centre Area Width (μm)	Anchor Beam Length (μm)	Electrode Length (μm)
1	60	105	310
2	85	105	310
3	110	105	310
4	60	55	310
5	60	80	310

TABLE 4.3: List of device designs with larger area at centre of resonator. Modifications are made to the centre area width and anchor beam length.

As with the two-beams design, the theoretical mechanical stiffness of the resonators for each design in Tab. 4.3 has been calculated. The values have been calculated using (4.11) and are listed in Tab. 4.4. In addition, theoretically calculated mode frequencies are listed, assuming k_c = -15.8 N/m, which is the highest value for k_c achievable with the upper practical limit for ΔV being 120 V.

4.4 Theoretical amplitude ratio response to perturbation for Southampton devices

For the model designs described in the previous section, the mode-localisation behaviour that would be expected according to the theory in chapter 3 has been calculated. The

Device	k_{mech} (N/m)	f_{op} (kHz)	f_{ip} (kHz)
1	15238	420.349	420.786
2	15238	353.581	353.949
3	15238	310.928	311.251
4	106021	1099.843	1100.007
5	34452	623.404	623.69

TABLE 4.4: Theoretical mechanical stiffness and mode frequencies of device designs with larger area at centre of resonator.

response of the amplitude ratio to a stiffness perturbation on resonator 1 has been calculated and plotted for all the device designs that are to be fabricated. The following section details the expected behaviour of the devices according to theory, with the aim of the providing a reference for comparison with the measured results from fabricated devices, discussed in the results chapters later in this thesis.

The resolution of the devices, which is defined as the smallest change in the stiffness or mass that can be measured, is dictated by the noise, which will be determined when the fabricated devices are characterised later in this thesis. The noise that is present in the output signal of the system will be as a result of thermomechanical noise in the resonators and electrical noise in the measurement circuitry.

4.4.1 Simple beams design

The influence of the coupling spring constant, k_c, on the mode-localisation behaviour has been calculated for the device with two coupled clamped-clamped beams with a length of 410 μm and a width of 10 μm (device 1 in Tab. 4.1). A stiffness increase, Δk, has been added to resonator 1 and the resulting in-phase amplitude ratio has been calculated according to (3.24). The response of the in-phase amplitude ratio to an increasing stiffness perturbation, Δk, has been plotted in Fig. 4.11 for two different values of k_c, 20.9 N/m and 11.75 N/m, created by values for ΔV of 120 V and 90 V, respectively. It can be seen that, for a given stiffness perturbation, Δk, a weaker coupling spring will result in a greater change in the amplitude ratio.

The influence of beam width on the amplitude ratio response of a coupled device has been determined by performing similar theoretical analysis on the models of devices 1 and 2 from Tab. 4.1. A value of 20.9 N/m has been used for k_c for both device models. The two devices have beam widths of 10 μm and 20 μm and the difference in the amplitude ratio response to a relative stiffness change, $\Delta k/k$, can be seen in the graphs of Fig. 4.12. It can be seen that the device sensitivity to a relative change in stiffness should be greater for a coupled resonator pair with a higher initial balanced stiffness, as explained previously in chapter 3.

Using the theoretical amplitude ratio response shown in Fig. 4.12, the sensitivity of the

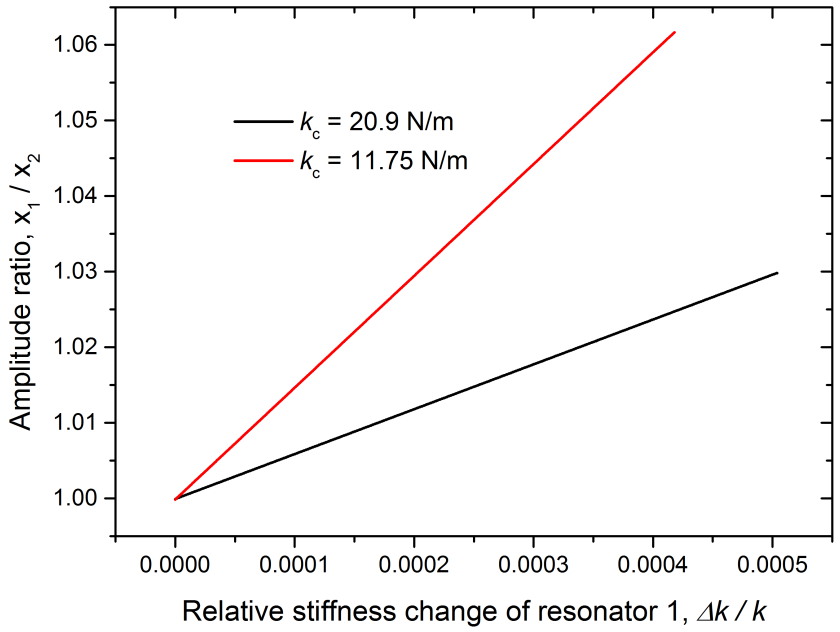

FIGURE 4.11: Theoretical response of amplitude ratio to a relative stiffness change on resonator 1 for two different coupling spring strengths, k_c.

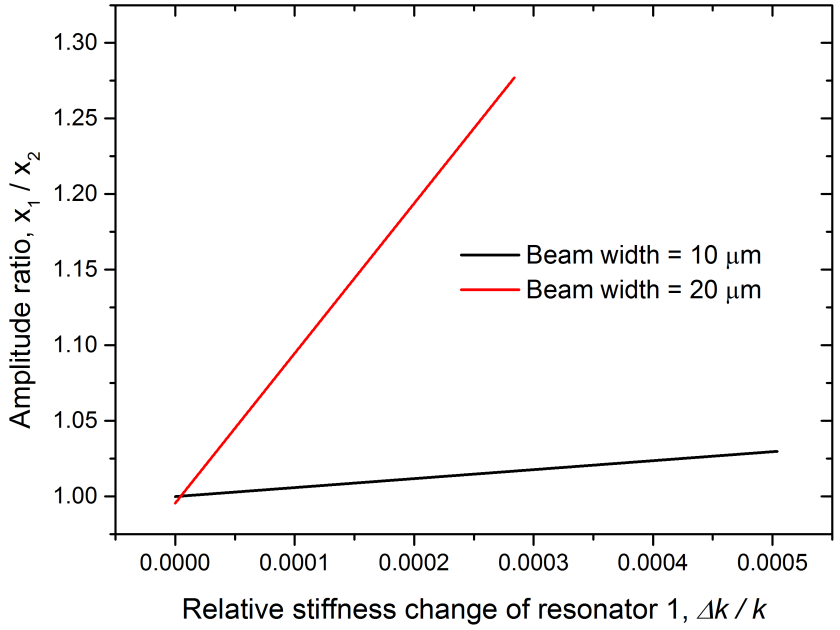

FIGURE 4.12: Theoretical response of amplitude ratio to a relative stiffness change on resonator 1 for two different beam widths.

two device models has been calculated using (3.25). The device with 10 μm wide beams has a sensitivity of 59.3, while the device with 20 μm beams has a sensitivity of 990, which is 16.7 times greater.

Next, theoretical analysis has been performed with models of coupled clamped-clamped beams of different lengths. Devices 1, 3 and 4 from Tab. 4.1 have been analysed with

beam lengths of 410 μm, 460 μm and 510 μm, respectively. The beam width has been maintained at 10 μm and a coupling spring, k_c, of 20.9 N/m has been used. The response of the amplitude ratio to a relative stiffness increase on resonator 1 is shown in Fig. 4.13 for each of the three devices.

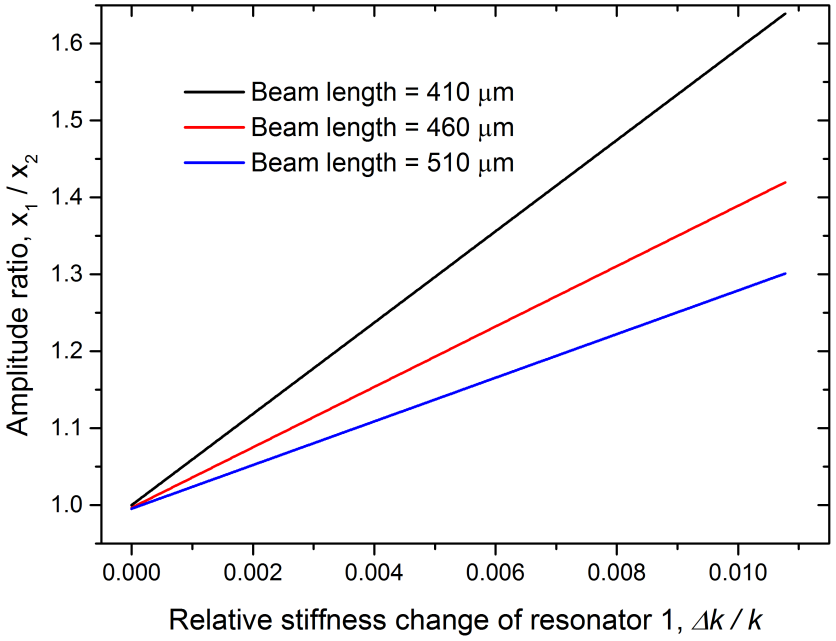

FIGURE 4.13: Theoretical response of amplitude ratio to a relative stiffness change on resonator 1 for three different beam lengths.

As explained in chapter 3, the sensitivity of a coupled resonator device, as defined in (3.25), will increase as beam length decreases because a shorter beam has a higher mechanical stiffness. The relationship between beam length and sensitivity can be seen clearly in Fig. 4.13, with the shorter beams showing a greater amplitude ratio response to relative stiffness perturbation.

4.4.2 Larger centre area design

The device designs that are listed in Tab. 4.3 have been theoretically analysed to determine the response of the amplitude ratio to a stiffness perturbation. First, designs of the device with a larger centre area with different anchor lengths have been analysed (devices 1, 4 and 5 in Tab. 4.3). Fig. 4.14 allows for a comparison of three different devices of the larger centre area design, with anchor beam lengths of 55, 80 and 105 μm.

It can be seen that, as with the clamped-clamped beam devices, the sensitivity to relative stiffness change is greatest for the device with the highest mechanical stiffness, which in this case is the device with the shortest anchor beams.

It is expected that the response of the amplitude ratio to a stiffness perturbation will be the same for devices with different widths of the centre mass area. Analysis has

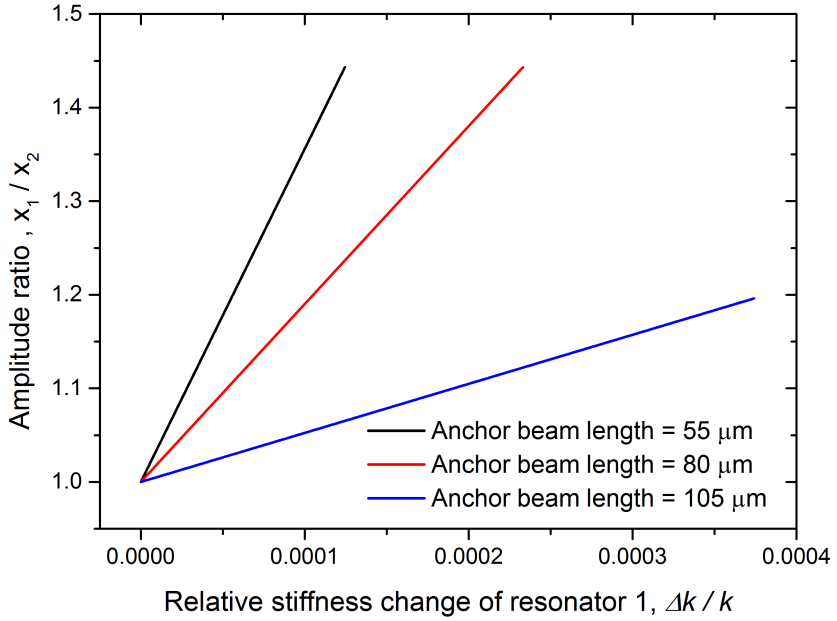

FIGURE 4.14: Theoretical response of amplitude ratio to a relative stiffness change on resonator 1 for three different anchor beam lengths.

been performed on three different device designs (devices 1, 2 and 3 in Tab. 4.3), which have centre area widths of 60, 85 and 110 μm with the anchor beam width maintained at 105 μm. As expected, the theoretical response of the amplitude ratio to a stiffness perturbation is the same for all three designs and is represented by the blue graph in Fig. 4.14.

In addition to the response to a stiffness perturbation, the response of the amplitude ratio to a mass change of resonator 1 has been calculated for device design 1 (Tab. 4.3). A primary motivation for including the larger centre area in the design is to facilitate mass sensing, therefore it is intended to perform mass sensing experiments on a device of design 1 later in this thesis. From Fig. 4.15, it can be seen that the response of the amplitude ratio change to a mass change is greater when a weaker coupling spring, k_c, of 8.88 N/m is used, rather than a k_c of 15.8 N/m.

Theoretically derived amplitude ratio responses will be compared to FEM simulated results in the next chapter and finally compared to experimental results from the characterisation of fabricated devices. The fabrication that has been performed to produce the devices will be detailed in the next section.

4.5 Fabrication of devices using the Southampton process

This section will detail the fabrication work that has been performed at the Southampton Nanofabrication Centre to produce the coupled MEMS resonator devices that have been

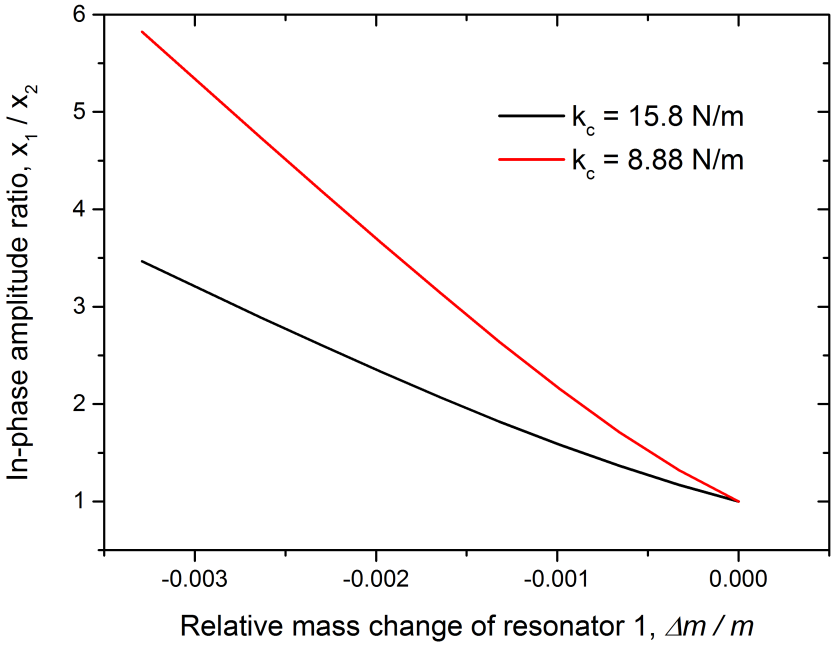

FIGURE 4.15: Theoretical response of amplitude ratio to a relative mass change on resonator 1 for device design 1.

designed in this chapter. Each step of the fabrication will be explained and work that has been performed will be detailed.

The fabrication process used to produce coupled MEMS resonators has been detailed earlier in this chapter and is shown in Fig. 4.1. For the MEMS devices of this work, the starting material is an SOI wafer with a diameter of 150 mm. The device layer thickness is 50 μm, the buried oxide (BOX) layer thickness is 3 μm and the handle layer thickness is 560 μm. In addition, several plain Si wafers have been processed and are used to characterise the various fabrication steps before they are performed on the SOI wafer.

4.5.1 Preparation of oxide hard masks

The first fabrication procedure to be performed is to deposit and pattern layers of SiO_2 on the front and back side of the SOI wafer. These patterned layers act as masks during the DRIE of the front and back side Si layers of the wafer. The oxide has been deposited using plasma-enhanced chemical vapour deposition (PECVD).

An Oxford Instruments Plasma Technology (OIPT) Plasmalab System 100 PECVD deposition tool has been used to deposit a layer of oxide with a thickness of 1 μm on the 50 μm device layer of the SOI wafer. The DRIE has shown an oxide mask selectivity of between 150 and 180, so a 1 μm mask will allow for 50 μm to etch with mask material left behind. The DRIE recipe is modified for the final 2 to 3 μm of etching to ensure a notch free finish. The notch free recipe etches the oxide mask faster than the normal

etch and the additional mask material allows for a finishing DRIE etch to be performed with a comfortable safety margin.

In order to pattern the oxide layer, a layer of photoresist is used. A 6 μm layer of AZ9260 positive photoresist is spin coated onto the wafer at 4000 rpm. Then, the wafer is baked at 120 °C for 2 minutes to harden the resist. The wafer is positioned in a mask aligner, along with the device layer mask, and the photoresist is exposed to UV light for 10 seconds. Only those areas not protected by the mask are exposed. Then, the wafer is placed in a solution of 1:4 AZ400K developer and deionised water for 5 to 6 minutes. The exposed areas of the photoresist are removed by the developer, leaving behind a patterned mask on top of the oxide, as shown in Fig. 4.16.

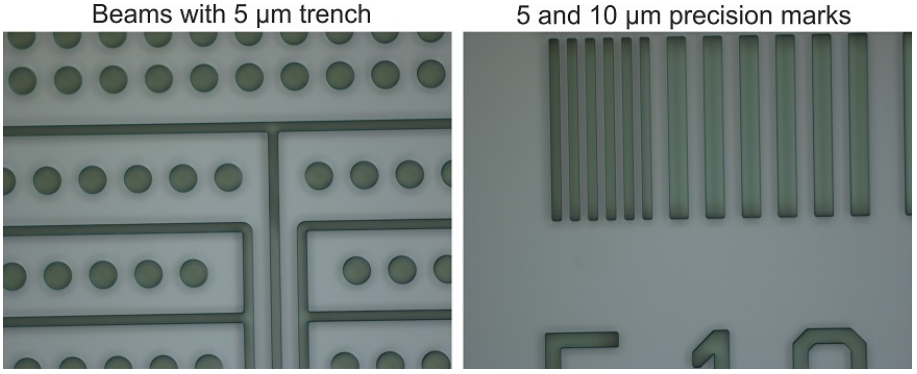

FIGURE 4.16: AZ9260 photoresist pattern on oxide of device layer

Using an OIPT Plasmalab 80+ reactive ion etcher (RIE), a low power (100 W) oxygen plasma is used to clean the trenches and holes of any remaining resist. Then, the oxide is etched using an OIPT Plasmalab System 100 inductively-coupled plasma (ICP) 380 etcher. The progress of the etch is monitored optically, as shown in Fig. 4.17, and is complete after 6 minutes. The etch is complete when the 5 μm precision marks are clear of oxide (Fig. 4.18), as this is the critical dimension of the devices.

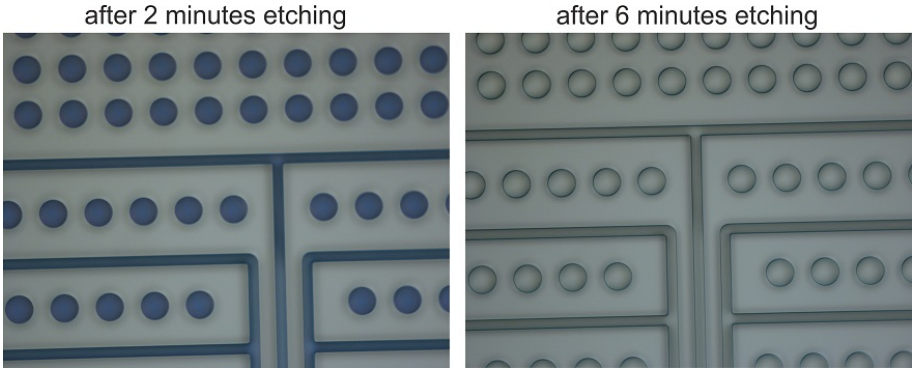

FIGURE 4.17: ICP etching of oxide mask for SOI device layer

The same procedure has been carried out for the back side of the SOI wafer, but with a thicker oxide layer. The handle layer thickness is 560 μm, so to ensure that there is

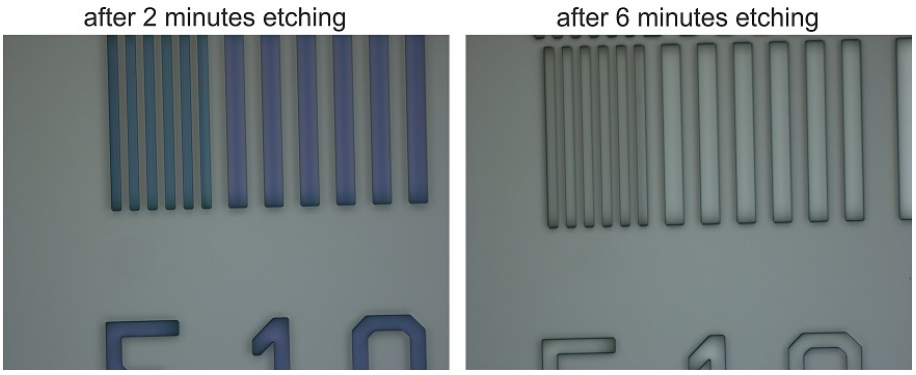

FIGURE 4.18: Precision marks showing ICP etching of oxide mask for SOI device layer

enough oxide to allow for the DRIE etch, a thickness of 3.8 μm has been deposited. As before, the oxide has been patterned with a layer of AZ9260 photoresist, with the handle layer mask being aligned with the pattern on the device layer using back side alignment (BSA). For the alignment, images are taken of the back side mask alignment marks. Then, viewing the wafer from the front side, the front side alignment marks are aligned with the image of the back side alignment marks.

Fig. 4.19 shows the precision marks on the back side during etching. The smallest feature size on the back side is a 40 μm trench, and it can be seen that the 10 μm features have been etched after 12 minutes, meaning that the 40 μm trenches will have been patterned, as shown in Fig. 4.20.

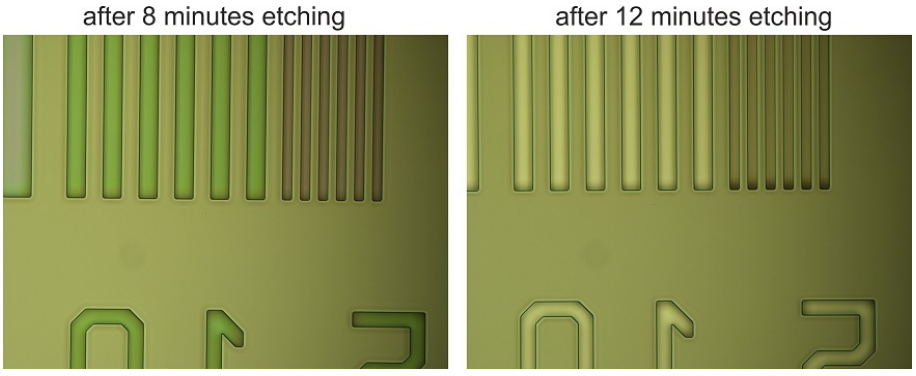

FIGURE 4.19: Precision marks showing ICP etching of oxide mask for SOI handle layer

4.5.2 Deep reactive ion etching (DRIE)

The next step, after the front and back side oxide hard masks have been deposited and patterned, is the DRIE of the device and handle layers. The Si etching of the front side pattern and the back side trenches has been performed with a PlasmaTherm Versaline Deep Silicon Etcher (DSE). The tool is capable of etching deep high aspect ratio features in silicon using the Bosch process. The first step of the process is the isotropic deposition

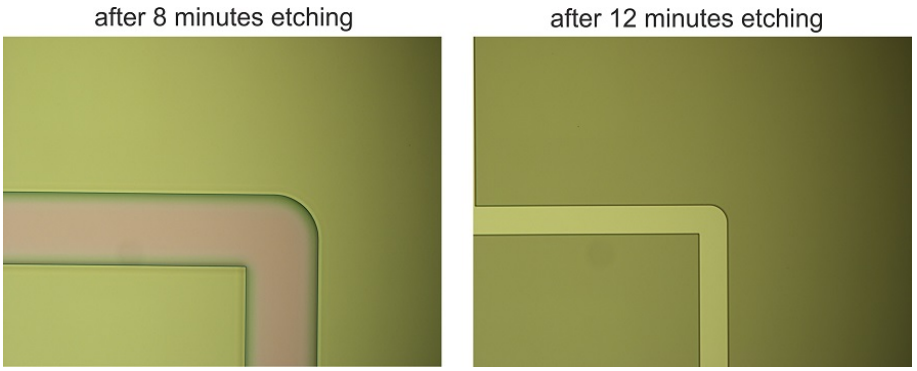

FIGURE 4.20: 40 μm wide trenches during ICP etching of oxide mask for SOI handle layer

of a polymer passivation layer created with C_4F_8 gas. Then, an anisotropic plasma etch is performed that removes all polymer that is exposed vertically, leaving behind a protective layer on the sidewalls of the features. Finally, the exposed silicon at the bottom of the feature is etched with an isotropic SF_6 plasma etch. The process then repeats, with each cycle taking 10 seconds.

The development of the DRIE recipes and etch times needed to achieve successful results will be detailed in this section. In order to characterise etch rates and side wall angles, DRIE has been performed on plain Si test wafers that have been patterned with front or back side oxide masks. After DRIE has been performed, the wafer is cleaved, to allow for profile images to be taken with a scanning electron microscope (SEM).

The critical dimension for the front side features is 5 μm for the trenches that define the beams and resonator structures. All other features, such as release holes and bonding pad boundary trenches, are larger than 5 μm. First, the etch rate has been characterised using Si test wafers. Fig. 4.21 shows the cross section of a 5 μm trench after 10 minutes of etching. The sidewall angle is acceptable and the average etch rate is determined to be 6.7 μm/min. For etching the 50 μm device layer of an SOI wafer, about 8 minutes should be sufficient.

Fig. 4.22 shows the cross section of some release holes and a 25 μm trench. It can be seen that the wider feature etches faster than the narrower release holes. On an SOI wafer, the wider trench would etch down to the BOX first and may begin etching the sides at the bottom of the trench, an effect called "notching". However, the 25 μm trench is wide enough that notching should not be a problem [14]. In addition, the 25 μm trench is not a critical device feature as it is the boundary of the entire device.

As with the device layer, the DRIE of the handle layer is first tested on a Si wafer that has been patterned with a handle layer oxide mask. A 75 minute etch has been performed with the low-frequency bias of the polymer etch being ramped up from 350 V at the start to 450 V after 75 minutes. The modification of the bias is necessary to maintain

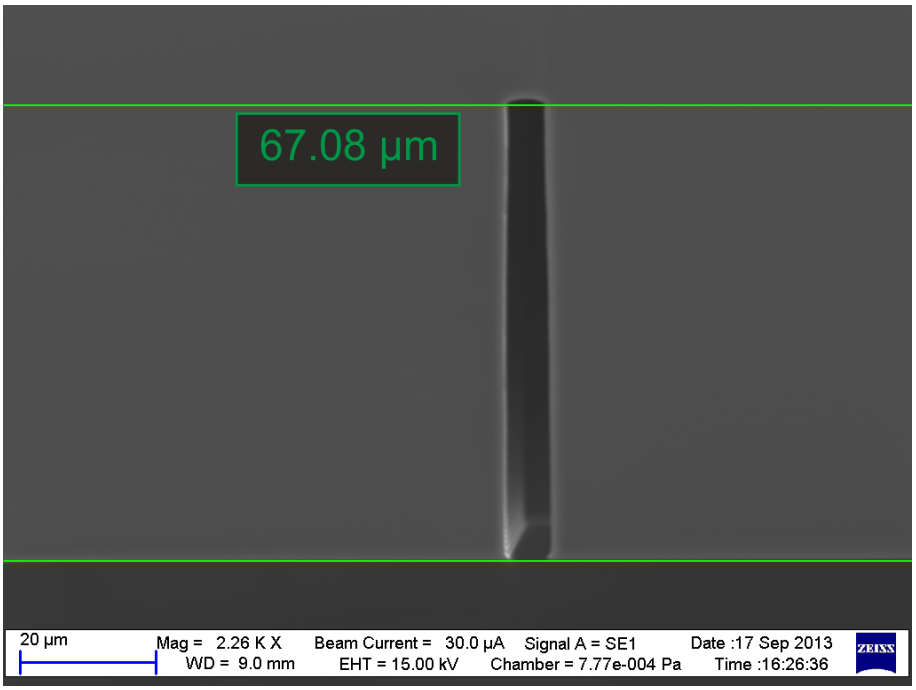

FIGURE 4.21: DRIE etching of Si test wafer with device layer oxide mask

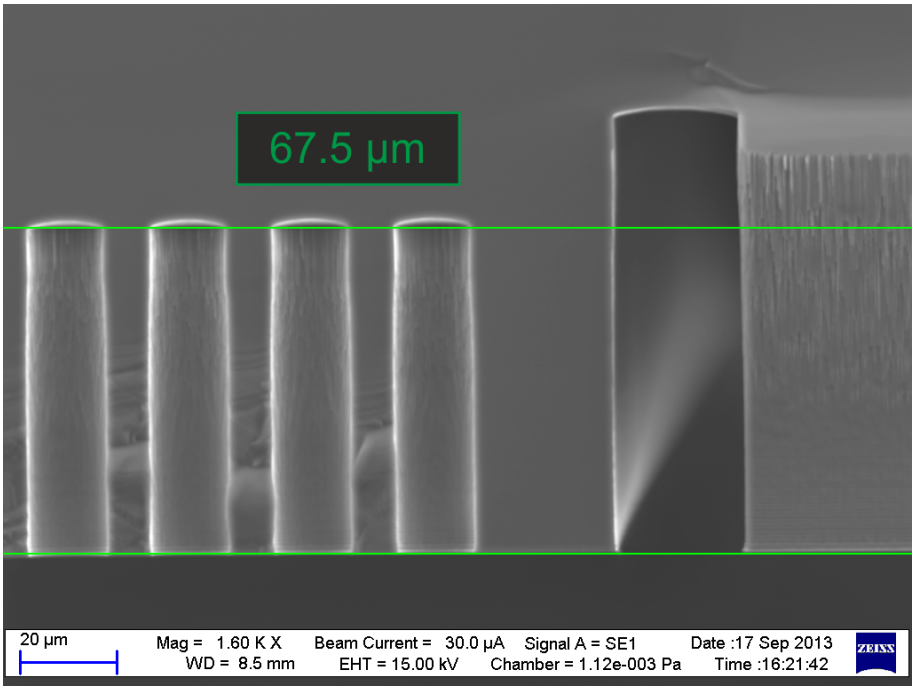

FIGURE 4.22: DRIE etching of Si test wafer, showing release holes and device boundary trench

a vertical side wall and stop the trench from tapering at the bottom. A cross section of a 40 μm wide trench is shown in Fig. 4.23. The etch depth is 443 μm, indicating an average etch rate of 5.9 μm/min. Therefore, to etch through the 560 μm handle layer of an SOI wafer will require at least 95 minutes of etching with the bias continuing to

ramp up beyond 450 V.

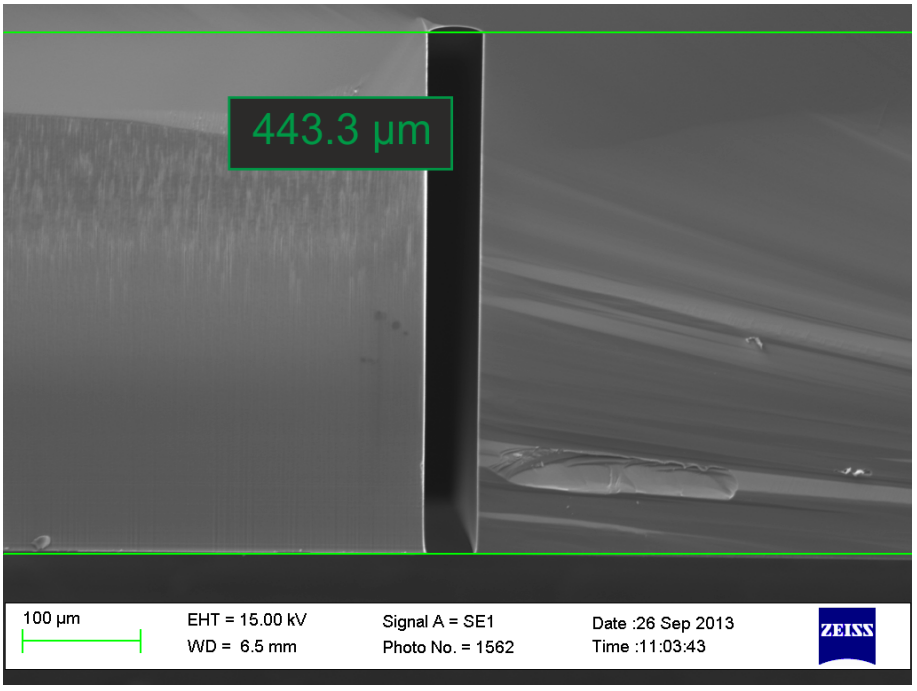

FIGURE 4.23: DRIE etching of Si test wafer with handle layer mask. Image shows cross section of 40 μm trench after 75 minutes of etching.

After running the front and back DRIE on Si test wafers, an SOI wafer has been etched from the front and the back. However, it has been found that the behaviour of the DRIE is very different for an SOI wafer, compared to a plain Si wafer. The BOX layer of the SOI wafer acts as an insulating layer, both thermally and electrically. For the device layer DRIE, the bias of the polymer etch has had to be increased from 250 V to 450 V, in order to overcome the accumulation of charge at the bottom of the trench as the etch approaches the BOX. For the handle layer DRIE, the same recipe as the test wafer has been used and resulted in the trenches failing to reach the BOX, as shown in Fig. 4.24. The back side etching missed the BOX by 25 μm and no further etching could be performed due to a misalignment of the front and back masks on the first SOI wafer. The front side etching was successful and no notching has been observed with the SEM at any of the features, including the 5 μm trenches. Some tapering has been measured at the 5 μm trenches, with the trenches narrowing by up to 1 μm at the bottom.

The etch rates that have been characterised using the first, unsuccessful SOI wafer, have been utilised for the second SOI wafer. The front etch recipe used a 500 V bias and a time of 9 minutes. A back side etch of 100 minutes has been performed, with the low-frequency bias of the polymer etch being ramped up from 350 V at the start to 500 V after 100 minutes.

After 90 minutes of etching the back side, the etch has been stopped in order to inspect the wafer and verify that the etch had not yet been completed. In the process of

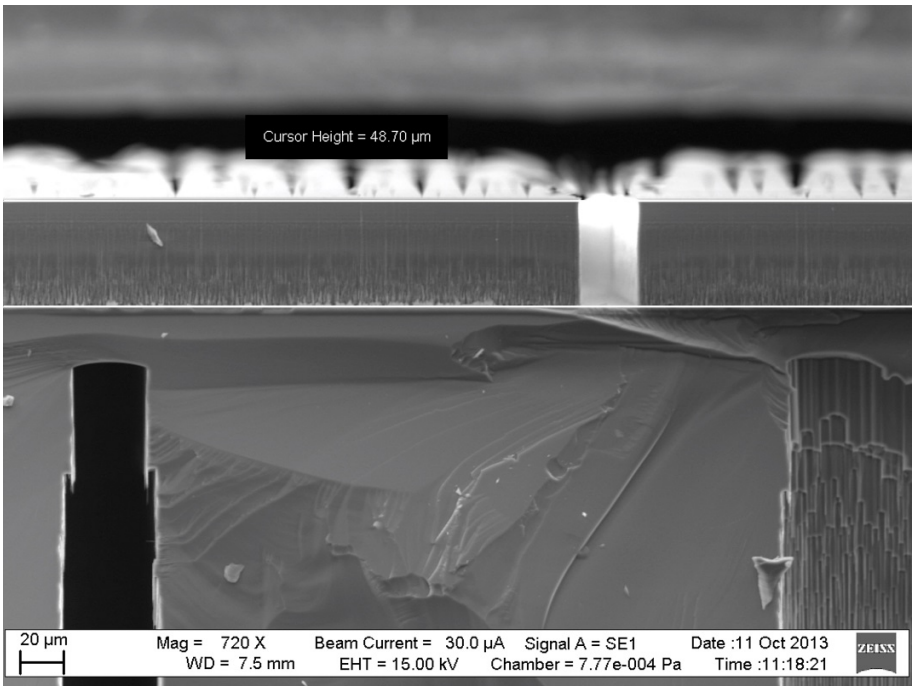

FIGURE 4.24: DRIE etching of SOI wafer. Image shows cross section of front and back side trenches. The device layer thickness has been measured to be 48.7 μm

unloading the wafer from the DRIE chamber, the wafer became stuck to the clamp ring, which holds the rim of the wafer during etching to maintain a seal for the back side helium cooling. The wafer eventually fell off the clamping ring, falling onto the loading pins and breaking into six pieces. The wafer broke along the backside trenches that define the chips. In order to complete the DRIE, the wafer pieces have been bonded to a carrier wafer using AZ9260 photoresist. After the remaining 10 minutes of DRIE has been performed, the wafer pieces have been removed from the carrier wafer using AZ100 resist stripper at 80 °C.

The end result has been a successful through etch of the handle layer, with the front side pattern being visible, with an optical microscope, at the bottom of the back side trenches.

4.5.3 HF vapour etching

The final stage in the fabrication process after DRIE is the release of the resonators and the chips from the wafer grid. The release has been performed using an HF vapour phase etch to remove the oxide below the MEMS structures and around the border of each chip. The etched SOI wafer pieces are fixed to an electrostatic chuck that is heated to 40 °C and is positioned front side down in the HF vapour chamber. The devices all released after 1 hour of exposure to HF vapour. After the etch, the wafer pieces are placed front side up and the wafer grid is lifted (Fig. 4.25b), which leaves behind

the chips. Then each chip is lifted, leaving behind the handle blocks from each device (Fig. 4.25a).

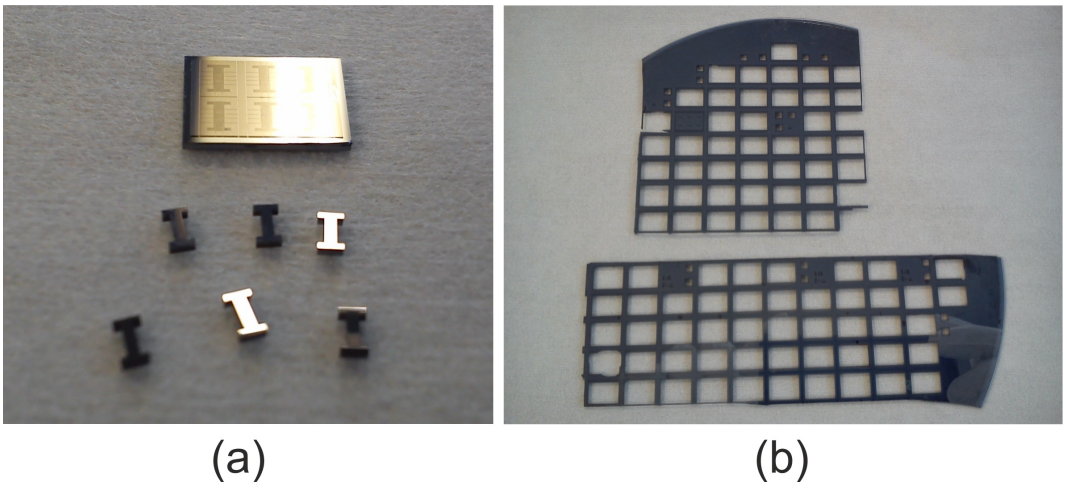

FIGURE 4.25: Coupled resonator fabrication: (a) HF vapour release of handle block (b) wafer grid remaining after release of chips

4.5.4 Finished devices

Fig. 4.26 shows an image of a completed device taken using a scanning electron microscope (SEM). It can be seen that the front side pattern has been successfully transferred to the device layer of the SOI wafer using DRIE. The device shown is of a clampled-clamped beam device with 410 $\times$ 10 μm beams. Additional devices of the dimensions listed in Tab. 4.1 have been fabricated successfully.

Also, the fabrication performed has produced successfully coupled resonator devices of the larger centre area design. An SEM image of one of the fabricated devices is shown in Fig. 4.27. Several devices have been obtained from the 150 mm SOI wafer, including all of the designs listed in Tab. 4.3.

4.6 NPU fabrication process

In addition to the devices fabricated at the University of Southampton, another batch of devices has been designed for fabrication at Northwestern Polytechnical University (NPU), Xi'an, China, using an SOI fabrication process developed there [14].

The process uses an SOI wafer of diameter 100 mm with a handle layer thickness of 400 μm. The wafer has a silicon device layer thickness of 30 μm and a BOX thickness of 5 μm. The fabrication process steps are shown in Fig. 4.28. Beginning with the SOI wafer (a), the MEMS structures are created by patterning and etching the device

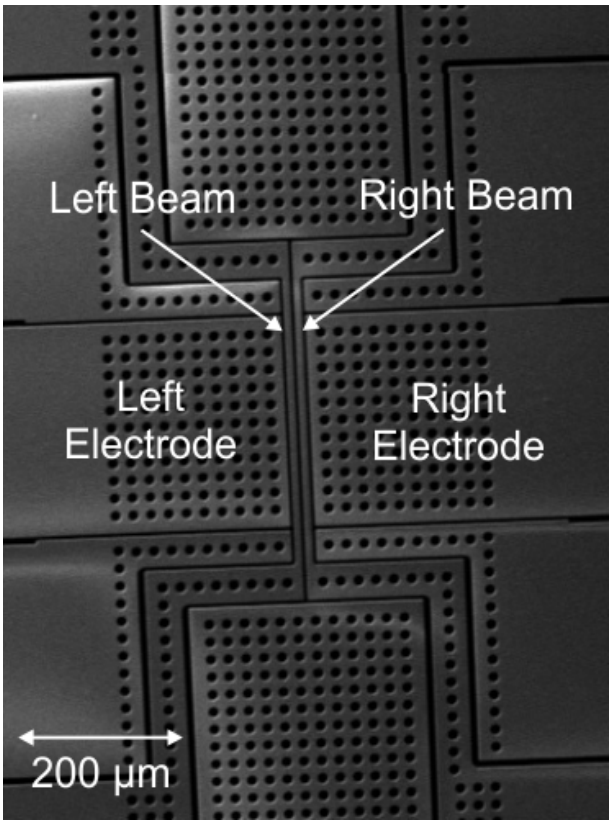

FIGURE 4.26: Scanning electron micrograph of a coupled clamped-clamped beam resonator device with 410 × 10 μm beams.

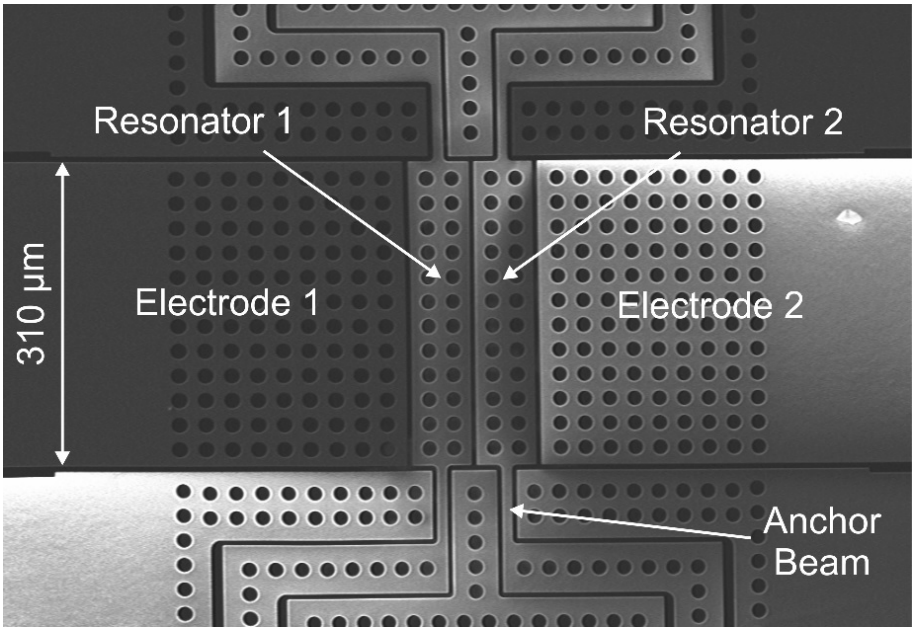

FIGURE 4.27: Scanning electron micrograph of a coupled resonator device with 310 × 60 μm centre area and 55 μm anchor beams.

layer using DRIE. The release hole pattern at the larger structural areas is overetched (b). The overetching causes notching, which results in a rough underside surface for the larger structural areas. The rough surface prevents stiction during the removal of the underlying BOX with a 40 % HF solution (c). Before the BOX removal step, the wafer is partially diced using a dicing saw before shipping from NPU to Southampton. Then, the individual chips are separated through cleaving and the oxide etch is performed. The use of HF vapour for the release of the resonators had been attempted, to reduce further the risk of stiction, but the time taken to remove the oxide was several hours, as the exposed oxide across had to be etched first.

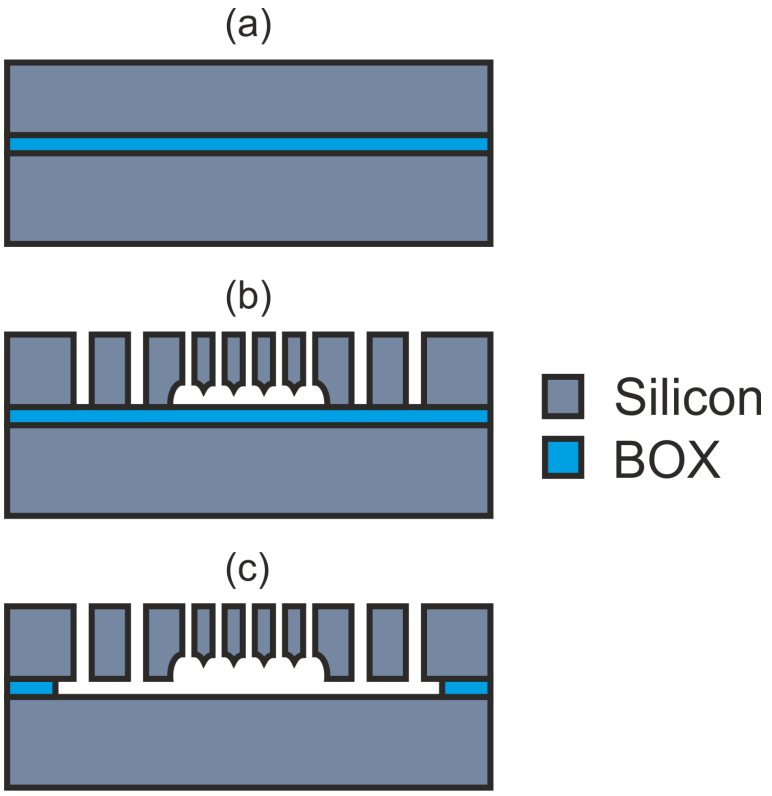

FIGURE 4.28: SOI fabrication process developed at NPU: (a) SOI wafer with 30 μm device layer, 5 μm BOX layer, and 400 μm handle wafer (b) Overetched DRIE of front side trenches and release holes (c) HF solution etch of BOX resulting in release of resonators. Rough underside caused by DRIE overetch ensures no stiction.

4.7 Design of devices using the NPU fabrication process

For the implementation of MEMS mode-localisation based sensors using the NPU fabrication process, a further variation on the device architectures has been designed. The layout of the coupled MEMS resonators using the NPU fabrication is achieved through the design of the single photomask. The photomask is used to pattern the photoresist layer that creates a mask layer for the DRIE. As before, the design is carried out using Tanner Tools L-Edit.

A new design have been created, which has some features not seen with the devices designed for the Southampton fabrication process. A 3D representation of the folded-beam anchor design is shown in Fig. 4.29. The layout design view is shown in Fig. 4.30. The device consists of two rectangular masses positioned parallel to each other, separated by a coupling gap of 3 μm. Alongside each resonator mass, a fixed electrode is positioned with a resonator-to-electrode spacing of 3 μm. Each mass is connected to each of the two fixed anchors with a pair of folded-beams.

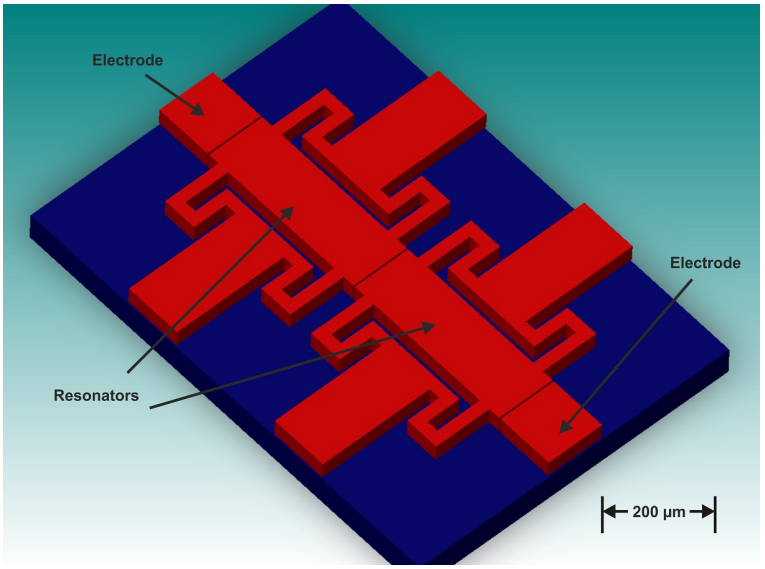

FIGURE 4.29: 3D representation of a folded anchor beam device (red: device layer, blue: handle layer

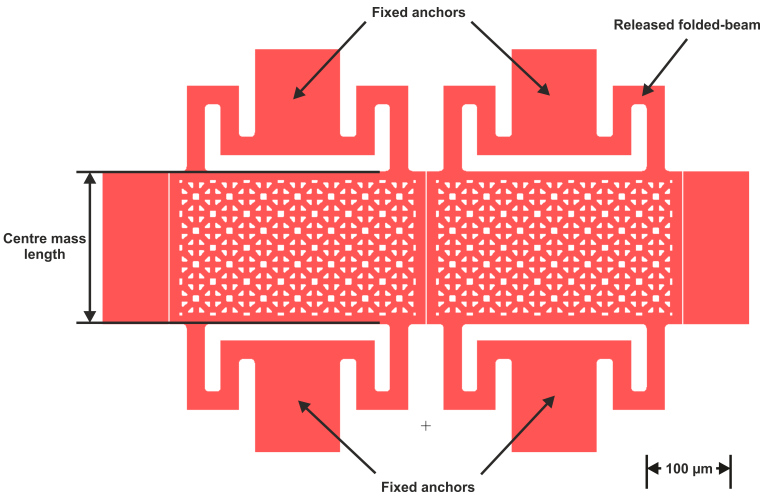

FIGURE 4.30: Photolithography mask layout for coupled resonators with a folded-beam anchor design.

The folded-beam anchors result in a lower stiffness compared to a simple anchor beam, as a result of the longer effective length, due to the folded design. The mechanical stiffness of one of the resonators can be calculated using (4.11), where L_a is the total length of

one of the four folded anchor beams. The width of the centre mass of the resonators has been held at 300 μm, so as to allow for a large enough fixed anchor (100 μm) that obeys the design rules. Two different centre mass lengths have been considered, 100 μm and 180 μm. The anchor beam length will influence the mechanical stiffness of the resonators and, therefore, the minimum required ΔV necessary to maintain adequate separation of the two modal frequencies, as shown in the graph of Fig. 4.31. As explained previously, the upper practical limit for ΔV is 120 V. It can be seen from Fig. 4.31 that, for devices with a 3 μm coupling gap, all anchor beam lengths down to 100 μm should be practical, for both centre mass lengths.

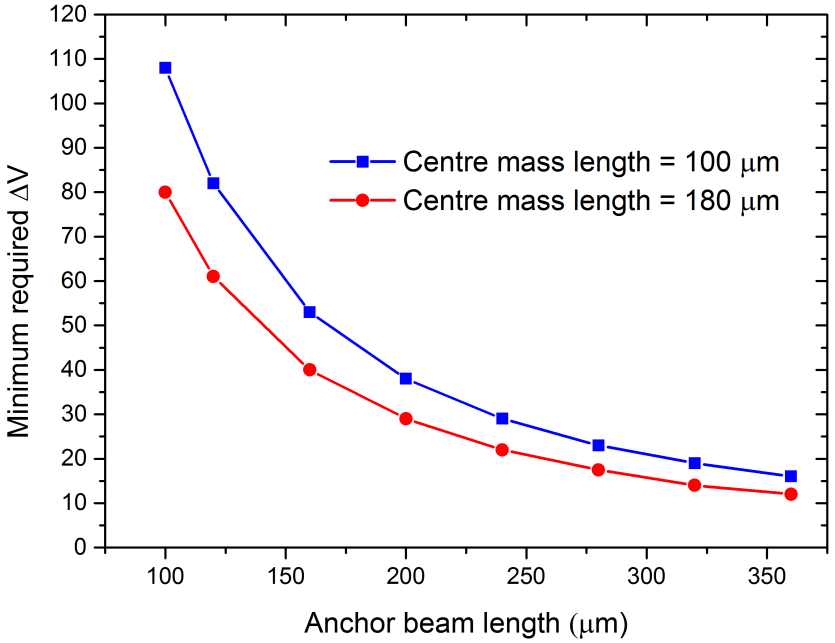

FIGURE 4.31: Minimum ΔV required to maintain adequate separation of two mode peaks for different folded anchor beam lengths.

The first design has a centre mass with dimensions 300 μm $\times$ 180 μm and a folded anchor beam length of 120 μm, which should give the highest sensitivity within the limit that have been specified. An additional design has been included with a centre mass length of 100 μm and a folded anchor beam length of 240 μm, bringing the minimum ΔV down to 29 V.

Device	Trench Width (μm)	Centre Mass Length (μm)	Folded Anchor Beam Length (μm)
1	3	180	120
2	3	100	240

TABLE 4.5: List of devices for folded-beam anchor design using NPU fabrication process.

Fig. 4.32 shows the complete layout of a coupled resonator device of the folded-beam anchor design. Bonding pads of dimensions 500 μm $\times$ 500 μm have been designed to

allow for wire bonding of the device, so that it can be connected to surrounding circuitry necessary for actuation and sensing.

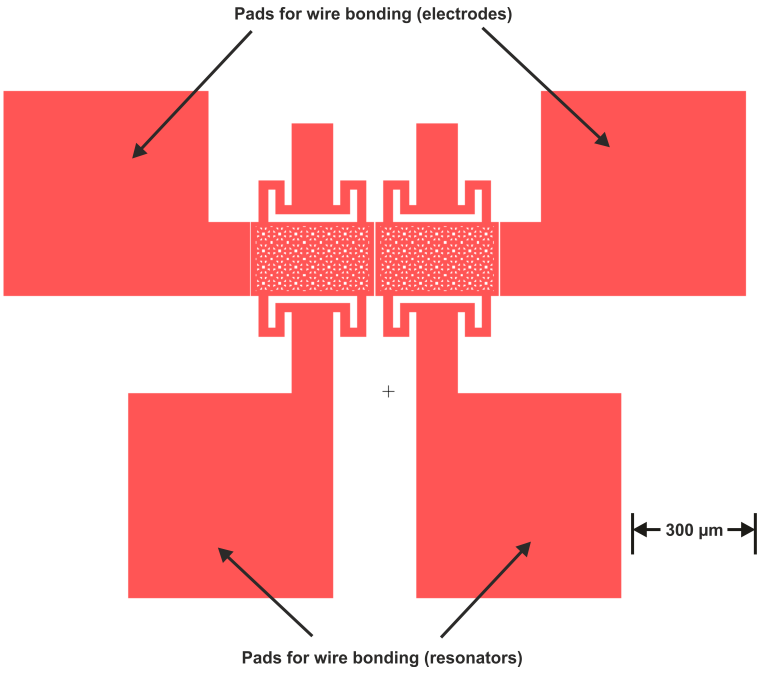

FIGURE 4.32: Photolithography mask layout for coupled resonators with a folded-beam anchor design, including pads for wire bonding

4.8 Theoretical amplitude ratio response to perturbation for NPU devices

Fig. 4.33 shows the theoretically calculated response of the out-of-phase amplitude ratio to a relative increase in stiffness of resonator 1, for the designs of device 1 and 2 from Tab. 4.5. It can been seen that the design of device 1 exhibits a greater sensitivity, owing to its mechanical stiffness of 97997 N/m, greater than the 12250 N/m value of device 2.

As with the devices that have designed with the Southampton fabrication process, the theory will be compared to the experimental results of fabricated device characterisation, covered in the later chapters of this thesis.

4.9 Fabrication of devices using the NPU process

As explained previously, the devices that have been designed for the NPU fabrication process have been mostly fabricated at NPU, with only the final separation of the individual chips from each other and the release of the MEMS structures using HF solution

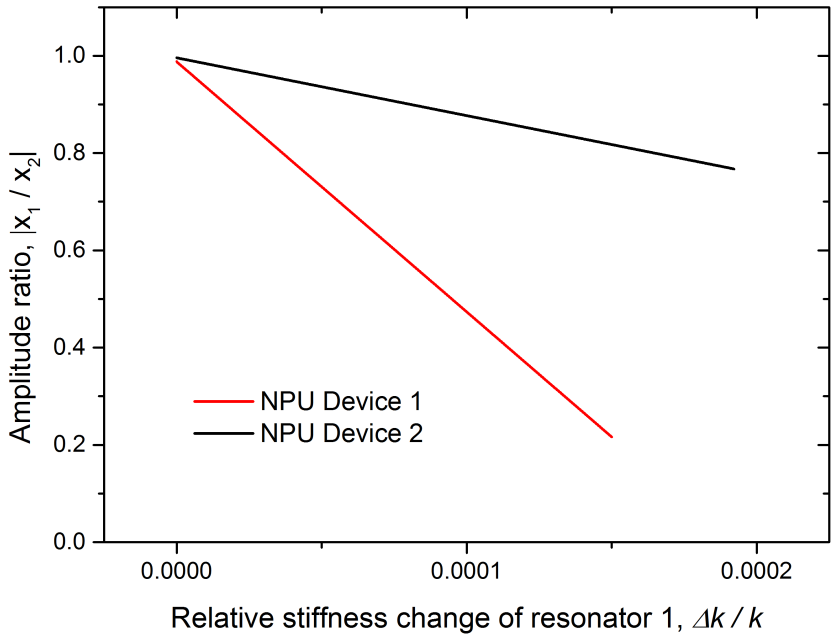

FIGURE 4.33: Theoretical response of out-of-phase amplitude ratio to a relative stiffness change on resonator 1 for two different device designs of the NPU fabrication process.

to remove the underlying BOX being performed in Southampton. An SEM image of a fabricated device is shown in Fig. 4.34.

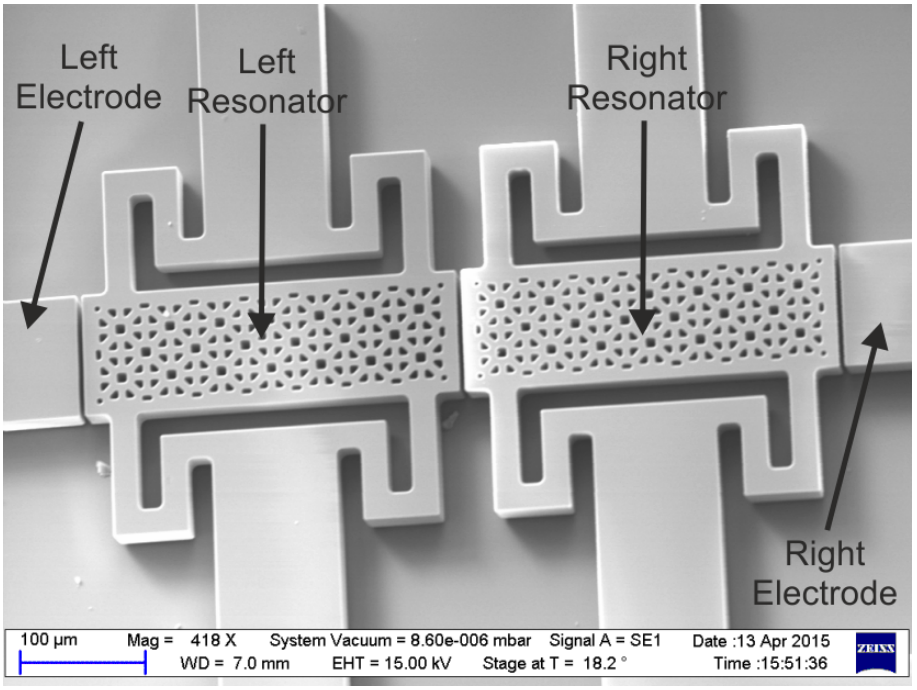

FIGURE 4.34: Scanning electron micrograph of a coupled resonator device fabricated using the NPU process.

The main difference to notice between the NPU devices and the devices fabricated in

Southampton is that there is no removal of the handle wafer below the resonators. Consequently, the yield for the devices fabricated using the NPU process is significantly lower (less than 20 %), when compared to the Southampton fabrication process (95 % for the devices in this work).

4.10 Summary

In this chapter, the design of the devices for use in this thesis has been detailed. Two fabrication processes have been used to produce coupled-resonator devices, one used at the University of Southampton and the other used at Northwestern Polytechnical University (NPU), Xi'an, China.

Each process uses an SOI wafer as its starting material with the buried oxide serving as the sacrificial layer. The device dimensions have been justified in terms of the design rules of the two fabrication processes and the limitations of the experimental set-up that is to be used to characterise the devices.

The theoretical mode-localisation behaviour of the device designs has been calculated and will be compared to FEM simulations and experimental results in the later chapters of this thesis.

A 150 mm SOI wafer has been processed to fabricate a batch of coupled MEMS resonator devices. The successful fabrication has been made possible by all of the process information generated by test Si wafers and unsuccessful SOI wafers.

Now that the fabrication process has been fully characterised, in ideal conditions, with available and properly functioning equipment, it is theoretically possible to complete the fabrication of a batch of devices from one SOI wafer in five working days.

Chapter 5

Finite-element simulations of coupled resonator systems

5.1 Introduction

In this chapter, finite-element method (FEM) simulations have been performed with *CoventorWare*, a MEMS simulation software package. The effect of stiffness perturbation on the mode shapes of electrostatically coupled resonator pairs has been simulated.

Three-dimensional meshed models have been created of the designs that have been outlined in chapter 4. Atmospheric damping and anchor losses have been included in the models, which include the resonators and the neighbouring electrodes, allowing for the simulation of an electrostatically induced stiffness change of one resonator.

The results of the simulations have been compared to the theory and in the later chapters of this thesis, the experimental results will be compared to the FEM simulation results in order to verify them.

5.2 CoventorWare and the finite element method

CoventorWare is a software package that allows for the creation of 3D models of microstructures and for their behaviour in response to various stimuli to be analysed.

First, the materials that the model is to be composed of are chosen and their properties are defined. These properties include density, Young's modulus and electrical conductivity. Then, a fabrication process is defined in the process editor. The material and the thickness of each of the layers of the model are defined. Then, the layout editor module is used to define the shape and dimensions of each layer, in much the same way as designing a photolithography mask, as shown in Fig. 5.1.

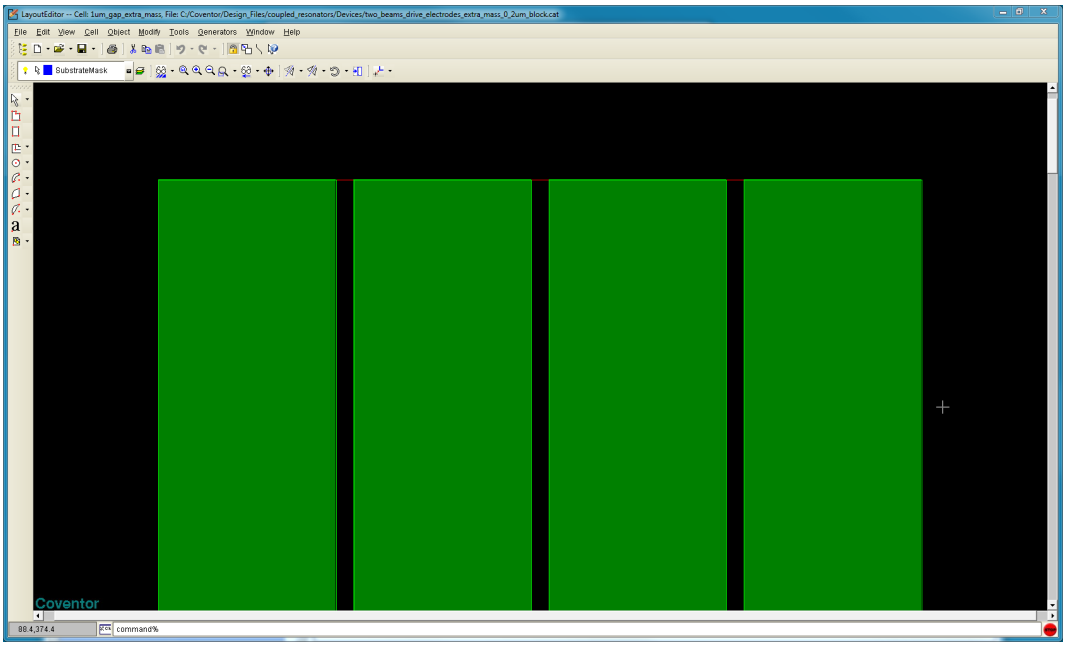

FIGURE 5.1: CoventorWare layout editor

Next, the information in the process and layout files are combined by the preprocessor module to create a 3D model of the structure, as shown in Fig. 5.2. Before simulations can be performed on this model, all the faces of the 3D structure need to be named, to enable the various boundary conditions to be set and to allow forces or voltages to be applied. The final step to be performed before simulation is to create a mesh for the FEM analysis.

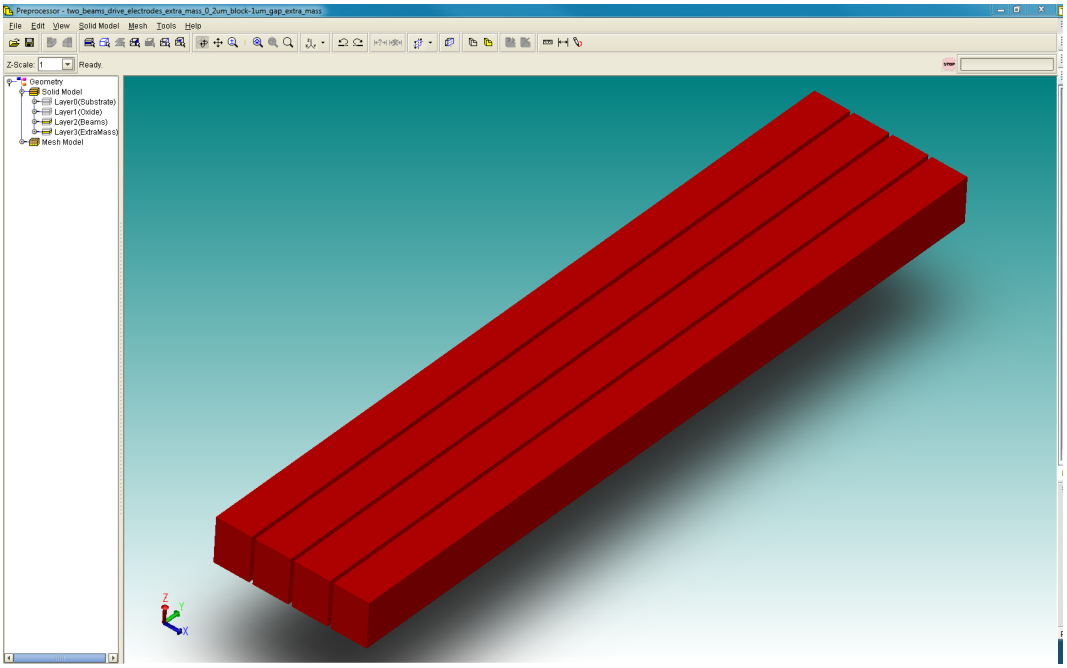

FIGURE 5.2: CoventorWare 3D model created from process and layout design files

The finite element method involves breaking down a 3D model into small discrete ele-

ments. The vertices of these elements are called nodes. The shape and density of the elements are defined, using the preprocessor, to create a mesh. The end result is shown in Fig. 5.3. FEM simulations are performed using the meshed model. For all the simulations, a mesh density has been selected that ensured a reasonable simulation time without sacrificing the accuracy of the results. The values used have been converged on after running several test simulations. For the simulations reported in this chapter, the mechanical solver, MemMech, is used. MemMech is used to calculate the displacement and stress throughout a structure that is subject to an external force. This is achieved by calculating the displacement of each of the nodes and the stress along each vertex connected to them [102].

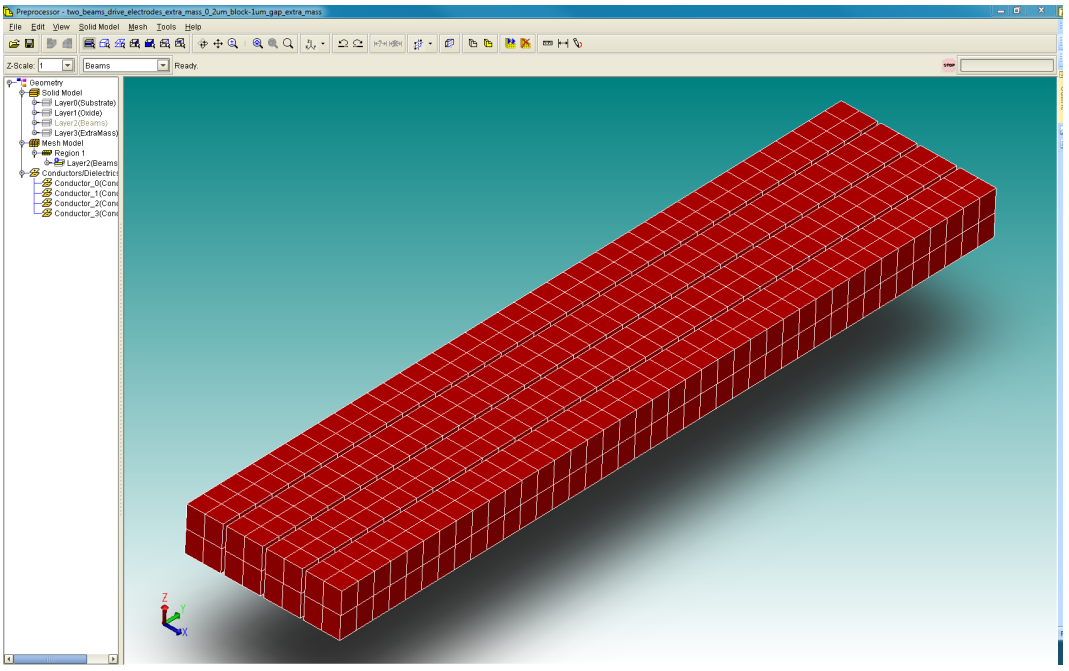

FIGURE 5.3: CoventorWare 3D model meshed for FEM simulation

When setting up the simulation in MemMech, the boundary conditions must be defined. Faces of the model that will be fixed are nominated as well as the faces that any external force will be applied to. The applied force can take the form of a mechanical or an electrostatic force. For a mechanical force, the pressure to be applied to a particular face is simply defined in N/m^2. If an electrostatic force is desired, then voltages on different faces can be defined, which will result in attractive force between structures.

In order to determine the mode frequencies and mode shapes of a 3D model, MemMech is used to perform a modal simulation. For a harmonic analysis, a sinusoidal force, as opposed to a static force, is applied to the model and the frequency is swept through a range of values around the mode frequencies, so that the vibration amplitude of the model across the frequency range can be determined. The results from a harmonic analysis can be used to determine the Q-factor of the model.

5.2.1 Damping

CoventorWare provides the simulation solver DampingMM to allow for the damping of a structure to be computed, which allows for the environmental conditions of the model to be specified and their influence included in the simulation. The atmospheric pressure can be specified, allowing for its effect on the damping of the vibrations to be factored into any modal or harmonic analyses. Also, the vibration energy that is lost through the anchors of a resonator structure is included in the simulation by allowing the faces at the edge of the model to absorb some of the vibration energy, rather than reflect all of it.

DampingMM calculates the squeezed film damping that results from the air in the gaps between the resonators and between the resonators and the electrodes [102]. The solver utilises a flow resistance model, which represents a linearised Reynold's equation with a finite-element model. The solver assumes a small gap relative to the area of the resonator, which is the case for the devices designed in this thesis. Another aspect of the DampingMM simulation is the flow resistance that is added from the atmosphere flowing round a corner to flow out an edge. As the linearised Reynold's equation is not valid at the edge region, the solver uses a flow models that have been developed from the Navier-Stokes equation [102].

In addition to the viscous damping, the DampingMM solver also models spring effects that occur due to the compression of the atmosphere in the gaps between the resonators and between the resonators and the electrodes.

The calculated mode shape produced by the modal simulation in MemMech is loaded into the DampingMM solver and the atmospheric pressure and temperature is set. Then, the faces on either side of the gap between the resonators are specified in the boundary conditions so that they will interact with the air. The faces on either side of the gap between the beams and the electrodes are specified similarly. The DampingMM solver produces a damping coefficient, which has units of newton-seconds per metre (Nsm^{-1}), describing the ratio of the damping force to the amplitude of the velocity of the resonator. The damping coefficient values for the out-of-phase and in-phase modes are retained for use with the MemMech solver, which will calculate the impact of the damping on the vibration amplitudes of the beams at the modal frequencies.

The anchor losses are computed during the harmonic analysis performed by the MemMech solver. The outer edges of the model are not fixed rigidly. Instead they are specified in the solver as being a 'quiet boundary', which prevents the reflection of all the vibration energy back into the resonating structure, simulating the effect of energy loss to the surrounding environment.

All of the FEM simulations that have been performed for this chapter include the effects of atmospheric damping and losses at the anchors. For the devices in this thesis, it

is possible to utilise the damping simulation capabilities of *CoventorWare* due to the simple geometry of the resonators, with parallel plates being the surfaces to calculate squeezed-film effects for. More complicated structural architectures are beyond the capability of the software [102], but that is not a limitation for the simulation work in this thesis.

5.3 Simple beams design

5.3.1 Simulation model set up

The first FEM simulations have been performed on a model of the rectangular clamped-clamped beams design described in chapter 4. 3D models have been created with the dimensions of devices 1 and 2 in Tab. 4.1. In addition to the resonator structures themselves, the surrounding area of the device layer has been included in the model to allow energy loss at the anchors, where vibration energy is dissipated into the surrounding material.

The models has been meshed with a rectangular brick mesh with each brick measuring 20 μm in each direction, which provided the fastest computation time without sacrificing result accuracy. The 3D meshed model of the device with 10 μm wide beams is shown in Fig. 5.4. A representation of the back side of the 3D model has been shown previously in Fig. 4.4, showing the cavity left behind by the removal of the handle layer block below the resonators.

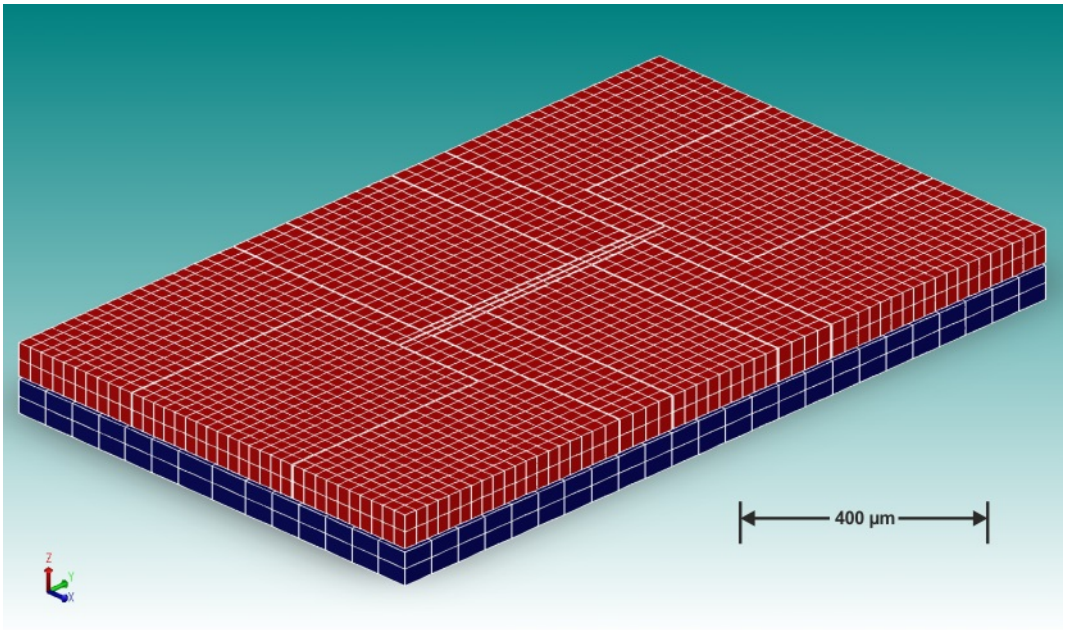

FIGURE 5.4: CoventorWare 3D meshed model of two beams coupled-resonator device with 410 × 10 μm beams.

The purpose of the FEM simulation is to determine the vibration amplitudes of the beams at the out-of-phase and in-phase mode shapes. In order to obtain accurate values for the amplitudes, anchor losses and the damping caused by the surrounding atmosphere must be factored into the simulation. *CoventorWare* has the capability to include these losses in an FEM simulation, using the MemMech and DampingMM solvers.

In order to calculate the damping of the coupled resonator system, MemMech is used first to obtain the in-phase and out-of-phase mode shapes. The numbering scheme of the beams and the electrodes is showm in Fig. 5.5. The beams have been electrostatically coupled together by applying DC voltages of 0 V and -120 V to resonator 1 and resonator 2, respectively, resulting in a coupling spring, k_c, that can be calculated as follows

$$\begin{aligned} k_c &= -\frac{(\Delta V)^2 \varepsilon_0 A}{g^3} \\ &= -\frac{(120\ \text{V})^2 \times 8.85 \times 10^{-12} \times 410\ \mu\text{m} \times 50\ \mu\text{m}}{(5\ \mu\text{m})^3} \\ &= -20.9\ \text{N/m} \end{aligned} \tag{5.1}$$

Another simulation using a different coupling spring has been performed. A value of -80 V has been applied to resonator 2, which will result in a weaker coupling spring, which has been calculated as follows

$$\begin{aligned} k_c &= -\frac{(\Delta V)^2 \varepsilon_0 A}{g^3} \\ &= -\frac{(90\ \text{V})^2 \times 8.85 \times 10^{-12} \times 410\ \mu\text{m} \times 50\ \mu\text{m}}{(5\ \mu\text{m})^3} \\ &= -11.75\ \text{N/m} \end{aligned} \tag{5.2}$$

In addition to the DC voltages applied to the two beams to create the two values of coupling spring, the two electrodes have also been DC biased to ensure a balanced initial state. Electrode 1 has been set to 120 V or 80 V and electrode 2 has been set to 0 V so that the potential difference between each resonator and its neighbouring electrode is 120 V or 80 V, resulting in equal magnitudes of spring softening (-20.9 N/m or 11.75 N/m) being applied.

The bottom of the handle layer has been fixed and a 1 V peak-to-peak AC voltage has been applied to electrode 1. The out-of-phase mode frequency has been simulated as 455 kHz and the in-phase mode frequency as 458 kHz. Then, the modal analysis determined the normalised mode shapes of the coupled resonator system. The mode shape data is used by the DampingMM solver to calculate the damping. The pressure is

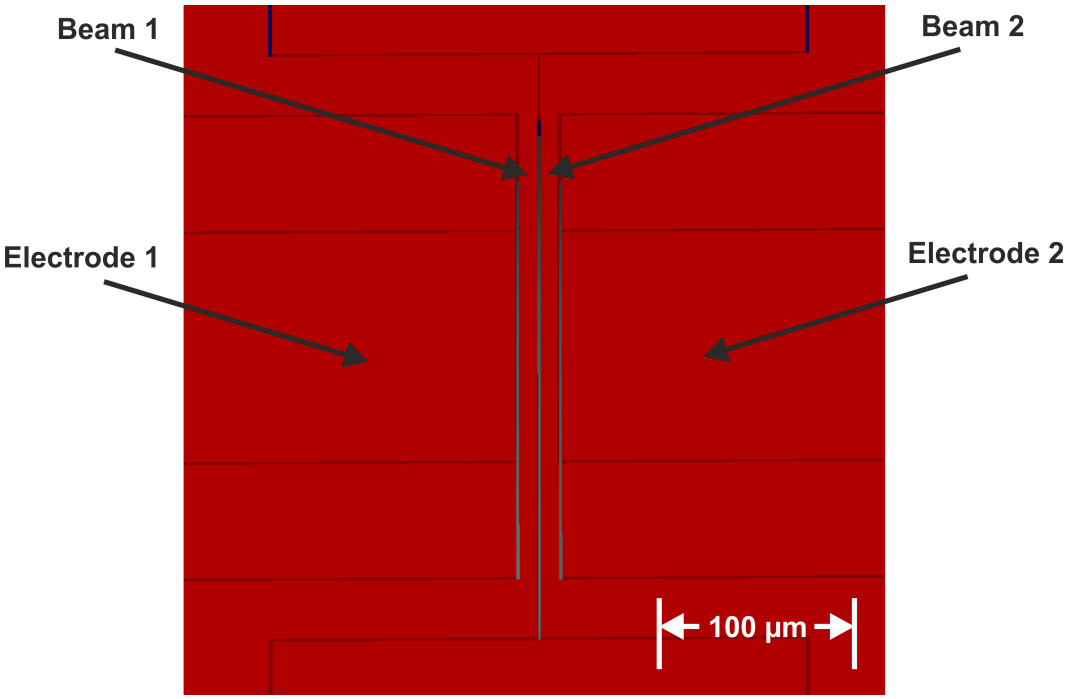

FIGURE 5.5: Close-up view of front side of two-beam coupled resonator system, including substrate and anchors

set to 6.6 Pa, a pressure that is available in a vacuum chamber, and the temperature is set to 300 K. Then, the faces on either side of the gap between the beams are specified in the boundary conditions so that they will interact with the air. The faces on either side of the gap between the beams and the electrodes are specified similarly.

The resulting damping coefficient values for the out-of-phase and in-phase modes are used with the MemMech solver, which will calculate the impact of the damping on the vibration amplitudes of the beams at the modal frequencies. The anchor losses are computed during the harmonic analysis performed by the MemMech solver. For the simulation performed with the model of Fig. 5.4, all of the faces around the edge of the model, including the underside, have been set as a quiet boundary, in order to simulate the effect of energy loss to the surrounding environment.

5.3.2 FEM simulated amplitude ratio response to a stiffness perturbation

The response of the amplitude ratio at the in-phase mode frequency to a stiffness increase of resonator 1 has been simulated using the two beam model shown in Fig. 5.4. The stiffness of resonator 1 has been increased by decreasing the DC voltage of electrode 1, resulting in a decrease of the electrostatic spring softening. For each incremental increase in the stiffness of resonator 1, the amplitude ratio at the in-phase mode frequency has been extracted, allowing the change of amplitude ratio, $\Delta(x_1/x_2)$, as a function of the

relative stiffness increase, $\Delta k/k$, to be determined.

The simulated amplitude ratio response to a relative stiffness increase of resonator 1 has been plotted in Fig. 5.6 for a pair of 410 × 10 μm clamped-clamped beams for k_c = -20.9 N/m and k_c = -11.75 N/m. The graph shows the influence of the strength of the coupling, k_c, on the amplitude ratio response to a stiffness perturbation, confirming the theory that a weaker coupling will result in greater sensitivity. Good agreement between the theory and the FEM simulated results has been achieved, with the FEM simulations showing a slightly higher sensitivity compared to the theory.

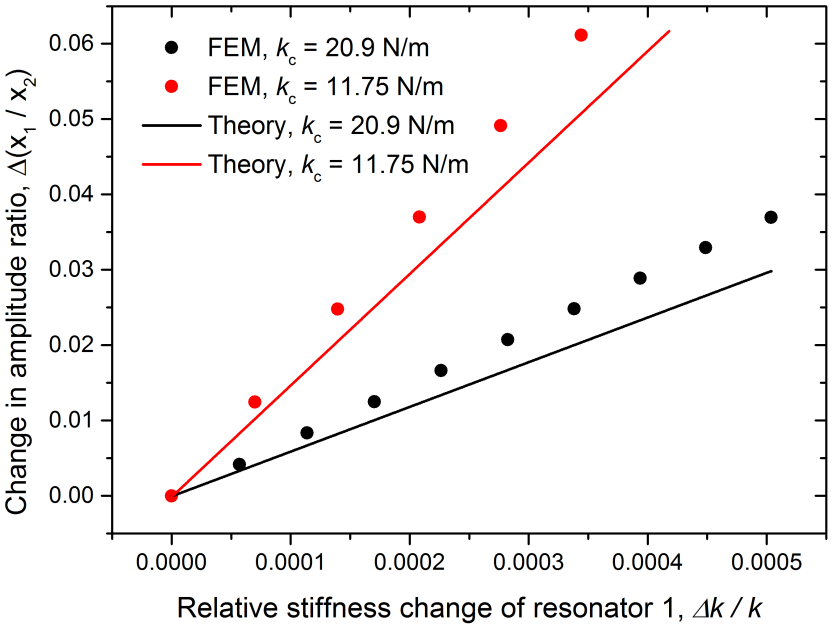

FIGURE 5.6: Theoretical and FEM simulated response of in-phase amplitude ratio to stiffness perturbation for coupled resonator device with 410 × 10 μm beams. Results are shown for two different strengths of coupling spring, k_c

5.3.3 FEM simulations of devices with different beam widths

In addition to the influence of coupling spring stiffness on the amplitude ratio response, the influence of beam width has been simulated. In addition to the model of Fig. 5.4, which has 410 × 10 μm beams, a model with 410 × 20 μm beams has been simulated. The results from the two models are shown in Fig. 5.7 and Fig. 5.8 for beam widths of 10 μm and 20 μm, respectively, for k_c = -20.9 N/m.

As expected from the theory, it can be seen that the sensitivity of the device with 20 μm beams is greater than for the device with 10 μm wide beams. The graphs show agreement between the theory and the FEM simulated responses. In the case of the 20 μm wide beams device, the simulated in-phase mode frequency is 959.616 kHz, compared to the theoretical frequency of 1042.639 kHz. The simulated value includes anchor loss and atmospheric damping.

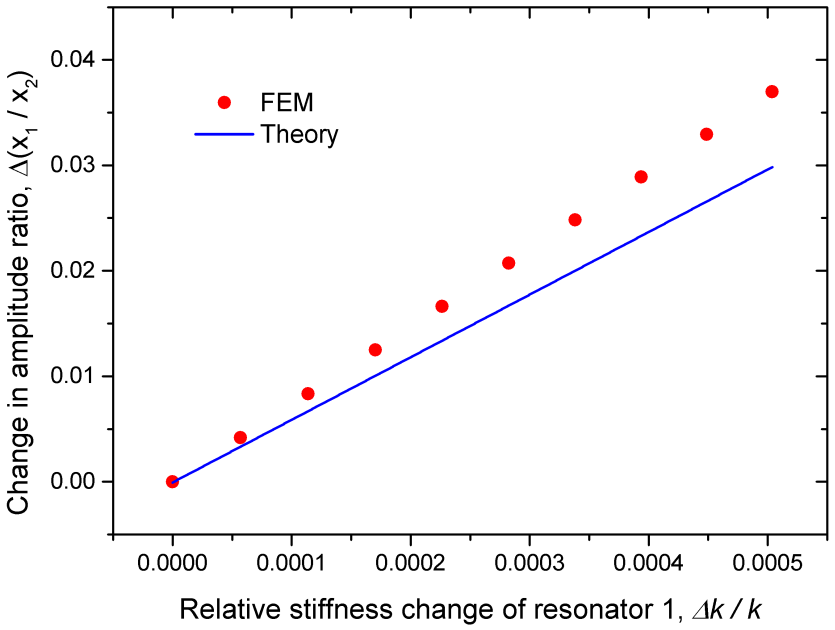

FIGURE 5.7: Theoretical and FEM simulated response of in-phase amplitude ratio to stiffness perturbation for coupled resonator device with 410 × 10 μm beams. k_c = -20.9 N/m

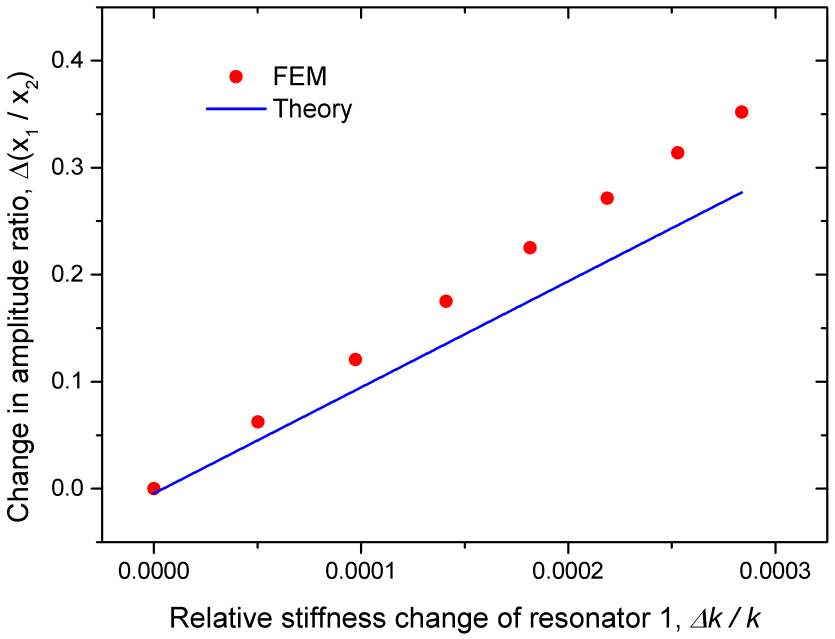

FIGURE 5.8: Theoretical and FEM simulated response of in-phase amplitude ratio to stiffness perturbation for coupled resonator device with 410 × 20 μm beams. k_c = -20.9 N/m

5.3.4 FEM simulations of devices with different beam lengths

The next set of FEM simulations determined the amplitude ratio response to stiffness perturbation for coupled clamped-clamped beam of different lengths. In addition to

the device of dimensions 410 × 10 μm, whose simulated mode-localisation behaviour is shown in Fig. 5.7, two more device models have been created and simulated, with beam lengths of 460 μm and 510 μm (devices 3 and 4 from Tab. 4.1). From Fig. 5.9, it can be seen that plotting the results of the two simulations allows for a comparison of the amplitude ratio response for devices with different beam lengths.

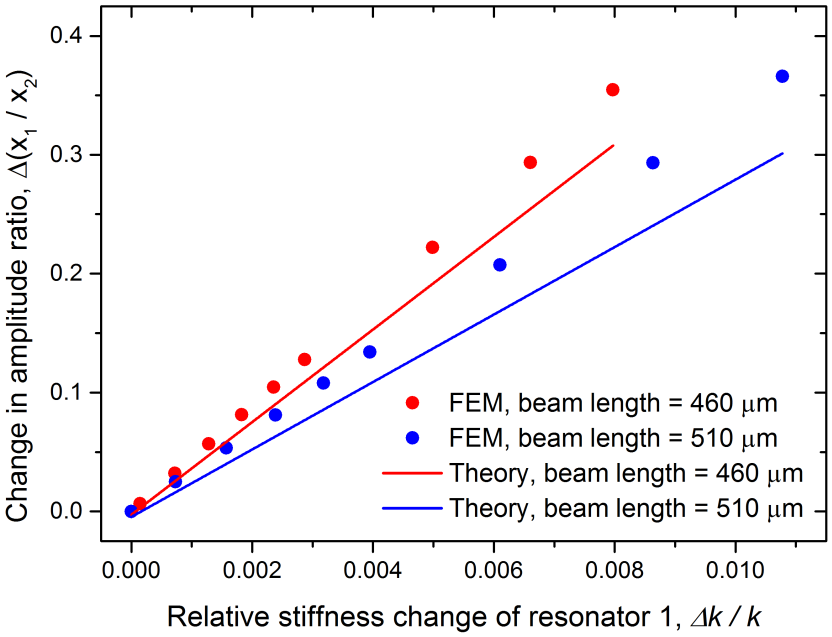

FIGURE 5.9: Theoretical and FEM simulated response of in-phase amplitude ratio to stiffness perturbation for coupled resonator devices with 460 × 10 μm beams and 510 × 10 μm beams.

Again, reasonable agreement is seen between the theory and the FEM simulated results. As before, the FEM simulations have show a higher sensitivity, with the discrepancy attributable to the inclusion of damping and anchor loss in the simulation model. The simulated in-phase mode frequencies are 395.518 kHz and 322.783 kHz for the 460 μm and 510 μm beams, respectively. These values are lower than the previously calculated theoretical frequencies in chapter 4, as a result of the inclusion of damping and anchor loss in the FEM model.

5.4 Larger centre area design

5.4.1 Simulation model

The models of the larger centre area design that have been described in chapter 4 have been created using *CoventorWare*. The dimensions that are listed in Tab. 4.3 have been used to create five different 3D models, which have each been meshed with the same rectangular brick mesh of 20 μm as used with the clamped-clamped beams design,

ensuring an accurate result in a reasonable time. The 3D meshed model of a larger centre area coupled device design is shown in Fig. 5.10, with the surrounding device layer and handle layer hidden for clarity.

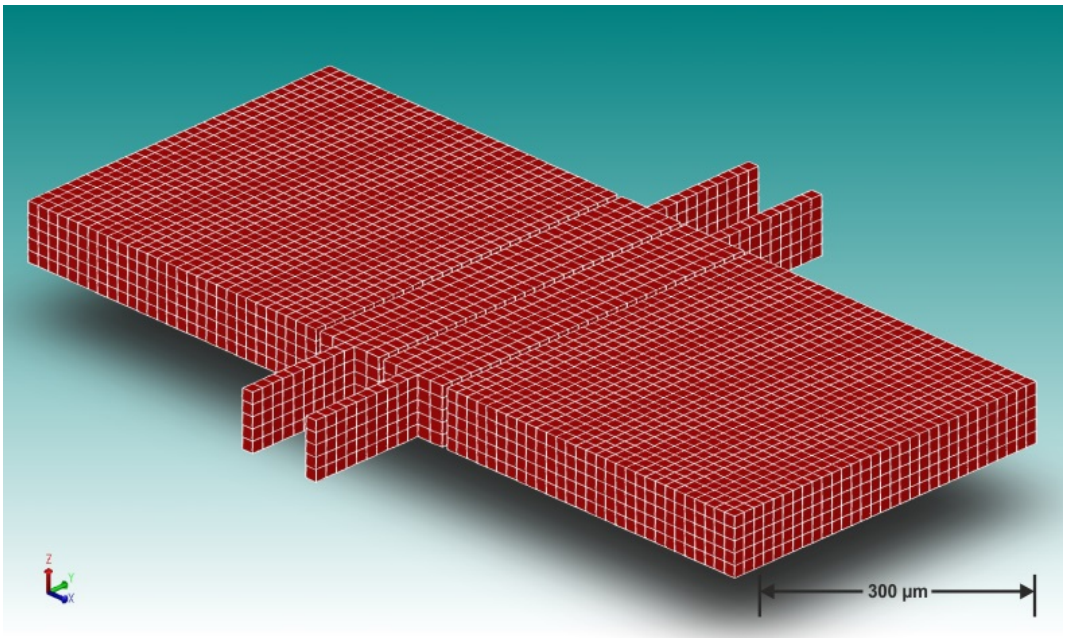

FIGURE 5.10: CoventorWare 3D meshed model of a larger centre area coupled-resonator device with 310 × 60 μm centre blocks and 105 μm anchor beams. The two resonators and the two neighbouring electrodes are shown.

The same anchor losses and atmospheric damping included in the two beams model have been included in the models for the larger centre area design. Electrostatic coupling has been applied to the model by DC biasing the resonators and the electrodes.

5.4.2 FEM simulated amplitude ratio response to a stiffness perturbation

The response of the amplitude ratio at the in-phase mode frequency to a stiffness increase of resonator 1 has been simulated for a meshed model of a coupled resonator device of the larger centre area design. The resonators have centre area dimensions of 310 × 110 μm with 105 μm long anchor beams. The resonators have been electrostatically coupled together by applying DC voltages of 0 V and -120 V to resonator 1 and resonator 2, respectively. The resulting coupling spring, k_c, has been calculated from (5.1) to be 15.8 N/m. Again, to ensure that the coupled system is balanced, the DC voltage of electrode 1 has been set to 120 V and electrode 2 has been set to 0 V, so that equal magnitudes of electrostatic spring softening are applied to each resonator. A second set of simulations have been performed with a DC voltage of -90 V, resulting in weaker electrostatic coupling, k_c, of 8.88 N/m.

The stiffness of resonator 1 has been increased by decreasing the DC voltage of electrode

1, which reduces the electrostatic spring softening. The amplitude ratio at the in-phase mode frequency has been extracted for each increase in stiffness and the response has been plotted as shown in Fig. 5.11.

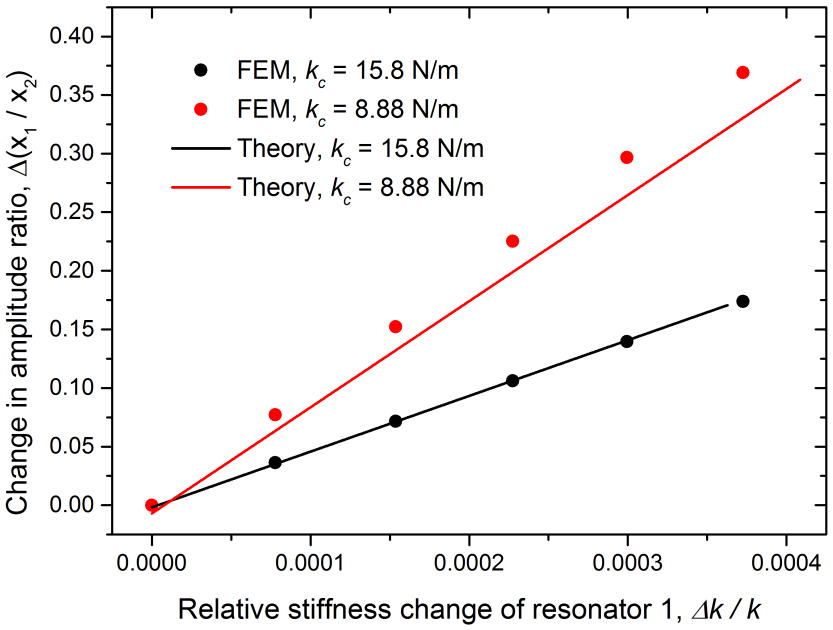

FIGURE 5.11: Theoretical and FEM simulated response of in-phase amplitude ratio to stiffness perturbation for coupled resonator device of the larger centre area design. Centre area dimensions of 310 × 110 μm with 105 μm long anchor beams. Results are shown for two different strengths of coupling spring, k_c.

As with the two clamped-clamped beams model, the FEM simulations for the larger centre area model show the same trend of increased sensitivity to stiffness perturbation for a weaker coupling, showing agreement with theory.

5.4.3 FEM simulations of devices with different centre area widths

Next, simulations have been carried out to determine the influence of the width of the centre area of the resonator on the device sensitivity. Two device models (device 1 and 3 from Tab. 4.3) with two different centre area widths, 60 μm and 110 μm, have been simulated. The anchor beam length of 105 μm is the same for both devices. The results of the simulations are shown in Fig. 5.12.

It is expected from theory that the mechanical stiffness of a resonator will not be affected by the width of the centre area, so the response of the amplitude ratio as a function of relative stiffness change should be the same for both devices, which the FEM simulations have demonstrated, with the results from the two models being the same. Fig. 5.12 shows the results that both theory and simulation has produced for the two models.

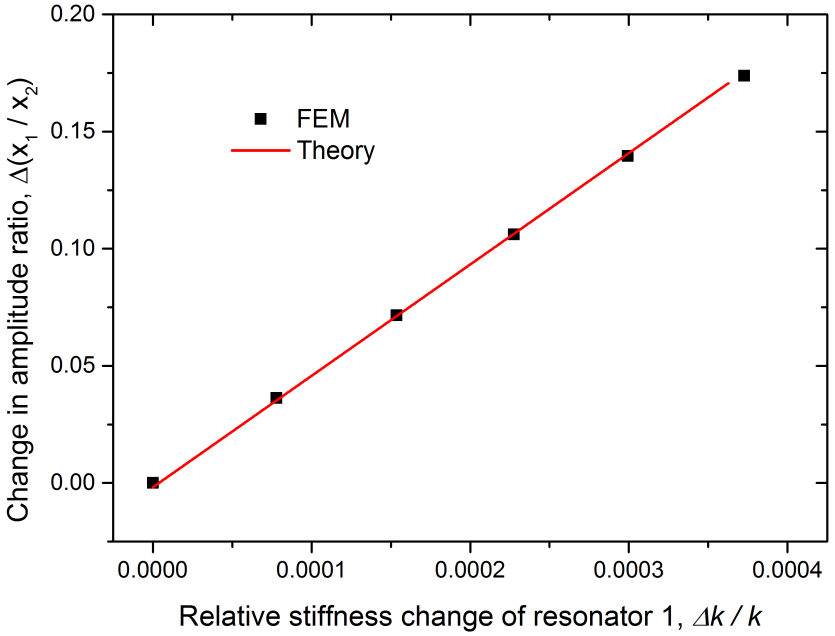

FIGURE 5.12: Theoretical and FEM simulated response of in-phase amplitude ratio to stiffness perturbation for coupled resonator devices with centre area dimensions of 310 × 60 μm and 310 × 110 μm, with 105 μm long anchor beams. Both devices have the same theoretical and simulated response.

5.4.4 FEM simulations of devices with different anchor beam lengths

Finally, FEM simulations have been performed to show the performance of coupled devices with different anchor beam lengths. 3D meshed models of devices 1, 4 and 5 from Tab. 4.3 have been used to simulate the amplitude ratio response to a an electrostatically induced stiffness increase on resonator 1. Fig. 5.13 shows the response of the amplitude ratio, x_1/x_2, to the relative change in stiffness, $\Delta k/k$, of resonator 1, for each of the three device designs, as well as the theoretically predicted behaviour.

It can be seen from Fig. 5.13 that the FEM simulated amplitude ratio response shows good agreement with the theoretical predictions for all three device designs. In addition, the sensitivity of the device, as defined previously, increases as a function of the anchor beam length, with shorter lengths resulting in more sensitive devices. From the theoretically derived equation (3.24), it is noted that the initial balanced effective stiffness, k, of the resonators does not influence the amplitude ratio response to the perturbation Δk. Therefore, a device's sensitivity, defined by its response to the relative stiffness change, $\Delta k/k$, will be increased for a higher initial balanced effective stiffness k, which has been confirmed by the FEM simulations.

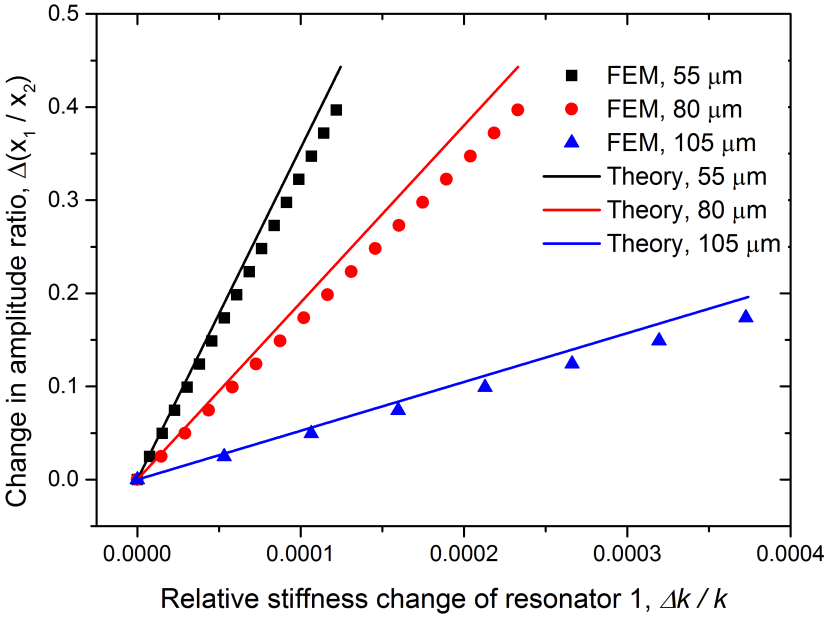

FIGURE 5.13: Theoretical and FEM simulated response of in-phase amplitude ratio to stiffness perturbation for coupled resonator devices with centre area dimensions of 310 × 60 μm, with anchor beam lengths of 55, 80 and 105 μm.

5.5 Summary

In this chapter, it has been demonstrated that for the designs of device that have been fabricated, FEM simulations of mode-localisation performed with *CoventorWare* agree with the theory. The model included anchors and surrounding substrate, with the boundary conditions set to allow for the absorption of vibration energy at the anchors, simulating anchor loss. In addition, squeezed film damping that would result from atmospheric gas molecules has been included in the model.

The results of the simulations will be compared to the experimental results from fabricated devices in the later chapters of this thesis.

Chapter 6

Initial mode-localisation experiments

6.1 Introduction

The following chapter will detail the initial experiments that have been performed with a fabricated coupled MEMS resonator device. The aim is to apply bias voltages to the resonators and electrodes to create an electrostatic spring between the resonators and then measure successfully the two mode frequencies (out-of-phase and in-phase) of the coupled system. Then, the stiffness of one of the resonators will be electrostatically increased in order to induce mode-localisation. The successful realisation of mode-localisation in the coupled system will be validated by measuring the shift in the mode frequencies, with the expected result being curve-veering behaviour in accordance with the theory (Fig. 3.4).

The electrical circuit that has been used to extract the frequency and amplitude of the resonator oscillations will be explained. In addition, the set up of the printed circuit board and the vacuum chamber will be outlined. This chapter will validate the measurement set-up, and the results in later chapters will be obtained using the same arrangement.

The experiments in this chapter will show the successful measurement of the out-of-phase and in-phase mode frequency peaks of a pair of clamped-clamped beams with the design of device 3 from Tab. 4.1. The design has been chosen because the bonded device proved to be reliable, with no issues concerning the wire-bonding and PCB soldering. The influence of a stiffness increase of one beam on the mode frequencies will be investigated, with the successful demonstration of mode-localisation. In addition, the influence of the coupling spring strength on the mode-localisation behaviour will be shown experimentally by varying the applied DC bias voltages.

6.2 Testing circuit design and manufacture

In order to measure the amplitude and frequency of the oscillations of a MEMS resonator, a testing circuit is required. For the testing of the devices in this thesis, the electrical measurement of the vibration amplitudes of the resonators is performed by measuring the output motional current from each of the resonators. The relationship between the motional current and the velocity of the vibrating structure is defined by the transduction factor, η [35], as follows

$$i_{mot} = \eta \dot{x} \tag{6.1}$$

For the resonator devices in this research, the vibrating resonator and the fixed electrode can be thought of as the plates of a parallel plate capacitor. For a parallel plate capacitor with a moveable plate, the transduction factor, η, can be expressed as

$$\eta = V_{dc} \frac{\varepsilon A}{g^2} \tag{6.2}$$

where V_{dc} is the DC bias voltage across the capacitor, ε is the permittivity, A is the area of the capacitor plates and g is the gap between the plates [35]. If the displacement, x, of the resonator with respect to time is expressed as

$$x = x_{peak} sin\omega t \tag{6.3}$$

then the velocity of the resonator, $\dot{x}$ is given by

$$\dot{x} = x_{peak} \omega cos\omega t \tag{6.4}$$

where x_{peak} is the peak displacement of the resonator and ω is the frequency of oscillation. Therefore, (6.2) and (6.4) can be substituted into (6.1) to give the following expression for the motional current

$$\begin{aligned} i_{mot} &= \eta \dot{x} \\ &= V_{dc} \frac{\varepsilon A}{g^2} x_{peak} \omega cos\omega t \end{aligned} \tag{6.5}$$

From (6.5), the peak of the alternating motional current, i_{peak0}, from a vibrating resonator at a modal frequency, $\mathrm{f_0}$, can be derived as

$$i_{peak0} = V_{dc}\frac{\varepsilon A}{g^2}x_{peak}\omega_0 \tag{6.6}$$

For this experiment, the wire-bonded MEMS chip has been plugged into a socket that has been mounted on a printed circuit board (PCB) that contains the necessary input and output circuitry. Fig. 6.1 shows an SEM of a bonded MEMS device and the connections to the schematic of the PCB circuitry.

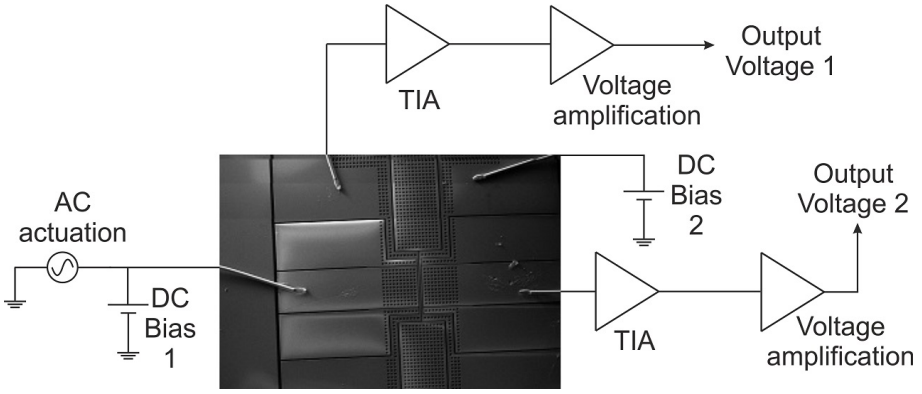

FIGURE 6.1: Experimental set-up. Coupled clamped-clamped beams MEMS device has been wire-bonded to carrier positioned on printed circuit board containing output circuitry.

As with the FEM simulations (chapter 5), electrostatic spring softening has been introduced to the two resonators by applying a positive DC voltage to electrode 1 (DC bias 1) and a negative DC voltage to resonator 2 (DC bias 2). Both resonator 1 and electrode 2 are held at 0 V, as they are connected to the inputs of two transimpedance amplifiers (TIAs). If the two DC bias voltages are of an equal magnitude but opposite polarity, then an equal value of electrostatic spring softening will be applied to each resonator, in accordance with (5.1). In addition, the electrostatic coupling spring between the two resonators has been created from the potential difference, ΔV, between the negative DC voltage on resonator 2 and 0 V on resonator 1.

For this initial experiment, the device used is a pair of clamped-clamped beams of length 460 μm and width 10 μm, which is device design 3 from Tab. 4.1. DC bias 1 has been set at 113.25 V and DC bias 2 has been set at -113.25 V, resulting in a coupling spring, k_c, of -20.9 N/m and electrostatic spring softening, k_{elec}, of -20.9 N/m on both resonators. Using a coupling spring of -20.9 N/m should result in out-of-phase and in-phase frequencies of 411.53 kHz and 417.48 kHz, ensuring sufficient separation of the two resonant peaks, ensuring no mode-aliasing. The resonators have been driven by applying an AC sinusoidal voltage from a signal generator to electrode 1. A 1 V peak-to-peak signal has been used as this has been found to drive the resonators without any non-linear behaviour, so the peaks can be reliably measured.

The vibration amplitudes of the coupled resonator pair have been extracted by measuring the motional currents from the capacitive transduction gaps between each resonator and its neighbouring electrode. As can be seen from Fig. 6.1, the motional currents from the vibrating resonators have been converted to voltage signals, using two TIAs (OPA657 from Texas Instruments). Subsequently, the voltage signals from the TIAs have been amplified (AD8065 from Analog Devices) to give output voltages of at least 100 mV amplitude. The PCB containing the output circuitry is shown in Fig. 6.2. The PCB layout has been designed using EAGLE and manufactured by Newbury Electronics Ltd. All components have been sourced from suppliers and soldered to the PCB, with the D-connector providing the means to make input and output connections to the testing circuit.

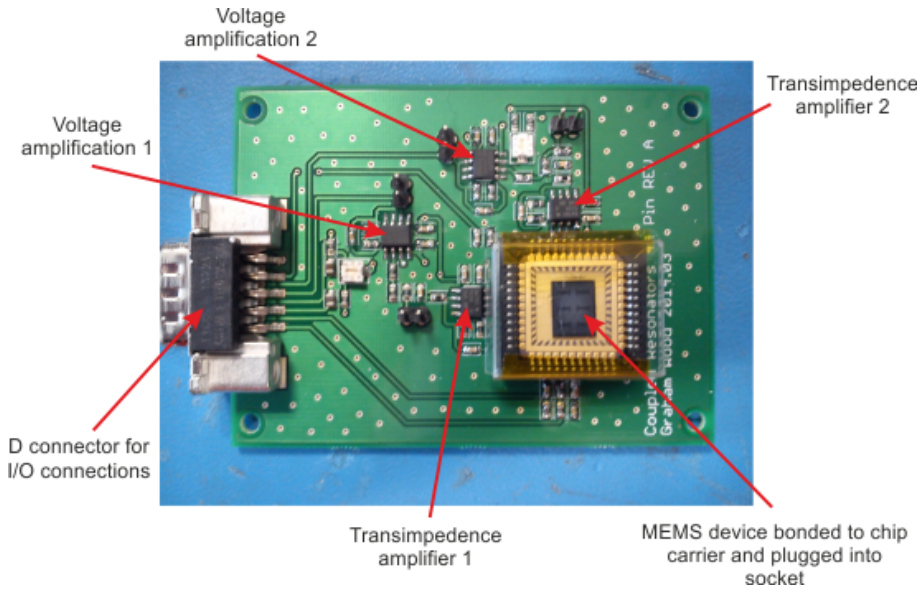

FIGURE 6.2: Testing circuit PCB.

A spectrum analyser (Rohde and Schwarz FSV 3) has been used to measure the output voltage signal from resonator 1 and resonator 2. The AC input signal has been swept across a frequency range while the amplitude of the output voltages is being measured. The out-of-phase and in-phase mode frequencies have been identified as the frequencies with the largest amplitudes. After identifying the modes, the frequency sweep range of the actuation signal is narrowed and the peak frequency and amplitude are measured for the in-phase mode for both resonator 1 and resonator 2. By comparing the amplitudes of the output voltage signals at the in-phase mode frequency, the vibration amplitude ratio of the resonator pair can be extracted.

6.3 Vacuum testing set-up

The characterisation experiments have been performed with the PCB secured in a vacuum chamber. Using a BOC Edwards EXT75DX turbo pump, the pressure inside the

chamber has been maintained at $3{\times}10^{-5}$ mbar, minimising atmospheric damping and allowing for high-Q resonant peaks to be achieved. The complete testing set-up is shown in Fig. 6.3.

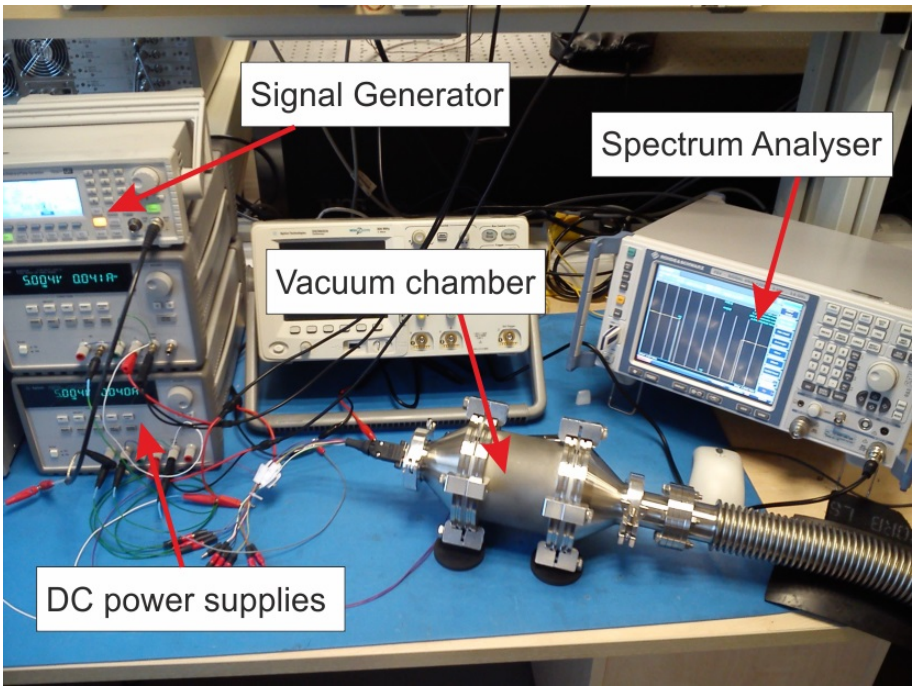

FIGURE 6.3: Device testing set-up.

The necessary electrical connections to the PCB have been made possible through the use of a D-connector feedthrough, which allows for all the connections to the D-connector on the PCB to be made from outside the chamber. All the DC and AC voltages can be applied and the output signals can be measured.

6.4 Mode-localisation demonstration

For each of the two output signals, the spectrum analyser has measured the amplitude of the varying output voltage signal across the range of the frequency sweep. For the device under test, several sweeps have been performed to identify the mode frequencies. A pair of peaks has been found in the range between 353 kHz and 360 kHz. Therefore, a 500 second sweep across that range with a 1 $V_{p\text{-}p}$ signal has been performed and the outputs have been measured and are shown in Fig. 6.4 and Fig. 6.5.

From Fig. 6.4 and Fig. 6.5, the peaks of the two mode frequencies can be seen clearly, demonstrating that the system is coupled together successfully and possesses an out-of-phase and an in-phase mode. It can be seen that the measured mode frequencies are lower than the theoretically predicted values of 411.53 kHz and 417.48 kHz, which is due to fabrication tolerances. When the BOX is removed by the HF vapour etching, addition oxide will be removed at the anchors due to the overetch that has been preformed to

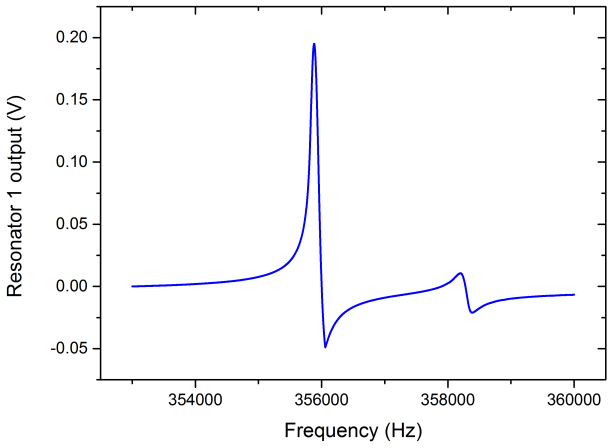

FIGURE 6.4: Output from resonator 1 for coupled resonator device with 460 × 10 μm beams.

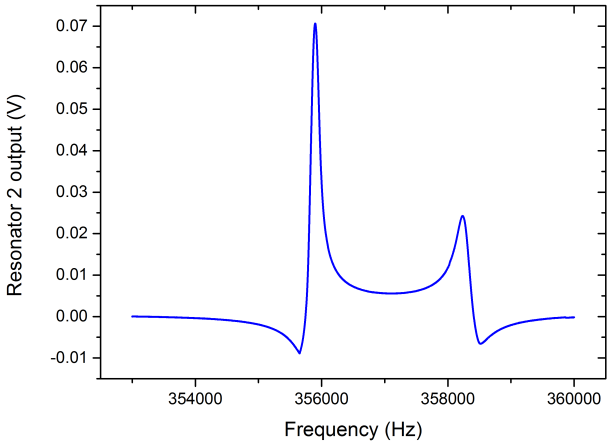

FIGURE 6.5: Output from resonator 2 for coupled resonator device with 460 × 10 μm beams.

ensure device release. The addition oxide (up to 10 μm) removed will have the effect of adding additional length to the resonators, which will have the result of lowering the mode frequencies, which is what has been measured.

From these measurements, the ratio of the peak output signals from the two resonators can be determined for each of the modes. The ratio is determined in the same way when testing the behaviour of all other fabricated devices that have been tested in this thesis.

The Q-factors of the peaks have been calculated from the frequency sweep results shown in Fig. 6.4 and Fig. 6.5. The lowest value is 1869, with the peak possessing a 3 dB bandwidth of 192 Hz. Therefore, to sufficiently minimise mode-aliasing, the separation of the out-of-phase and in-phase mode frequencies, Δf, should be at least $2 \times \Delta f_{3dB} =$ 384 Hz. The measured value for Δf is 2300 Hz, which is $12 \times BW_{3dB}$. so mode-aliasing has been avoided.

It can be seen from Fig. 6.4 and Fig. 6.5 that the peaks do not exhibit any non-linear behaviour, with no fold-over effect present.

In order to demonstrate the phenomenon of mode-localisation, the stiffness of resonator 1 has been increased while maintaining the stiffness of resonator 2. The increase in the stiffness of resonator 1 has been achieved by decreasing the DC voltage on electrode 1, which results in a decrease of the electrostatic spring softening of resonator 1. From the start value of 120 V, the value of the DC voltage on electrode 1 has been decreased incrementally and after each decrease, frequency sweeps have been performed and the output signals have been extracted. Fig. 6.6 and Fig. 6.7 show the output from resonator 1 and resonator 2, respectively, as the stiffness of resonator 1 is increased.

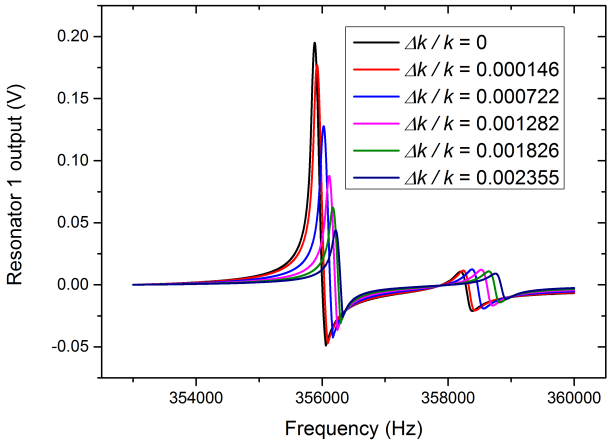

FIGURE 6.6: Output from resonator 1 for coupled resonator device with 460 × 10 μm beams. The relative stiffness increase of resonator 1 ($\Delta k/k$) for each graph is shown in the legend.

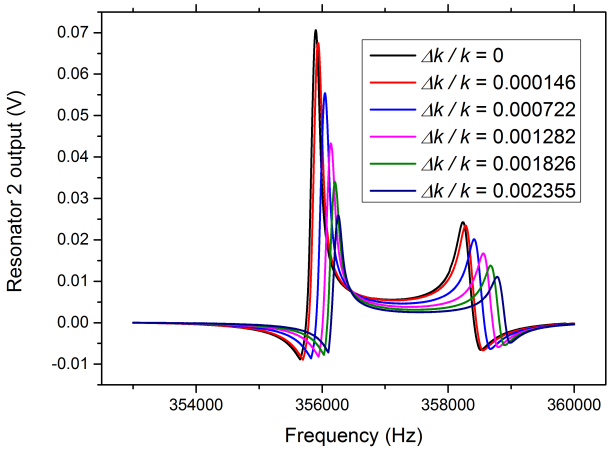

FIGURE 6.7: Output from resonator 2 for coupled resonator device with 460 × 10 μm beams. The relative stiffness increase of resonator 1 ($\Delta k/k$) for each graph is shown in the legend.

It can be seen that the amplitude and frequency of the peaks shifts in response to the introduction of a stiffness imbalance. If the two mode frequencies are plotted so their

response to the relative stiffness increase can be seen, the graph of Fig. 6.8 is the result. It can be seen that the two mode frequencies diverge in response to an increasing stiffness perturbation being applied to the system, as expected from the theoretically derived response seen in Fig. 3.4. Around the balanced zone, where the two resonators should have the same stiffness because the DC voltages are equal, there is a "veering neck" where the frequencies are at their closest. As discussed earlier in chapter 3, according to theory the two modes cannot occur at the same frequency, with the veering behaviour exhibited by the device being the result.

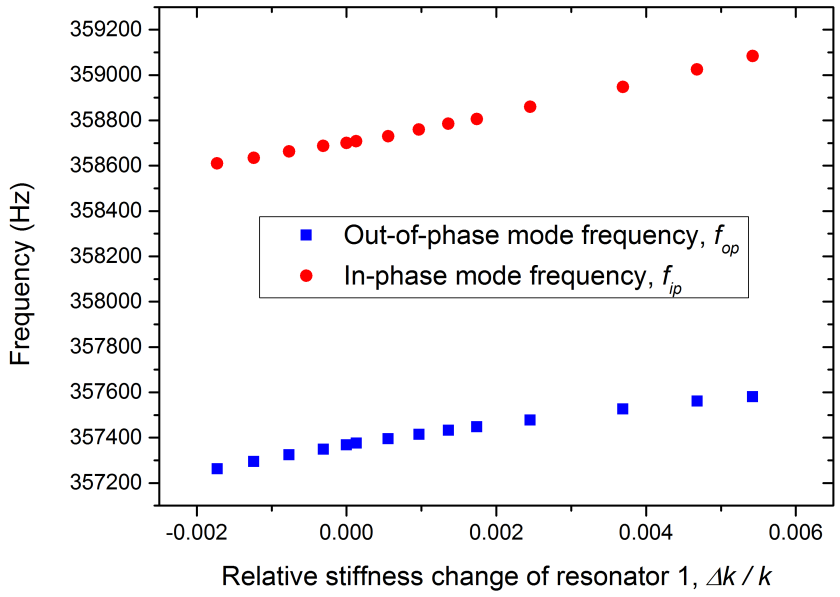

FIGURE 6.8: Out-of-phase and in-phase mode frequencies response to the relative stiffness increase of resonator 1 for coupled resonator device with 460 × 10 μm beams and $k_c = 11.75$ N/m.

At the veering neck the out-of-phase and the in-phase modes are separated by 1325 Hz and the separation value, Δf, is increased up to 1500 Hz for a relative stiffness increase of 0.0055 on resonator 1. The graph of Fig. 6.9 illustrates how the separation of the two mode frequencies responds to a stiffness increase on resonator 1, with the close spacing at the veering neck clearly demonstrated. Also, the results show that the device is relatively well matched with the narrowest gap between the modes occurring when the electrostatic spring softening applied to the two resonators is almost equal. A small decrease in the stiffness of resonator 1 is needed to balance the system, indicating that there is a slight mismatch in the mechanical stiffness of the two resonators, which is the result of fabrication tolerances.

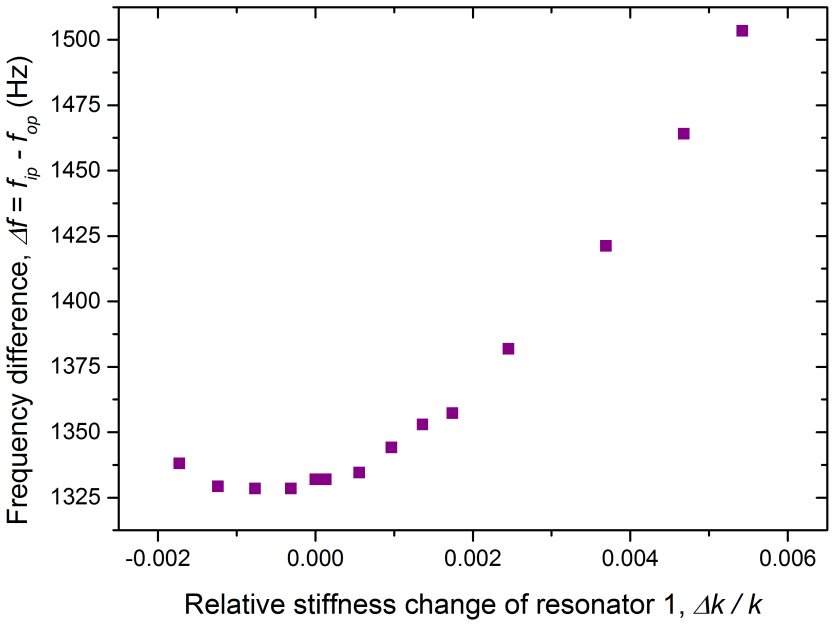

FIGURE 6.9: Change in separation of mode frequencies in response to a relative change in the stiffness of resonator 1. $k_c = 11.75$ N/m

6.5 Varying the coupling spring

Experiments have been performed on the clamped-clamped beams device to demonstrate the effect of varying the strength of the coupling spring, k_c. From the theoretically derived expressions given by (4.7) it can be seen that for a weaker coupling spring, k_c, the two mode frequencies should be closer together. To confirm the behaviour of the device in response to a change in k_c, the DC voltages on electrode 1 and resonator 2 have been reduced from their starting values of 120 V and -120 V, so that the strength of the coupling spring reduces according to (3.9). Fig. 6.10 shows the response of the two mode frequencies to a stiffness perturbation for two different values of coupling spring, 20.9 N/m and 11.73 N/m.

It can be seen from Fig. 6.10 that the out-of-phase and in-phase frequencies increase in response to a weaker coupling spring and that the two frequencies move closer together, as predicted by the theory. The experiment has been repeated for several values of coupling spring and the response of the width of the veering neck, which is the point at which the the two mode frequencies are closest, has been plotted, as shown in Fig. 6.11. The narrowing of the veering neck in response to a weaker coupling spring can be seen clearly, with the separation of the modes at the veering neck, Δf, always at least $2 \times BW_{3dB}$. The important result that has been obtained is that for the lowest value of coupling spring, $k_c = 11.73$, the two mode frequencies are separated by more than $3 \times BW_{3dB}$, ensuring that no mode-aliasing occurs.

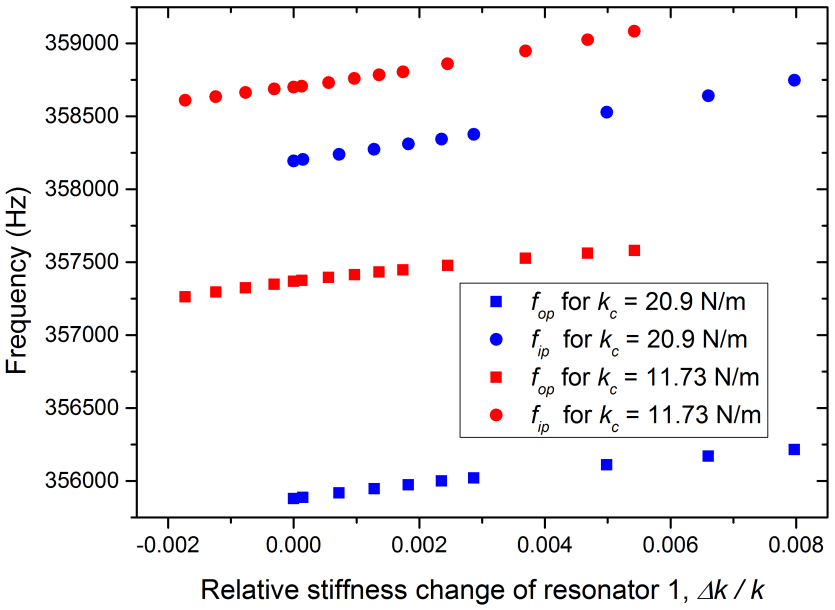

FIGURE 6.10: Curve veering behaviour for two different values of coupling spring strength, k_c.

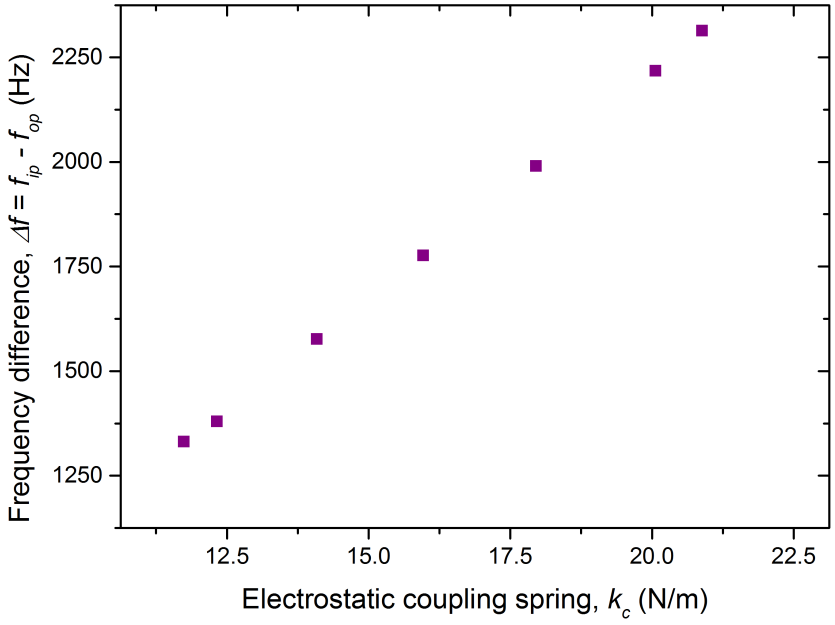

FIGURE 6.11: Response of the veering neck width to a change in the coupling spring, k_c.

6.6 Summary

In this chapter, the frequency response to a stiffness perturbation of an electrostatically coupled pair of clamped-clamped beams has been characterised. The device has behaved according to the theory that has been derived in chapter 3. As expected, introducing a stiffness imbalance to the coupled system results in a divergence of the out-of-phase

and in-phase mode frequencies. Mode veering behaviour has been demonstrated, with a weaker coupling spring resulting in the two modes being closer to one another, but still satisfying the anti-aliasing condition.

Also in this chapter, the method for measuring the amplitude ratio of the resonator pair at the mode frequencies has been explained. In the next chapters, the response of the vibration amplitude ratio to a stiffness or mass imbalance will be characterised for different designs of coupled resonator device.

Chapter 7

Effect of varying structural dimensions on device performance

7.1 Introduction

The main focus of the experiments reported on in this chapter is the response of the ratio of the vibration amplitudes of a pair of electrostatically coupled MEMS resonators. Specifically, the response of the amplitude ratio at the mode-frequencies to a change in the stiffness of one of the two resonators. All of the device designs that have been introduced in chapter 4 have been characterised and their mode-localisation behaviour has been compared to that predicted by the FEM simulations in chapter 5.

For the clamped-clamped beams design, the influence of beam width and length on device sensitivity has been determined. For the devices of the larger centre area design, the effect of the centre width on sensitivity has been determined. In addition, the effect of anchor beam length on device sensitivity has been characterised.

Lastly, this chapter will detail the results of stiffness perturbation experiments that have been performed on devices of the folded anchor beam design, fabricated with the NPU process. A comparison between the different designs has been made and the results have been compared to the most sensitive devices reported in the literature.

For the measurements that are performed in this chapter, the experimental methodology that has been outlined in chapter 6 has been used to extract the amplitude ratios at the in-phase mode frequency. For each design of device, a single sample has been characterised. Each sample is ideally measured 2 or 3 times and an average result is produced. However, due to the time involved in fully characterising a devices (up to a day) and some reliability issues with the measurement set-up, in particular the PCB, some devices have been characterised only once. Where multiple measurements have been performed, error bars are displayed on the graph showing the spread of results.

	Measured modes		
Beam dimensions (μm)	f_{op} (kHz)	f_{ip} (kHz)	$k_{1,2}$ (N/m)
410 × 10	427.897	429.082	1389
410 × 20	954.376	954.84	13759

TABLE 7.1: Experimentally measured mode frequencies and corresponding effective stiffness.

7.2 Simple beams design

7.2.1 Beam width

The first experimental characterisation has been performed on devices of the simple clamped-clamped beams design (Fig. 4.26). Two devices have been characterised, one with beams of dimensions 410 μm × 10 μm and the other 410 μm × 20 μm (devices 1 and 2 from Tab. 4.1). The same testing arrangement has been used as in the previous chapter (Fig. 6.1). As calculated in (5.1), an electrostatic coupling spring of -20.9 N/m has been formed between the beams by applying -120 V to resonator 2 and holding resonator 1 at 0 V. The DC voltage of electrode 1 has been set to 120 V and electrode 2 has been held at 0 V, so that the potential difference, ΔV, between each resonator and its neighbouring electrode is 120 V, which electrostatically softens the stiffness of each resonator equally according to (3.9).

The initial mode frequencies have been measured for both devices and the values are listed in Tab. 7.1. Comparing with theoretical values for the mode frequencies in Tab. 4.2, it can be seen that the experimental measured frequencies are lower, which is likely as a result of fabrication tolerances at the anchors, leading to a lower resonator stiffness. Taking the measured values for the mode frequencies, an estimation of the resonator stiffness has been calculated using (4.3) for each device and is listed in Tab. 7.1.

In addition to the mode frequencies, the Q-factor and 3 dB bandwidth, Δf_{3dB}, of the resonant peaks has been determined. Tab. 7.2 shows the values for Δf_{3dB} for each device. The variation in Q-factor values, including when compared to the device characterised in chapter 6, can be attributed to fabrication variations. However, the spread of values seen from the measurements presented throughout this chapter demonstrate that the assumed value of 10,000 used for theoretical calculations is a fair estimate. It can be seen that the separation of the out-of-phase and in-phase mode frequencies, Δf, is at least 2 × Δf_{3dB}, so mode-aliasing has been sufficiently minimised.

Beam dimensions (μm)	Q-factor	3 dB bandwidth, Δf_{3dB} (Hz)	Mode separation, Δf (Hz)
410 × 10	3237	133	1185
410 × 20	15154	63	464

TABLE 7.2: Experimentally measured device characteristics.

Next, the DC voltage of electrode 1 has been reduced from the starting value of 120 V, so that the stiffness of resonator 1 is increased and the response of the amplitude ratio of the two output signals has been extracted. The same experiments have been performed on the 10 μm and 20 μm wide beam devices. The stiffness of the left resonator has been increased in increments so that the relative stiffness ($\Delta k/k$) increases by up to 400 ppm. Fig. 7.1 and Fig. 7.2 show the response of the amplitude ratio (x_1/x_2) at the in-phase mode frequency to the shift in relative stiffness ($\Delta k/k$) of resonator 1. It can be seen that the FEM simulated and experimental results show good agreement, for both the 10 μm and 20 μm wide beam devices.

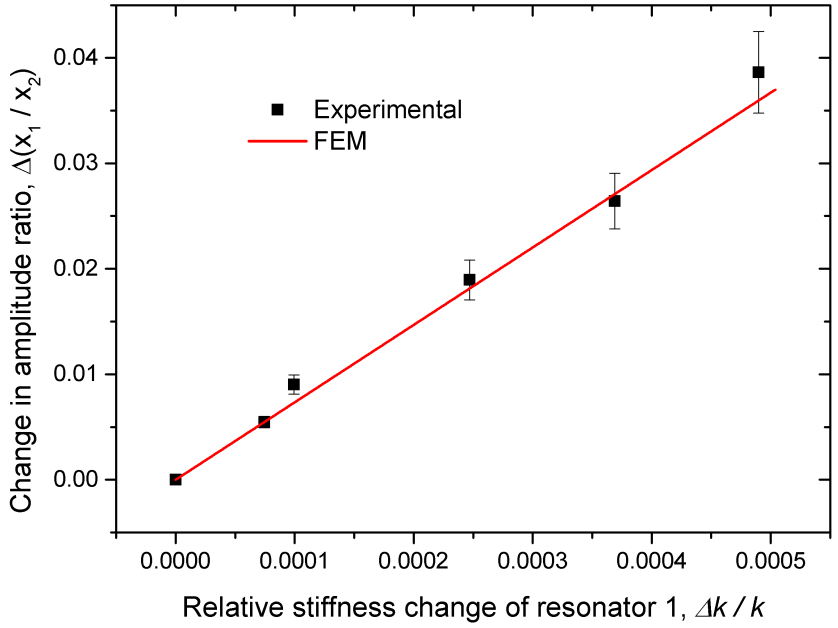

FIGURE 7.1: Change in amplitude ratio at the in-phase mode frequency in response to stiffness change of resonator 1 for pair of 410 $\times$ 10 μm clamped-clamped beams.

The sensitivity, S_k, of the device is defined as the response of the amplitude ratio (x_1/x_2) at the in-phase mode frequency to the shift in relative stiffness ($\Delta k/k$) of resonator 1 as given by (3.25). A sensitivity of 75 has been measured for the 10 μm wide beam and 1000 for the 20 μm wide beam, which compares favourably to the current state-of-the-art value of 356 [93].

As discussed in chapter 3, the sensitivity of a device to a relative change in the stiffness should be higher for devices with a higher initial stiffness. The results in Fig. 7.1 and Fig. 7.2 confirm the relationship with the sensitivity being 13 times higher for the 20 μm wide beam device, compared with the 10 μm wide beam device, because of its higher initial stiffness.

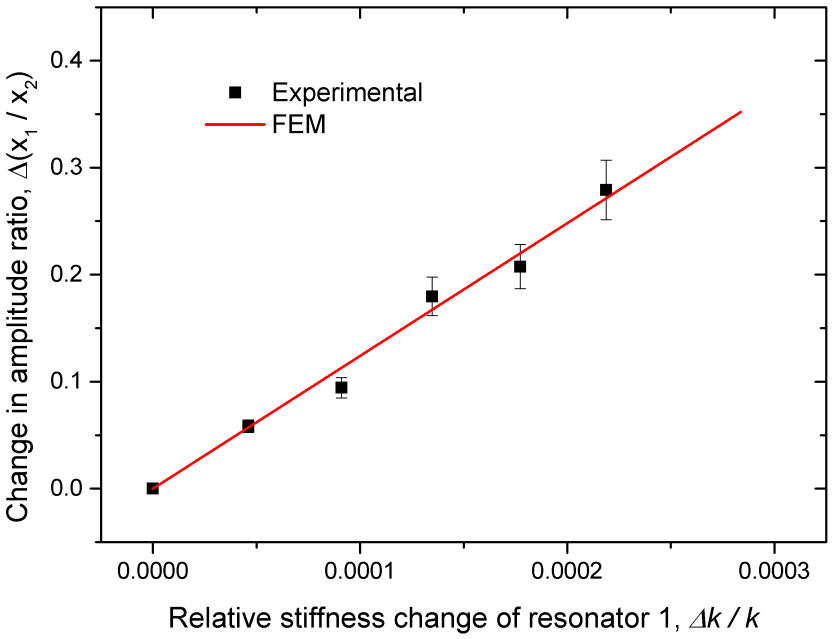

FIGURE 7.2: Change in amplitude ratio at the in-phase mode frequency in response to stiffness change of resonator 1 for pair of 410 × 20 μm clamped-clamped beams.

	Measured modes		
Beam dimensions (μm)	f_{op} (kHz)	f_{ip} (kHz)	$k_{1,2}$ (N/m)
410 × 10	427.897	429.082	1389
460 × 10	355.88	358.194	1086
510 × 10	296.115	297.609	832

TABLE 7.3: Experimentally measured mode frequencies and corresponding effective stiffness.

7.2.2 Beam length

The next set of experiments performed has been to determine the amplitude ratio response to stiffness perturbation for coupled clamped-clamped beams of different lengths. Devices of design 3 and design 4 from Tab. 4.1 have been characterised. The beam width for both devices is 10 μm, with a length of 460 μm for one device and 510 μm for the other. The out-of-phase and in-phase mode frequencies have been measured and are given in Tab. 7.3. As before, it has been found that the measured frequencies are lower than the theoretically calculated values, due to a lower mechanical stiffness resulting from fabrication tolerances.

Tab. 7.4 shows the Q-factor measurements on the devices with different lengths and it can be seen that the separation of the mode frequencies is more than sufficient to prevent the occurance of any mode aliasing.

Taking the FEM simulations results that have been presented in Fig. 5.9 in chapter 5 for comparison, the amplitude ratio response of the two device designs has been experimentally determined. The results are shown in Fig. 7.3 and Fig. 7.4.

Beam dimensions (μm)	Q-factor	3 dB bandwidth, Δf_{3dB} (Hz)	Mode separation, Δf (Hz)
410 × 10	3237	133	1185
460 × 10	3597	100	2314
510 × 10	5871	50	2737

TABLE 7.4: Experimentally measured device characteristics.

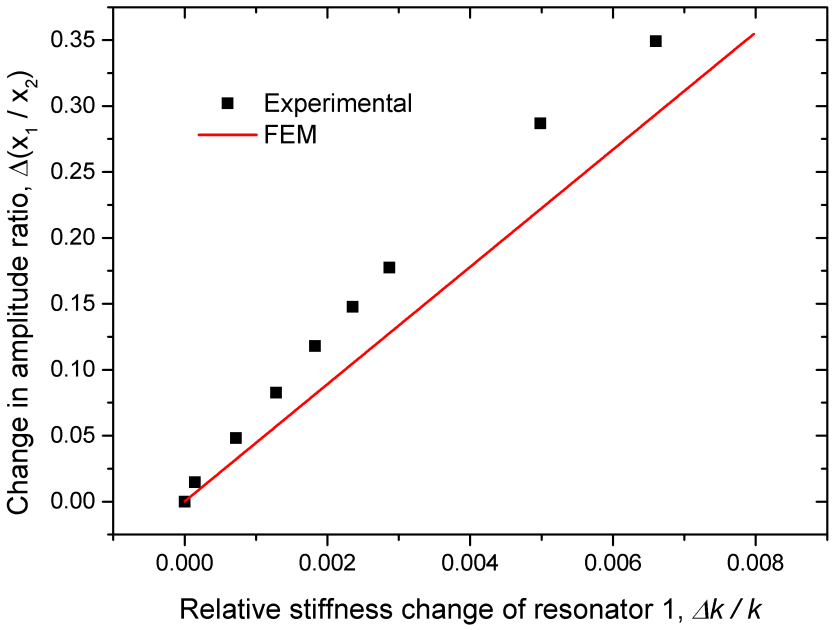

FIGURE 7.3: Change in amplitude ratio at the in-phase mode frequency in response to stiffness change of resonator 1 for pair of 460 × 10 μm clamped-clamped beams.

It can be seen from Fig. 7.3 and Fig. 7.4 that the sensitivity is higher for the coupled resonator device with shorter beams, in agreement with theory and simulation. For the device with 460 μm long beams, a sensitivity of 45 has been measured and for the device with 510 μm long beams, a sensitivity of 34 has been measured. When the sensitivity of 75 for the device with 410 μm long beams is considered, the trend of greater sensitivity for devices with resonators with greater mechanical stiffness is clear.

7.3 Larger centre area design

7.3.1 Centre area width

The next set of experimental measurements that have been performed has been the characterisation of devices of the larger centre area design (Fig. 4.27). Initially, the behaviour of two devices have been compared, one with a centre area width of 60 μm and the other 110 μm. The length of the centre block is 310 μm and the anchor beam dimensions are 105 × 10 μm for both devices.

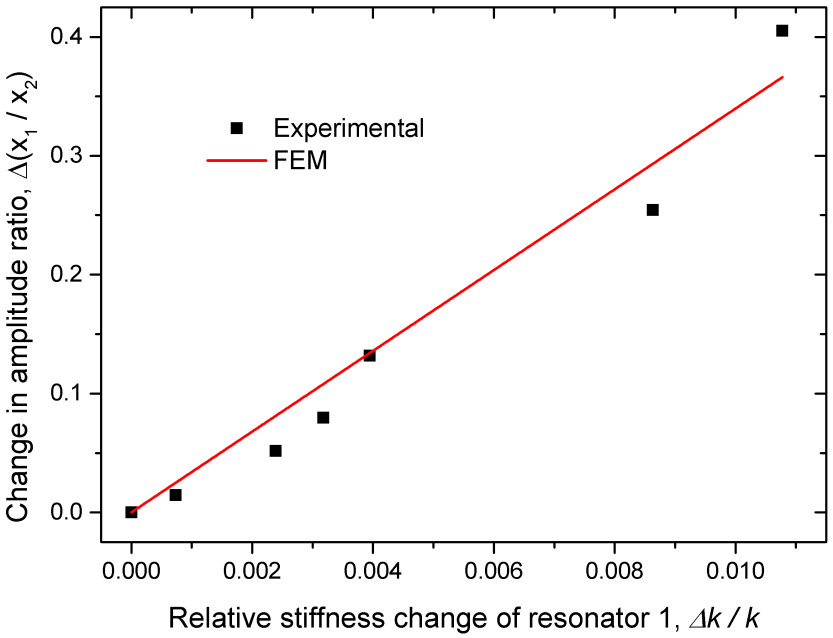

FIGURE 7.4: Change in amplitude ratio at the in-phase mode frequency in response to stiffness change of resonator 1 for pair of 510 × 10 μm clamped-clamped beams.

From theory and FEM simulations (Fig. 5.12), it is expected that the sensitivity of the devices should be unaffected by the width of the centre block, as the mechanical stiffness should be unaffected. Fig. 7.5 shows the response of the amplitude ration at the the in-phase mode shape to a relative increase in the stiffness of resonator 1. Also, the FEM simulated amplitude ratio response is shown.

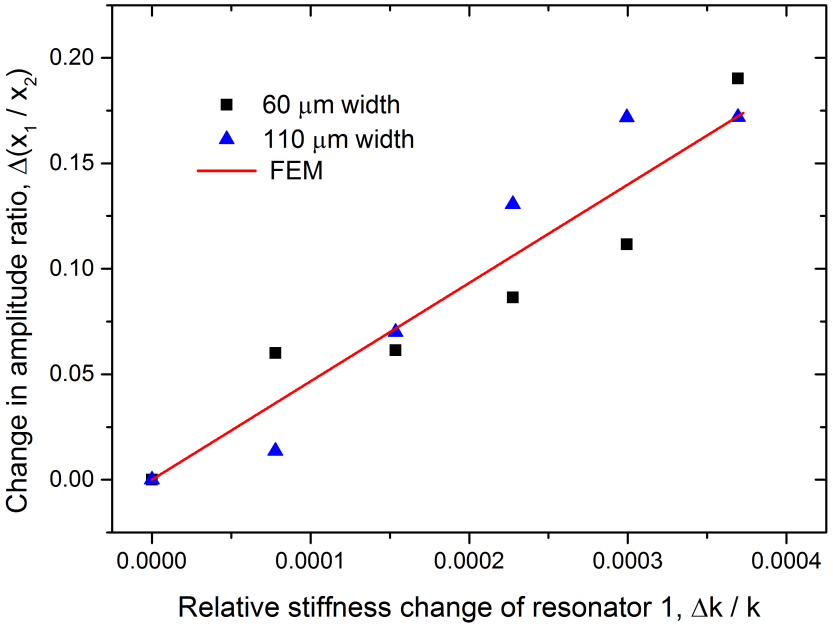

FIGURE 7.5: Change in amplitude ratio at the in-phase mode frequency in response to stiffness change of resonator 1 for pair of resonators with larger centre area. Results are shown for devices with centre area widths of 60 μm and 110 μm.

It can be seen that no significant difference in the amplitude ratio response can be

	Measured modes		
Anchor beam length (μm)	f_{op} (kHz)	f_{ip} (kHz)	$k_{1,2}$ (N/m)
55	1041.223	1041.605	95232
80	757.381	758.184	50863
105	328.005	328.543	9292

TABLE 7.5: Experimentally measured mode frequencies and corresponding effective stiffness

determined between the two devices. Both sets of results broadly agree with the FEM simulated trend, meaning that no improvement in sensitivity can be achieved through altering the centre area width. Additionally, it can be seen that, in accordance with the theory, the change in mass that results from the change in the centre area width does not influence the amplitude ratio response to a stiffness perturbation.

7.3.2 Anchor beam length

The previously outlined measurement method has been used to extract the out-of-phase and in-phase mode frequencies of each of the three device designs (55 μm, 80 μm and 105 μm anchor beam length). The measured values are shown in Tab. 7.5. The variation between the measured values and the theoretical values in Tab. 4.4 is likely as a result of fabrication tolerances and intrinsic stress in the SOI device layer. Taking the measured values for the mode frequencies, an estimation of the actual effective stiffness, k_1 and k_2, for each of the three resonator designs at the initial balanced state has been calculated using (3.16), with the values shown in Tab. 7.5.

As explained previously, starting from a balanced state, the two mode frequencies should diverge in response to a stiffness imbalance between the resonators. Fig. 7.6 shows the the experimentally measured difference between the out-of-phase and in-phase mode frequencies, for a device with 105 μm anchor beams, in response to an electrostatically induced stiffness increase on resonator 1. It can be seen that the frequency difference increases as a function of the stiffness perturbation, as expected. An initial imbalance would be expected between the resonators, due to fabrication tolerances and the trend shown in Fig. 7.6 suggests that for this device, resonator 1 has a higher stiffness than resonator 2. However, provided that the initial imbalance is sufficiently small, the amplitude ratio response should be linear with respect to the stiffness perturbation. For all three devices characterised in this section, the initial imbalance has been found to be less than 0.02 %, allowing for the linear behaviour of the amplitude ratio to be assumed.

The two mode frequencies are sufficiently separated when $\Delta k = 0$ so that the two modes are distinguishable and accurate measurements of the peak amplitudes can be made. The Q-factor of the modes for each device have been measured and are shown in Tab. 7.6, along with the 3 dB bandwidth, Δf_{3dB}, of the peaks. It can be seen that

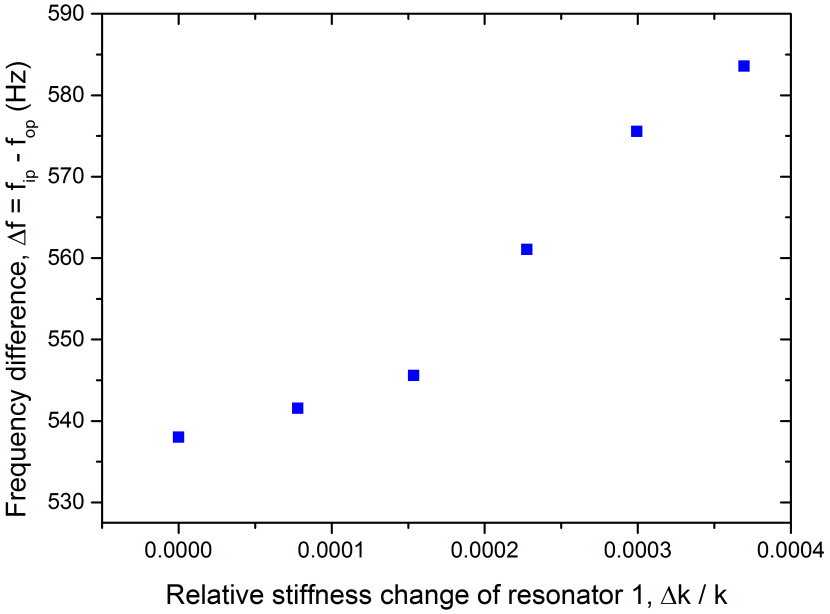

FIGURE 7.6: Measured response of frequency difference between the out-of-phase and in-phase modes for 2-DOF system to a relative stiffness change on resonator 1. The device measured has anchor beams with a length of 105 μm.

the separation of the out-of-phase and in-phase mode frequencies, Δf, is at least 2 $\times$ Δf_{3dB}, so mode-aliasing has been avoided.

For the device with 105 μm anchor beams, for a relative stiffness increase of 0.0004 for resonator 1, the in-phase mode frequency increased by 53 Hz, representing an relative increase of 0.016 %. Using the definition of (2.6), the frequency sensitivity has been calculated to be 0.4, which will be compared to the sensitivity of the amplitude ratio shift.

Anchor beam length (μm)	Q-factor	3 dB bandwidth, Δf_{3dB} (Hz)	Mode separation, Δf (Hz)
55	11768	88	382
80	6535	116	685
105	1950	169	538

TABLE 7.6: Experimentally measured device characteristics.

The experimentally measured amplitude ratio change, $\Delta(x_1/x_2)$, in response to an electrostatically induced relative stiffness increase, $\Delta k/k$, on resonator 1 is shown in Fig. 7.7, for all three device designs, along with the FEM simulated response.

The graph of Fig. 7.7 shows the expected trend of increasing amplitude ratio, x_1/x_2, as a function of increasing stiffness imbalance in the resonator pair. It can be seen that the measured values show good agreement with the simulated values, confirming the validity of both the theoretical equation (3.24) and the FEM model.

From (3.24), it is noted that the initial effective stiffness does not feature, with the

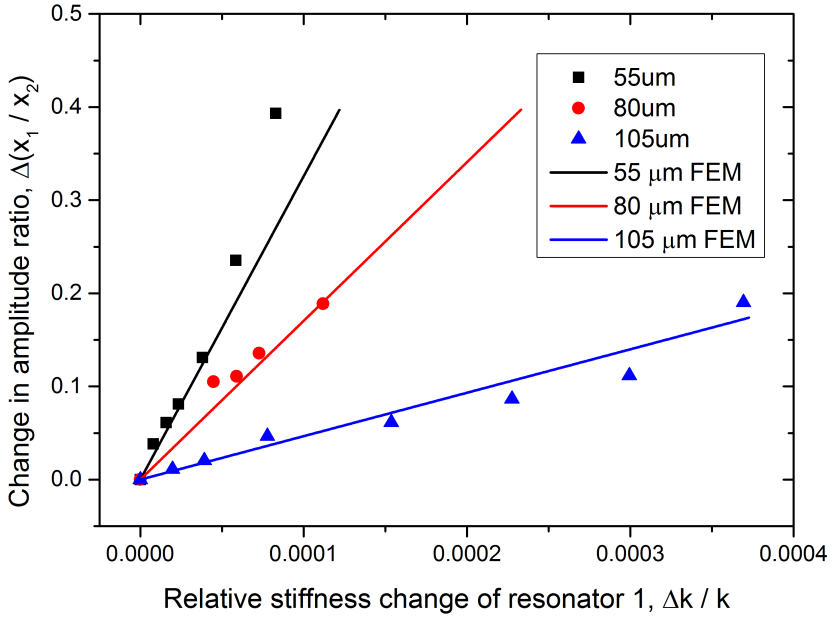

FIGURE 7.7: Measured response of amplitude ratio of 2-DOF system to a relative stiffness change on resonator 1 for devices with 55 μm, 80 μm and 105 μm anchor beam lengths.

coupling spring constant, k_c, and the change in stiffness of resonator 1, Δk, determining the amplitude ratio of the resonators at the in-phase mode frequency. Therefore, it is expected that a higher initial effective stiffness, k, leads to higher sensitivity with respect to relative stiffness change, $\Delta k/k$, as has been confirmed from the experimental measurements (Fig. 7.7).

From the amplitude ratio responses shown in Fig. 7.7, the sensitivities of the different device designs have been calculated and are listed in Tab. 7.7. It can be seen that the sensitivity for the coupled resonator devices decreases as a function of the length of the anchor beam, L_a.

Anchor beam length (μm)	Sensitivity, S_k
55	3257
80	1704
105	466

TABLE 7.7: Experimentally derived device sensitivities.

Taking the measurements from the device with 105 μm anchors, it has been demonstrated that the amplitude ratio shift of a coupled resonator system is more sensitive to a stiffness imbalance than the in-phase mode frequency shift (equivalent to resonant frequency shift of a 1-DOF system), with a four orders of magnitude difference, comparing a sensitivity of 0.4 for frequency shift to a sensitivity of 466 for amplitude ratio shift. Similarly, for the device with 55 μm anchor beams, the sensitivity of the in-phase resonant frequency to a relative stiffness change is 0.134, whereas the sensitivity of the amplitude ratio is 3257, also representing a four orders of magnitude increase. The find-

	Measured modes		
Anchor beam length (μm)	f_{op} (kHz)	f_{ip} (kHz)	$k_{1,2}$ (N/m)
120	796.893	797.688	84000
240	478.535	488.771	16410

TABLE 7.8: Experimentally measured mode frequencies and corresponding effective stiffness

ings agree with previously published studies [96], which characterised coupled resonators of the double-ended tuning fork design.

The best example of stiffness sensing for a 2-DOF coupled resonator system in literature [96] shows a sensitivity of 356, if the sensitivity definition in (3.25) is applied. From Tab. 7.7, it can be seen that the best sensitivity demonstrated for devices of the larger centre area design, 3257, is 9 times greater than the state of the art, demonstrating the importance of dimension variation in the design of 2-DOF coupled resonator sensors.

7.4 Folded-beam anchor design

In addition to the testing of the devices that have been fabricated using the Southampton process, two devices of the folded-beam anchor design fabricated using the NPU process have been tested. The design and dimensions of the two devices have been explained in chapter 4 and are listed in Tab. 4.5. The measured mode frequencies of the two devices that have been tested are listed in Tab. 7.8, along with the subsequently derived resonator stiffness.

The experimentally determined values for the resonator stiffness of each device is higher than the theoretical predictions. For each device, the initial DC voltages have been set so that the electrostatic coupling spring, k_c, is -14.16 N/m, to ensure sufficient mode separation, Δf. Fig. 7.8 and Fig. 7.9 show the amplitude ratio response to a stiffness increase on resonator 1 at the out-of-phase mode for the two devices. The out-of-phase mode is preferred for the devices of the folded-beam anchor design as the out-of-phase peaks have proved easier to identify and measure.

It can be seen that the sensitivity of the device with 120 μm folded-beam anchors (Fig. 7.8) is higher than for the device with 240 μm folded-beam anchors (Fig. 7.9). The theory from Fig. 4.33 and the trend of coupled devices with stiffer structures possessing greater sensitivity to relative stiffness increase have been confirmed. A sensitivity of 33964 has been measured for device design 1 and 11575 for device design 2. The sensitivity values are higher than the theoretical values of 5200 and 1147 for design 1 and design 2, respectively, that have been calculated in chapter 4. The explanation for the increased sensitivity has been attributed to a larger coupling gap for the fabricated device than the designed value of 3 μm, resulting in a weaker coupling spring, k_c, of

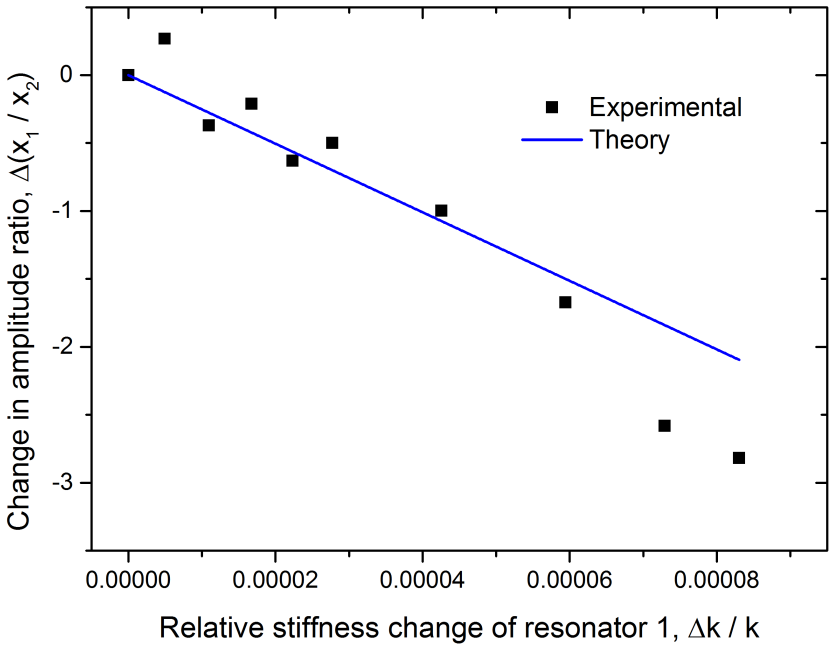

FIGURE 7.8: Measured response of amplitude ratio of 2-DOF system to a relative stiffness change on resonator 1 for devices with centre mass dimensions of 300 μm $\times$ 180 μm and 120 μm folded-anchor beam length.

-5.97 N/m. For the theoretical trends that have been plotted in Fig. 7.8 and Fig. 7.9, a coupling gap of 4 μm has been used for the calculation, resulting in an agreement with the measured amplitude ratio response.

As a result of the weaker coupling spring, the values are superior to the sensitivities seen for other device designs, suggesting that the folded-beam anchor may have greater potential for sensing applications. However, a drawback of devices fabricated with the NPU process is the unreliability of the fabricated coupling gaps and the increased likelihood of stiction occurring, resulting in less predictable behaviour, in terms of the mechanical and electrostatic stiffnesses.

7.5 Minimum detectable stiffness change

Published research [94] gives an expression for the signal-to-noise ratio (SNR) of a coupled resonator system. Using the expression to analyse the devices presented in this chapter, it is possible to determine the values of SNR. The expression for the SNR of the output of a coupled resonator is given by [94]

$$\mathrm{SNR} = \frac{\mathrm{SNR}_1 \times \mathrm{SNR}_2}{\mathrm{SNR}_1 + \mathrm{SNR}_2} \tag{7.1}$$

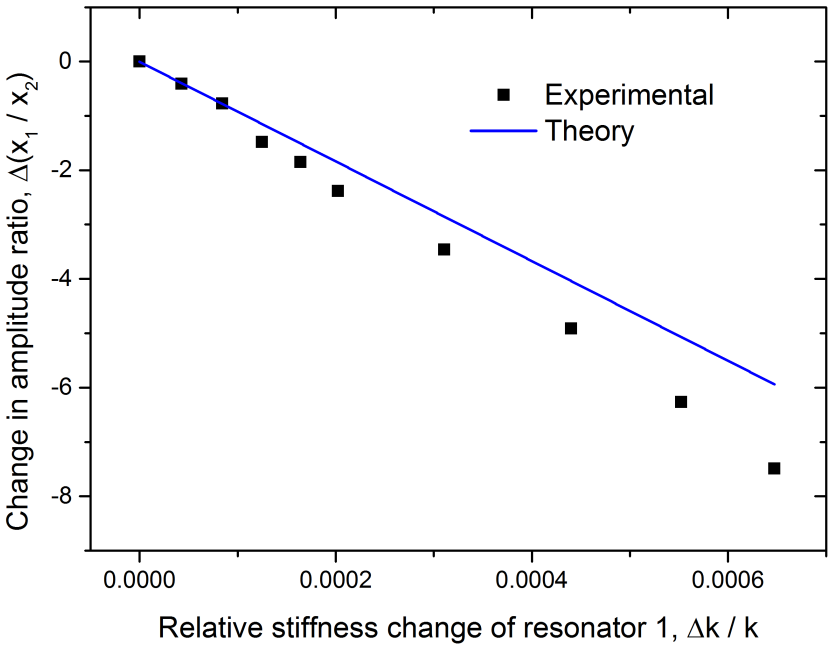

FIGURE 7.9: Measured response of amplitude ratio of 2-DOF system to a relative stiffness change on resonator 1 for devices with centre mass dimensions of 300 μm $\times$ 100 μm and 240 μm folded-anchor beam length.

where SNR_1 is the signal-to-noise ratio of the output from resonator 1 and SNR_2 is the signal-to-noise ratio of the output from resonator 2. The noise of the output from each resonator has been determined from the extracted output signal. Fig. 7.10 shows the in-phase resonant peak for a device of the larger centre area design (design 4 from Tab. 4.3). The noise in the output signal from resonator 2 can be clearly seen and it is possible to quantify it through visual inspection. The output from other devices has been examined similarly.

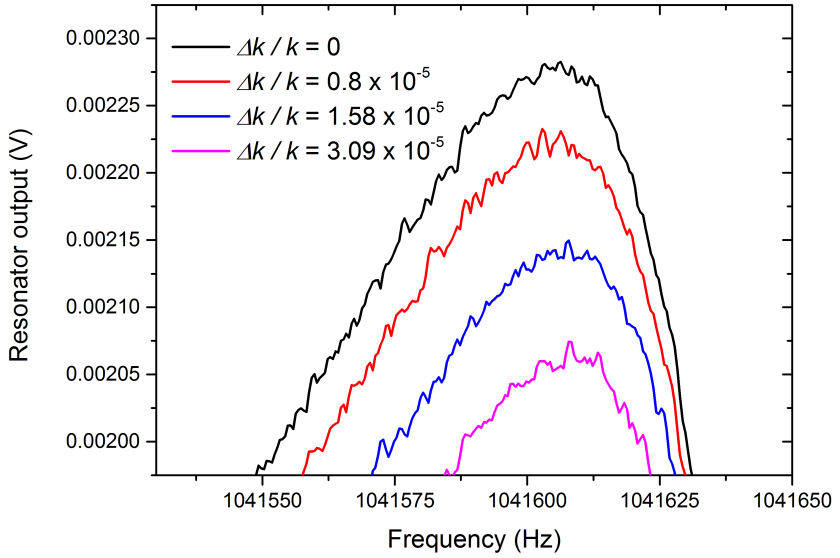

FIGURE 7.10: Zoomed in view of resonator 2 output signal showing noise.

A noise value of up to 2×10^{-5} V can be seen from the output resonant peaks. The

shift in the amplitude at the in-phase mode for resonator 2 has been measured to be 5.003×10^{-5} V for a relative stiffness change of 0.8×10^{-5}, giving an SNR of 6.26. A similar process has been performed with the output from resonator 1, which possesses an SNR of 272.25. Using (7.1) to calculate the SNR of the amplitude ratio of the signals from the two resonators, a value of 6.12 has been calculated, which also can be expressed as 7.87 dB.

It has been found that reliably measuring a relative increase in stiffness, $\Delta k/k$, below a value of 0.8×10^{-6} is not possible, as the change in amplitude ratio cannot be reliably measured due to an unacceptable SNR. As the device of design 4 from Tab. 4.3 has been shown to possess the greatest sensitivity of all the devices fabricated using the Southampton process, it can be concluded that the lowest minimum detectable relative stiffness change achieved is 0.8×10^{-6}, which compares favourably with previously reported mode-localised stiffness sensors outlined in chapter 3 that demonstrated a detection limit of 1.41×10^{-5}.

For the two devices fabricated using the NPU process that have been characterised for this work, similar calculations have been performed to determine the minimum detectable stiffness change. Device design 2 from Tab. 4.5 has been shown to possess the greatest sensitivity, so the minimum detectable relative stiffness change has been calculated for the device. For a relative stiffness change of 0.8×10^{-6}, it has been found the SNR is 9.4 dB. Therefore, it can be concluded that the NPU device can give a superior sensitivity with the same minimum detectable relative stiffness change.

7.6 Conclusion

This chapter has detailed the characterisation of the coupled resonator devices that have been fabricated for this research. Several devices with variations in dimensions have been the fabricated, allowing for the influence of the dimensions on the mode-localisation response to a stiffness perturbation to be characterised.

For the coupled clamped-clamped beams design, it has been found that the width of the beams has an effect on the device sensitivity, with beams of 20 μm width having 13 times the sensitivity to relative stiffness change compared to devices with 10 μm width. For devices of the larger centre area, it has been found that the sensitivity is greater if the anchor beam length is shorter, with the sensitivity found to be 7 times greater for a device with 55 μm anchor beam length compared to a device with 105 μm anchor beam length. When compared to the clamped-clamped beams devices, over 3 times improvement in sensitivity has been measured.

In addition to the improved sensitivity that has been demonstrated by the larger centre area device design, the design has a larger surface area, which can prove advantageous

for mass sensing, which will be explored in the next chapter. For example, the surface can be biologically functionalised so that an antigen of interest will bind to one of the resonators causing an imbalance.

Finally, devices of the folded-beam anchor design fabricated using the NPU process have been tested and it has been found that the sensitivity is greater than expected, probably due to a larger coupling gap than designed, due to the fabrication process. As a result of the weaker coupling, the highest sensitivity of the folded-beam anchor design is 5 times greater than the larger centre area devices fabricated using the Southampton fabrication process. Compared to the state-of-the-art, the highest sensitivity reported in this thesis is 46 times greater.

However, it should be noted that while the greatest sensitivity has been demonstrated with a device fabricated using the NPU process, in terms of fabrication yield, the Southampton fabrication process has been shown to be superior. The SOI fabrication process used at Southampton has been shown to have a high yield of over 95 % [13], which has been confirmed during the wafer-level fabrication for this thesis, while the yield for the NPU fabricated devices has been as low as 10 %, with extensive testing of devices required to find a successfully released resonator structures that can function as resonators. In addition, the behaviour of the Southampton fabricated devices has been shown to be more predictable than the NPU fabricated devices, with the fabricated coupling gaps being as designed. Therefore, future work could investigate folded-beam anchor devices fabricated using the Southampton process.

Chapter 8

Mass sensing

8.1 Introduction

The next area of mode-localisation based sensing to be explored in this thesis is the detection of a mass change in one of a pair of electrostatically-coupled MEMS resonators. The capability to detect a mass change can prove the feasibility of using a coupled resonator device as a biological or chemical sensor. This chapter will detail the experimental work that has been performed regarding mass sensing with a coupled-resonator device.

8.2 Experimental set-up

To determine the suitability as mass sensors of the devices that have been fabricated for this thesis, one of the devices that has been used for the stiffness sensing experiments in chapter 7 has been selected for further testing. The device chosen is a device of the design with a larger centre area as the architecture would allow for easier biological functionalisation and the larger surface area would promote the binding of the analyte to be detected. The dimensions of the centre block are 310 μm $\times$ 60 μm and the anchor beam length is 55 μm (device 4 from Tab. 4.3). Fig. 4.27 shows an SEM image of the device that has been chosen for the mass sensing experiments.

For the testing that is reported on in this chapter, the concept of mass sensing has been tested by removing mass from resonator 1, thus introducing an imbalance between the resonators, which should be detectable by extracting the amplitude ratio of the resonators as they are resonating at the in-phase mode frequency.

A DC bias voltage of -120 V has been applied to resonator 2, while resonator 1 has been held at 0 V, creating an electrostatic coupling spring, k_c, of -15.8 N/m between

them. DC voltages of 120 V and 0 V have been applied to electrode 1 and electrode 2, respectively, resulting in an equal level of electrostatic spring softening being applied to each resonator. Also, the characterisation of the mass sensing of the devices has been performed with DC voltages of 90 V and -90 V on electrode 1 and resonator 2, respectively, which allows for the influence of the coupling spring, k_c, on the mass sensitivity to be determined.

The same testing circuit (Fig. 6.1) and the same $3{\times}10^{-5}$ mbar vacuum chamber set-up (Fig. 6.3) as used for the stiffness sensing characterisation has been for the mass sensing characterisation. The amplitude ratio at the in-phase mode frequency of 1.0416 MHz has been extracted for the device at the initial balanced state. Then, a focussed ion beam (FIB) has been used to mill away some of the silicon of resonator 1, reducing its mass relative to resonator 2. After each incremental reduction in the mass of resonator 1, the amplitude ratio has been extracted so that a trend of amplitude ratio versus mass change can be established.

8.3 Focussed ion beam milling

Fig. 8.1 shows an SEM image of the coupled resonator device after the initial mass removal using the FIB. The ion milling has been performed by a Ga FIB with a beam energy of 30 keV and milling current between 1.5 nA and 3 nA. By visual inspection of SEM images from multiple angles, the volume of the removed silicon has been determined. Taking a value of 2331 kg/m^3 for the density of silicon, a calculation of the removed mass has been made. The initial mass removed is 2.1 ng, representing a relative mass change, $\Delta m/m$, of -0.0015. After the mass removal, the device is characterised using the previously described testing set-up. The amplitude ratio at the in-phase mode has been extracted for both k_c = -15.8 N/m and k_c = -8.88 N/m.

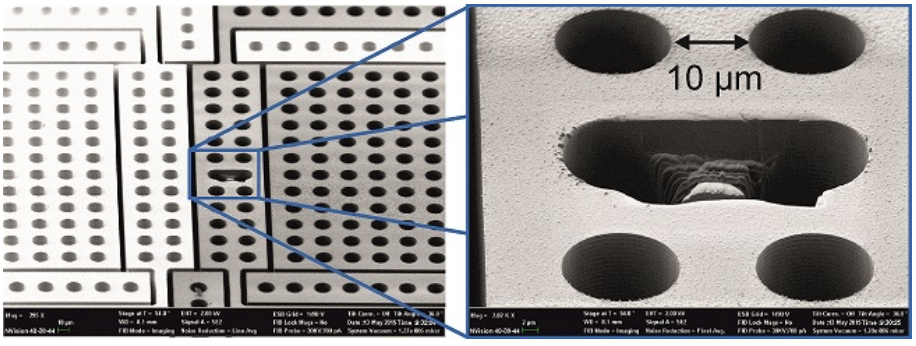

FIGURE 8.1: Initial mass removal for resonator 1 achieved using FIB milling. Visual inspection allowed for a calculation of the removed mass as 2.1 ng.

Two further sessions of ion milling have been performed to remove more silicon from resonator 1. The mass removed after the second session can be seen on the right of Fig. 8.2. The volume of material removed during the second session of FIB milling is

a much more clearly defined amount than the first session and the calculation of the removed mass has been simplified. The reason for the difference is that during the first session, the resonator moved during milling due to charging. For the second session, the ion beam has been directed at a new area of the resonator and the target area has been manually adjusted during the milling to correct for the movement of the resonator caused by charging. The result is a much more clearly defined volume of removed material. The two different volumes that have been removed after the two FIB milling sessions can be seen in Fig. 8.2. The mass of material removed during the second FIB milling session is 594 pg, bringing the total relative mass change, $\Delta m/m$, to -0.0019. Again, the amplitude ratio at the in-phase mode has been extracted for both k_c = -15.8 N/m and k_c = -8.88 N/m.

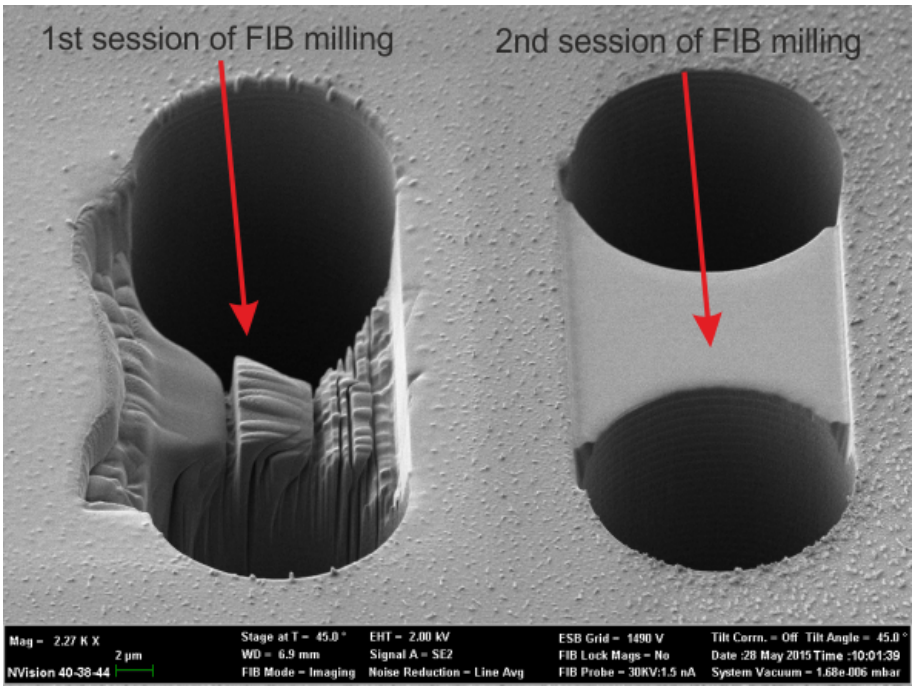

FIGURE 8.2: Mass removal for resonator 1 after second session of FIB milling. Visual inspection allowed for a calculation of the additional removed mass as 594 pg.

A third and final FIB milling sessions has been performed to remove material from resonator 1, followed by the measurement of the amplitude ratio. The same target area as the second mill has been used, with same manual adjustment performed during milling to compensate for the movement caused by charging. The result of the third FIB milling session has been the removal of an additional 469 pg, which brings the total relative mass change up to -0.0024.

8.4 Detection of mass change

As has been explained, the amplitude ratio at the in-phase mode has been extracted from the device after each mass removal. The results of the measurements, for both

k_c = -15.8 N/m and k_c = -8.88 N/m, have been plotted in Fig. 8.3. In addition to the experimental results, the theoretically derived response of the amplitude ratio to a decrease in mass of resonator 1, according to (3.33), has been plotted.

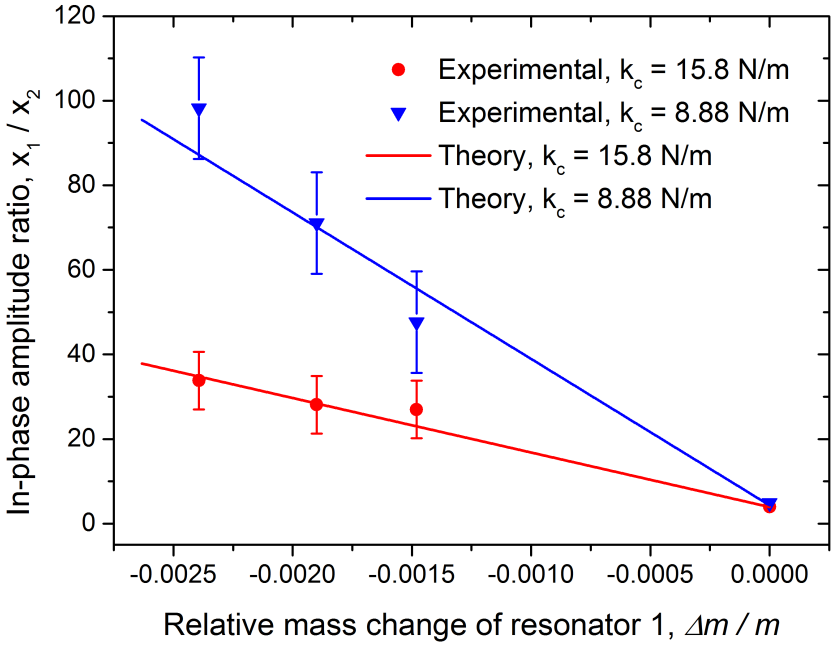

FIGURE 8.3: Theoretical and experimental response of the amplitude ratio at the in-phase mode to a mass change of resonator 1. Responses for two different coupling spring constants are shown with error bars representing uncertainty in the mass change.

It can be seen that the amplitude ratio response to a mass change of resonator 1 follows a linear trend, in accordance with the theoretical calculation. In addition, Fig. 8.3 shows that for a weaker coupling spring, the sensitivity of the amplitude ratio is increased. The sensitivity of the device has been calculated according to (3.34) for both values of coupling spring and is shown in Tab. 8.1.

Coupling spring, k_c (N/m)	Sensitivity, S_m
-15.8	12875
-8.88	34361

TABLE 8.1: Experimentally derived device sensitivities.

The shift of the in-phase mode frequency has been measured so as to determine the frequency sensitivity as defined by (2.7) of a 1-DOF resonator of the same design. The frequency sensitivity has been measured to be 0.203. Compared to the 1-DOF mass sensitivity, the amplitude ratio mass sensitivity of Tab. 8.1 shows up to five orders of magnitude increase.

Previously reported work [99] has demonstrated mode-localised mass sensing with a sensitivity of 6367. The sensitivity of the device characterised in this chapter is up to 5.4 times greater than the state of the art, showing its potential use as a biological or chemical mass sensor.

Similar to the minimum detectable stiffness change calculation performed in chapter 7, the signal-to-noise ratio of the output signal from each resonator has been calculated and then, using (7.1), the overall SNR has been calculated. With an SNR of 1.84 for a mass change of 469 pg, it can be concluded that the minimum detectable mass change is probably about 400 pg. While the value is larger than than previously reported devices (see Tab. 3.1), the superior sensitivity should be remembered and with further effort to reduce the noise, the device has the potential to be a superior mass sensor.

8.5 Conclusion

In this chapter, mass sensing by measuring the mode-localisation effect in an electrostatically coupled resonator pair has been demonstrated. The design of device that has been characterised is of the larger centre area design, with the reason for the architecture is to facilitate future biological or chemical mass sensing.

By removing mass from one of the resonator pair, an imbalance has been introduced to the coupled system, causing the amplitude ratio at the mode frequenters to change. Good agreement with the theoretical predicted trend has been achieved. By measuring the change in the amplitude ratio of the in-phase mode, it has been shown that the device can be used as a mass sensor. By decreasing the coupling spring strength, it has been shown that the sensitivity of the device can be improved. It has been shown that the device characterised in this chapter possesses a sensitivity that is 5.4 times greater than the best value reported in the literature.

Chapter 9

Conclusions and future work

The aim of the research that has been performed to enable the production of this thesis has been to improve the performance of sensors that are based on the mode-localisation effect in electrostatically-coupled MEMS resonator pairs. The research has focused on the design, fabrication and characterisation of various designs and dimensions of coupled MEMS resonator devices. The influence of the design and dimensions on the device sensitivity has been determined experimentally.

The fabrication of coupled MEMS resonator devices has been performed successfully using the facilities of the Southampton Nanofabrication Centre, demonstrating a new use for the SOI-based fabrication process that has only been used previously to create gyroscopes and accelerometers. For the 150 mm SOI wafer that has been processed, a yield of 95 % has been achieved. Also, the reliability of the process in preventing stiction has been proven successfully, as all the devices that have been tested exhibited resonant behaviour, with no need to test multiple devices to find a functional one.

Additional devices have been fabricated successfully using an alternative fabrication process, performed mostly at Northwestern Polytechnical University (NPU), Xi'an, China. The process differed in that the substrate below the suspended structures is not removed, which resulted in the occurrence of stiction in some of the devices. Consequently, a yield of approximately 30 % has been achieved, with more testing required to identify functional devices after completing the fabrication.

For all of the results, in order to facilitate comparison with previously published results, the definition of device sensitivity has been taken as the change in the amplitude ratio, x_1/x_2, of the resonators at the in-phase mode in response to a given relative stiffness change, $\Delta k/k$, or relative mass change, $\Delta m/m$, of one of the resonators.

A summary of all the results and conclusions presented in this thesis follows. Also, areas of future work that can build on the results that have been obtained for this thesis are suggested.

9.1 Results summary

The first design characterised has been a pair of electrostatically-coupled clamped-clamped beams. The width and length of the rectangular beams have been varied between the several designs that have been fabricated. It has been found that a 13 times improvement in stiffness sensitivity can be achieved by increasing the width of a 410 μm long resonator from 10 μm up to 20 μm. Additionally, it has been found that the beam length plays an important role in the sensitivity of the device, with a device with 410 μm long beams having double the sensitivity of a device with 510 μm long beams, while the width is maintained at 10 μm. The beam dimensions of the device with greatest stiffness sensitivity are 410 μm $\times$ 20 μm, with a sensitivity that is 2.8 times greater than the state-of-the-art.

The second design of coupled resonator that has been characterised consists of a rectangular block that is connected to the each of the two anchors with a beam. The main feature of the design is the larger surface area, which is intended to facilitate its use as a mass sensor, particularly as a biological sensor with the larger area providing more binding sites for the analyte of interest. Initially, the sensitivity to a stiffness perturbation has been determined, with the length of the anchor being varied between the devices. With the size of the centre block fixed at 310 μm $\times$ 60 μm, the length of the anchor beams has been found to influence the sensitivity of the device to a stiffness change of one the resonator pair. A 7 times improvement in sensitivity has been achieved for a device with 55 μm anchor beams compared to a device with 105 μm anchor beams. Varying the width of the centre block of the resonators did not have an appreciable impact on the stiffness sensitivity, indicating that the stiffness sensitivity is best altered through varying the anchor beam dimensions. The greatest stiffness sensitivity exhibited by a device of the larger centre area design has been found to be 3.26 times greater than the best value obtained for the simple rectangular beam devices. When compared to the state-of-the-art, a improvement of 9 times has been achieved.

The sensitivity for the coupled resonator devices has been shown to be higher if the mechanical stiffness of the resonators is higher. It should be noted that the vibration amplitude at the mode frequencies will be smaller for stiffer resonators, which will impact on the output signal and result in a smaller SNR. The device with the highest sensitivity, and therefore the smallest SNR, allowed for a measurement of a relative stiffness change of 0.8 ppm, which is an improvement on previously reported mode-localised stiffness sensors, which showed a resolution of 17 ppm.

The final design of coupled resonators has been fabricated with the fabrication process developed at NPU. A different design architecture consisting of a large mass anchored by four folded-beam anchors has been created. The stiffness of the resonators has been increased by shortening the length of the anchor beams from 240 μm down to 120 μm leading to a 1.42 times increase in stiffness sensitivity has been measured. Due to a

weaker coupling spring that resulted from an larger than designed coupling gap, it has been found that the devices show up to 5 times improvement in sensitivity compared to the other two device architectures fabricated with the Southampton process. Compared to the state-of-the-art, a 46 times improvement has been measured. However, the difference between the design and the fabricated device suggests that the fabrication process is less reliable. In addition, it should be noted that the fabrication process used to produce the devices has a much lower yield.

Finally, a coupled resonator device has been used to demonstrate mode-localised mass sensing. The design with the larger centre area has been used, as the architecture is intended to facilitate its use as a mass sensor. Using a focused ion beam, material has been removed in increments from one of the resonator pair. After each ion milling session to remove mass, the resulting change in amplitude ratio has been measured, which allows for the mass sensitivity of the coupled system to be calculated. Compared to the best value seen in the literature, the device fabricated and tested in this thesis shows a 5.4 times improvement in mass sensitivity.

In summary, this thesis has demonstrated the use of a high-yield dicing-free SOI-based process to fabricate electrostatically-coupled MEMS resonator pairs. The sensitivity of the amplitude ratio at the in-phase mode shape has been found to be up to 9 times greater than the state-of-art, with variations in device dimensions proving to be important. Other devices fabricated with an alternative SOI-based process showed stiffness sensitivity up to 46 times greater than the state-of-the-art, but with the drawback that the fabrication process is of a much lower yield and reliability Finally, mass sensing has been demonstrated with a coupled-resonator device, with a 5.4 times improvement over the best value in the literature.

9.2 Main conclusions

- Successful fabrication of a mode-localised sensor based on a pair of electrostatically-coupled MEMS resonators.
- Demonstration of a high-yield (> 90 %) fabrication process to produce coupled resonator devices.
- Variation of the device design and dimensions resulted in relative stiffness change sensitivity that is 9 times greater than the state-of-the-art and a resolution that allows for the measurement of a relative stiffness change of 0.8 ppm, superior to existing mode-localised sensors that have measured down to 17.6 ppm.
- Demonstration of mode-localised mass sensing with a sensitivity 5.4 times higher than the state-of-the-art. The minimum detectable mass, which is limited by the

noise, is 400 pg, which could be improved to a previously demonstrated value of 10 pg with future work to lessen the noise.

9.3 Future work

The devices that have been characterised for this thesis have been designed so that they may be utilised as biological or chemical mass sensors. In particular, the resonators with the larger centre area have been designed so as to provide more binding sites for the analyte that is to be measured.

However, for the mass sensing demonstration in this thesis, it has been shown that the resolution is large (pg scale), especially when compared to resonant frequency-shift based sensors (down to fg scale). Future development of the device could include miniaturisation to improve the sensitivity and the resolution. Improvements in the output circuitry could be designed that could reduce the noise in the output signal, which will improve the minimum detectable mass change.

The next step in the development of the sensors created in this thesis will be the functionalisation of the resonator surface with a material that will cause the analyte to immobilise there. For a sensor based on the mode-localisation effect in a pair of electrostatically coupled MEMS resonators, it is necessary to functionalise only one of resonators, which is a significant challenge. Solutions to the problem include the use of micro-pipettes to accurately dispense the functionalisation material onto one of the resonators. Also, an additional layer of gold over one of the resonators could enable its functionalisation using self-assembly.

Further improvements to the actuation and sensing circuitry could include the implementation of a self-oscillating feedback loop, which would eliminate the need for manually searching for the mode frequency of interest, as has been necessary for the experiments in this thesis. Combined with the superior sensitivity of the devices in this thesis, the future development of a feedback loop would allow for the creation of a new generation of MEMS-based sensors.

9.4 Publications

Parts of the work in this thesis have been published as:

G. S. Wood, C. Zhao, S. H. Pu, I. Sari, and M. Kraft. “An investigation of structural dimension variation in electrostatically-coupled MEMS resonator pairs using mode-localisation”, *IEEE Sensors Journal*, submitted.

G. S. Wood, C. Zhao, S.H. Pu, S. A. Boden, I. Sari, and M. Kraft. "Mass sensor utilising the mode-localisation effect in an electrostatically-coupled MEMS resonator pair fabricated using an SOI process", *Microelectronic Engineering*, vol. 159, pp. 169-173, 2016.

G. S. Wood, C. Zhao, S. H. Pu, I. Sari, and M. Kraft. "Sensor based on the mode-localization effect in electrostatically-coupled MEMS resonators fabricated using an SOI process", *Proceedings of the 14th IEEE Sensors Conference*, Nov. 2015.

G. S. Wood, S. H. Pu, C. Zhao, and M. Kraft. "Design of biological sensors utilising mode-localisation in electrostatically coupled microresonators", *Proceedings of the 23rd Micromechanics and Microsystems Europe Workshop*, Sep. 2012.

Bibliography

[1] A. C. Wong and C. T. C. Nguyen, "Micromechanical mixer-filters ("Mixlers")," *Journal of Microelectromechanical Systems*, vol. 13, no. 1, pp. 100–112, 2004.

[2] C. T.-C. Nguyen, "MEMS Technology for Timing and Frequency Control," *IEEE Transactions on Ultrasonics, Ferroelectrics, and Frequency Control*, vol. 54, no. 2, pp. 251–270, 2007.

[3] C. T. Leondes, *MEMS/NEMS Handbook*. Springer, 2006.

[4] J. F. Wu, G. K. Fedder, and L. R. Carley, "A low-noise low-offset capacitive sensing amplifier for a 50-microgram / root Hz monolithic CMOS MEMS accelerometer," *IEEE Journal of Solid-State Circuits*, vol. 39, no. 5, pp. 722–730, 2004.

[5] K. C. Schwab, "Putting Mechanics into Quantum Mechanics," *Physics Today*, vol. 58, no. 7, pp. 36–42, 2005.

[6] N. C. Tien, A. Ongkodjojo, R. C. Roberts, and D. Li, "The future of MEMS in energy technologies," in *9th International Conference on Solid-State and Integrated-Circuit Technology*, 2008.

[7] B. Ilic, Y. Yang, and H. G. Craighead, "Virus detection using nanoelectromechanical devices," *Applied Physics Letters*, vol. 85, no. 13, pp. 2604–2606, 2004.

[8] T. Adrega, D. M. F. Prazeres, V. Chu, and J. P. Conde, "Thin-film silicon MEMS DNA sensors," *Journal of Non-Crystalline Solids*, vol. 352, no. 9-20, pp. 1999–2003, 2006.

[9] H. Zhang, M. S. Marma, S. K. Bahl, E. S. Kim, and C. E. McKenna, "Sequence specific label-free DNA sensing using film-bulk-acoustic-resonators," *IEEE Sensors Journal*, vol. 7, no. 11-12, pp. 1587–1588, 2007.

[10] P. Thiruvenkatanathan, J. Woodhouse, J. Yan, and A. A. Seshia, "Manipulating Vibration Energy Confinement in Electrically Coupled Microelectromechanical Resonator Arrays," *Journal of Microelectromechanical Systems*, vol. 20, no. 1, pp. 157–164, 2011.

[11] P. W. Anderson, "Absence of Diffusion in Certain Random Lattices," *Physical Review*, vol. 109, no. 5, pp. 1492–1505, 1958.

[12] M. Spletzer, A. Raman, A. Q. Wu, X. F. Xu, and R. Reifenberger, "Ultrasensitive mass sensing using mode localization in coupled microcantilevers," *Applied Physics Letters*, vol. 88, no. 25, 2006.

[13] I. Sari, I. Zeimpekis, and M. Kraft, "A dicing free SOI process for MEMS devices," *Microelectronic Engineering*, vol. 95, pp. 121–129, 2012.

[14] J. Xie, Y. Hao, H. Chang, and W. Yuan, "Single Mask Selective Release Process for Complex SOI MEMS Devices," *Key Engineering Materials*, vol. 562–565, pp. 1116–1121, 2013.

[15] M. A. Cooper, *Label-Free Biosensors*. Cambridge University Press, 2009.

[16] D. Grech, K. S. Kiang, J. Zekonyte, M. Stolz, R. J. K. Wood, and H. M. H. Chong, "Highly linear and large spring deflection characteristics of a Quasi-Concertina MEMS device," *Microelectronic Engineering*, vol. 119, pp. 75–78, 2014.

[17] Z. Zhang, Y. Zhang, L. Liu, and T. Ren, "A Novel MEMS Pressure Sensor with MOSFET on Chip," in *2008 IEEE Sensors*, pp. 1564–1567, Oct. 2008.

[18] X. Yu, L. J. Wu, X. M. Zhang, and B. Li, "Interface Circuit Design and Implementation for MEMS Pressure Sensor in Tire Pressure Monitoring System," in *11th IEEE International Conference on Solid-State and Integrated Circuit Technology*, pp. 1284–1286, Oct. 2012.

[19] G. Fragiacomo, K. Reck, L. Lorenzen, and E. V. Thomsen, "Novel Designs for Application Specific MEMS Pressure Sensors," *Sensors*, vol. 10, no. 11, pp. 9541–9563, 2010.

[20] C. L. Cheng, H. C. Chang, C. I. Chang, Y. T. Tuan, and W. L. Fang, "Mechanical Force-Displacement Transduction Structure for Performance Enhancement of Cmos-Mems Pressure Sensor," in *27th IEEE International Conference on Micro-electromechanical Systems*, pp. 757–760, Jan. 2014.

[21] P. J. Chen, D. C. Rodger, E. Meng, M. S. Humayun, and Y. C. Tai, "Implantable unpowered parylene MEMS intraocular pressure sensor," in *International Conference on Microtechnologies in Medicine and Biology*, pp. 256–259, May. 2006.

[22] N. V. Lavrik, M. J. Sepaniak, and P. G. Datskos, "Cantilever transducers as a platform for chemical and biological sensors," *Review of Scientific Instruments*, vol. 75, no. 7, p. 2229, 2004.

[23] Z. A. Strong, A. W. Wang, and C. F. McConaghy, "Hydrogel-Actuated Capacitive Transducer for Wireless Biosensors," *Biomedical Microdevices*, vol. 4, no. 2, pp. 97–103, 2002.

[24] C. A. Grimes, D. Kouzoudis, K. G. Ong, and R. Cramp, "Thin-Film Magnetoelastic Microsensors for Remote Query Biomedical Monitoring," *Biomedical Microdevices*, vol. 2, no. 1, pp. 51–60, 1999.

[25] J. K. Gimzewski, C. Gerber, E. Meyer, and R. R. Schlittler, "Observation of a Chemical-Reaction Using a Micromechanical Sensor," *Chemical Physics Letters*, vol. 217, no. 5-6, pp. 589–594, 1994.

[26] R. Berger, C. Gerber, J. K. Gimzewski, E. Meyer, and H. J. Guntherodt, "Thermal analysis using a micromechanical calorimeter," *Applied Physics Letters*, vol. 69, no. 1, pp. 40–42, 1996.

[27] H. P. Lang, R. Berger, C. Andreoli, J. Brugger, M. Despont, P. Vettiger, C. Gerber, J. K. Gimzewski, J. P. Ramseyer, E. Meyer, and H. J. Guntherodt, "Sequential position readout from arrays of micromechanical cantilever sensors," *Applied Physics Letters*, vol. 72, no. 3, pp. 383–385, 1998.

[28] R. Raiteri, B. Margesin, and M. Grattarola, "An atomic force microscope estimation of the point of zero charge of silicon insulators," *Sensors and Actuators B: Chemical*, vol. 46, no. 2, pp. 126–132, 1998.

[29] R. Raiteri, M. Grattarola, H. J. Butt, and P. Skladal, "Micromechanical cantilever-based biosensors," *Sensors and Actuators B: Chemical*, vol. 79, no. 2–3, pp. 115–126, 2001.

[30] C. A. Savran, T. P. Burg, J. Fritz, and S. R. Manalis, "Microfabricated mechanical biosensor with inherently differential readout," *Applied Physics Letters*, vol. 83, no. 8, pp. 1659–1661, 2003.

[31] C. A. Savran, A. W. Sparks, J. Sihler, J. Li, W. C. Wu, D. E. Berlin, T. P. Burg, J. Fritz, M. A. Schmidt, and S. R. Manalis, "Fabrication and characterization of a micromechanical sensor for differential detection of nanoscale motions," *Journal of Microelectromechanical Systems*, vol. 11, no. 6, pp. 703–708, 2002.

[32] J. Fritz, M. K. Baller, H. P. Lang, H. Rothuizen, P. Vettiger, E. Meyer, H. J. Guntherodt, C. Gerber, and J. K. Gimzewski, "Translating biomolecular recognition into nanomechanics," *Science*, vol. 288, no. 5464, pp. 316–318, 2000.

[33] A. Subramanian, P. I. Oden, S. J. Kennel, K. B. Jacobson, R. J. Warmack, T. Thundat, and M. J. Doktycz, "Glucose biosensing using an enzyme-coated microcantilever," *Applied Physics Letters*, vol. 81, no. 2, pp. 385–387, 2002.

[34] M. A. Schmidt and R. T. Howe, "Silicon Resonant Microsensors," *14th Automotive Materials Conference: Ceramic Engineering and Science Proceedings*, vol. 8, no. 9-10, pp. 1019–1034, 1987.

[35] V. Kaajakari, *Practical MEMS*. Small Gear Publishing, 2009.

[36] L. Jiang, R. Cheung, M. Hassan, A. J. Harris, J. S. Burdess, C. A. Zorman, and M. Mehregany, "Fabrication of SiC microelectromechanical systems using one-step dry etching," *Journal of Vacuum Science and Technology B*, vol. 21, no. 6, pp. 2998–3001, 2003.

[37] K. L. Ekinci, Y. T. Yang, and M. L. Roukes, "Ultimate limits to inertial mass sensing based upon nanoelectromechanical systems," *Journal of Applied Physics*, vol. 95, no. 5, pp. 2682–2689, 2004.

[38] L. Jiang, M. Hassan, R. Cheung, A. J. Harris, J. S. Burdess, C. A. Zorman, and M. Mehregany, "Dry release fabrication and testing of SiC electrostatic cantilever actuators," *Microelectronic Engineering*, vol. 78-79, pp. 106–111, 2005.

[39] S. Kon, K. Oldham, and R. Horowitz, "Piezoresistive and piezoelectric MEMS strain sensors for vibration detection," *Sensors and Smart Structures Technologies for Civil, Mechanical, and Aerospace Systems*, vol. 6529, pp. U901–U911, 2007.

[40] C. Comi, A. Corigliano, G. Langfelder, A. Longoni, A. Tocchio, and B. Simoni, "A High Sensitivity Uniaxial Resonant Accelerometer," in *23rd IEEE International Conference on Microelectromechanical Systems*, pp. 260–263, Jan. 2010.

[41] A. Tocchio, A. Caspani, G. Langfelder, A. Longoni, and E. Lasalandra, "Resolution and Start-up Dynamics of MEMS Resonant Accelerometers," in *2011 IEEE Sensors*, pp. 161–164, Oct. 2011.

[42] A. Tocchio, A. Caspani, G. Langfelder, A. Longoni, and E. Lasalandra, "A Pierce Oscillator for MEMS Resonant Accelerometer with a novel Low-Power Amplitude Limiting Technique," in *2012 IEEE International Frequency Control Symposium*, May. 2012.

[43] U. Park, J. Rhim, J. U. Jeon, and J. Kim, "A micromachined differential resonant accelerometer based on robust structural design," *Microelectronic Engineering*, vol. 129, pp. 5–11, 2014.

[44] A. A. Seshia, M. Palaniapan, T. A. Roessig, R. T. Howe, R. W. Gooch, T. R. Schimert, and S. Montague, "A vacuum packaged surface micromachined resonant accelerometer," *Journal of Microelectromechanical Systems*, vol. 11, no. 6, pp. 784–793, 2002.

[45] T. A. Roessig, R. T. Howe, A. P. Pisano, and J. H. Smith, "Surface-micromachined resonant accelerometer," in *International Conference on Solid-State Sensors and Actuators (Transducers)*, pp. 859–862, Jun. 1997.

[46] D. W. Burns, R. D. Horning, W. R. Herb, J. D. Zook, and H. Guckel, "Sealed-cavity resonant microbeam accelerometer," *Sensors and Actuators A: Physical*, vol. 53, no. 1-3, pp. 249–255, 1996.

[47] Y. L. Shang, J. B. Wang, S. Tu, and D. Y. Chen, "A Novel Micromachined Differential Resonant Accelerometer with Flexural Mechanisms Fabricated by SOI-MEMS Technology," in *2011 IEEE Sensors*, pp. 165–168, Oct. 2011.

[48] D. R. Myers and A. P. Pisano, "Torque measurements of an automotive halfshaft utilizing a MEMS resonant strain gauge," in *15th IEEE International Conference on Solid-State Sensors, Actuators and Microsystems (Transducers)*, pp. 1726 – 1729, Jun. 2009.

[49] S. P. Beeby, G. Ensell, B. R. Baker, M. J. Tudor, and N. M. White, "Micromachined silicon resonant strain gauges fabricated using SOI wafer technology," *Journal of Microelectromechanical Systems*, vol. 9, no. 1, pp. 104–111, 2000.

[50] K. E. Wojciechowski, B. E. Boser, and A. P. Pisano, "A MEMS resonant strain sensor operated in air," in *17th IEEE International Conference on Microelectromechanical Systems*, pp. 841–845, Jan. 2004.

[51] K. E. Wojciechowski, B. E. Boser, and A. P. Pisano, "A MEMS resonant strain sensor with 33 nano-strain resolution in a 10 kHz bandwidth," in *2005 IEEE Sensors*, pp. 947–950, Oct. 2005.

[52] R. G. Azevedo, D. G. Jones, A. V. Jog, B. Jamshidi, D. R. Myers, L. Chen, X. A. Fu, M. Mehregany, M. B. J. Wijesundara, and A. P. Pisano, "A SiC MEMS resonant strain sensor for harsh environment applications," *IEEE Sensors Journal*, vol. 7, no. 3-4, pp. 568–576, 2007.

[53] R. G. Azevedo, W. Huang, O. M. O'Reilly, and A. P. Pisano, "Dual-mode temperature compensation for a comb-driven MEMS resonant strain gauge," *Sensors and Actuators A: Physical*, vol. 144, no. 2, pp. 374–380, 2008.

[54] M. Chan, D. R. Myers, B. Sosnochik, L. Lin, and A. P. Pisano, "Localized strain sensing using high spatial resolution, highly-sensitive MEMS resonant strain gauges for failure prevention," in *16th International Conference on Solid-State Sensors, Actuators and Microsystems (Transducers)*, Jun. 2011.

[55] M. Ferri, F. Mancarella, L. Belsito, A. Roncaglia, J. Yan, A. A. Seshia, K. Soga, and J. Zalesky, "Strain sensing on steel surfaces using vacuum packaged MEMS resonators," in *Eurosensors XXIV*, vol. 5, pp. 1426–1429, Sep. 2010.

[56] Y. Chuan and G. Can, "Investigation based on MEMS double Si3N4 resonant beams pressure sensor," in *5th IEEE International Conference on Nano/Micro Engineered and Molecular Systems*, pp. 5 – 8, Jan. 2010.

[57] Y. Chuan and G. Can, "Structure design on MEMS TiN resonant pressure sensors," in *5th IEEE International Conference on Nano/Micro Engineered and Molecular Systems*, pp. 30 – 33, Jan. 2010.

[58] Z. Luo, D. Chen, J. Wang, and J. Chen, "A differential resonant barometric pressure sensor using SOI-MEMS technology," in *2013 IEEE Sensors*, pp. 1–4, Nov. 2013.

[59] Y. X. Li, D. Y. Chen, and J. B. Wang, "Stress Isolation Used In MEMS Resonant Pressure Sensor Package," in *Eurosensors XXV*, vol. 25, Sep. 2011.

[60] T. Ishida, V. N. Quet, S. Mochizuki, Y. Kagawa, T. Takayama, and T. Omata, "MEMS whistle-type temperature-compensated displacement sensor using resonant frequency shift," *Sensors and Actuators A: Physical*, vol. 222, pp. 24–30, 2015.

[61] E. Mehdizadeh, M. Rostami, X. B. Guo, and S. Pourkamali, "Atomic Resolution Disk Resonant Force and Displacement Sensors for Measurements in Liquid," *IEEE Electron Device Letters*, vol. 35, no. 8, pp. 874–876, 2014.

[62] E. Mehdizadeh, X. Guo, S. Pourkamali, A. Hajjam, and A. Rahafrooz, "Nanoprecision force and displacement measurements using MEMS resonant structures," in *2013 IEEE Sensors*, pp. 1–4, Nov. 2013.

[63] G. Binnig, H. Rohrer, C. Gerber, and E. Weibel, "7x7 Reconstruction on Si(111) Resolved in Real Space," *Physical Review Letters*, vol. 50, no. 2, pp. 120–123, 1983.

[64] U. Dürig, J. K. Gimzewski, and D. W. Pohl, "Experimental-Observation of Forces Acting during Scanning Tunneling Microscopy," *Physical Review Letters*, vol. 57, no. 19, pp. 2403–2406, 1986.

[65] T. R. Albrecht, P. Grutter, D. Horne, and D. Rugar, "Frequency-Modulation Detection Using High-Q Cantilevers for Enhanced Force Microscope Sensitivity," *Journal of Applied Physics*, vol. 69, no. 2, pp. 668–673, 1991.

[66] P. Girard, G. C. Solal, and S. Belaidi, "Observation of voltage contrast in non-contact resonant mode atomic force microscopy," *Microelectronic Engineering*, vol. 31, no. 1-4, pp. 215–225, 1996.

[67] M. Hoummady and E. Farnault, "Enhanced sensitivity to force gradients by using higher flexural modes of the atomic force microscope cantilever," *Applied Physics A: Materials Science and Processing*, vol. 66, pp. S361–S364, 1998.

[68] J. A. Harley and T. W. Kenny, "A high-stiffness axial resonant probe for atomic force microscopy," *Journal of Microelectromechanical Systems*, vol. 10, no. 3, pp. 434–441, 2001.

[69] J. Le Rouzic, B. Cretin, P. Vairac, and B. Cavallier, "Specific geometries of resonant cantilevers for Scanning Force Microscopy," in *2009 Joint Meeting of the European Frequency and Time Forum and the IEEE International Frequency Control Symposium*, pp. 822–825, Apr. 2009.

[70] G. Douchet, F. Sthal, E. Bigler, R. Bourquin, and T. Leblois, "Resonant Langasite Microsensor for Atomic Force Microscopy," in *2009 Joint Meeting of the European Frequency and Time Forum and the IEEE International Frequency Control Symposium*, pp. 826–830, Apr. 2009.

[71] Y. T. Yang, C. Callegari, X. L. Feng, K. L. Ekinci, and M. L. Roukes, "Zeptogram-scale nanomechanical mass sensing," *Nano Letters*, vol. 6, no. 4, pp. 583–586, 2006.

[72] J. Chaste, A. Eichler, J. Moser, G. Ceballos, R. Rurali, and A. Bachtold, "A nanomechanical mass sensor with yoctogram resolution," *Nature Nanotechnology*, vol. 7, no. 5, pp. 301–304, 2012.

[73] A. Gupta, D. Akin, and R. Bashir, "Single virus particle mass detection using microresonators with nanoscale thickness," *Applied Physics Letters*, vol. 84, no. 11, pp. 1976–1978, 2004.

[74] A. Gupta, J. P. Denton, H. McNally, and R. Bashir, "Novel fabrication method for surface micromachined thin single-crystal silicon cantilever beams," *Journal of Microelectromechanical Systems*, vol. 12, no. 2, pp. 185–192, 2003.

[75] A. Gupta, D. Akin, and R. Bashir, "Detection of bacterial cells and antibodies using surface micromachined thin silicon cantilever resonators," *Journal of Vacuum Science & Technology B: Microelectronics and Nanometer Structures*, vol. 22, no. 6, pp. 2785–2791, 2004.

[76] K. Y. Gfeller, N. Nugaeva, and M. Hegner, "Micromechanical oscillators as rapid biosensor for the detection of active growth of Escherichia coli.," *Biosensors & Bioelectronics*, vol. 21, no. 3, pp. 528–533, 2005.

[77] K. Y. Gfeller, N. Nugaeva, and M. Hegner, "Rapid biosensor for detection of antibiotic-selective growth of Escherichia coli," *Applied and Environmental Microbiology*, vol. 71, no. 5, pp. 2626–2631, 2005.

[78] A. Bietsch, J. Zhang, M. Hegner, H. P. Lang, and C. Gerber, "Rapid functionalization of cantilever array sensors by inkjet printing," *Nanotechnology*, vol. 15, no. 8, pp. 873–880, 2004.

[79] B. Ilic, D. Czaplewski, H. G. Craighead, P. Neuzil, C. Campagnolo, and C. Batt, "Mechanical resonant immunospecific biological detector," *Applied Physics Letters*, vol. 77, no. 3, pp. 450–452, 2000.

[80] T. P. Burg, A. R. Mirza, N. Milovic, C. H. Tsau, G. A. Popescu, J. S. Foster, and S. R. Manalis, "Vacuum-packaged suspended microchannel resonant mass sensor for biomolecular detection," *Journal of Microelectromechanical Systems*, vol. 15, no. 6, pp. 1466–1476, 2006.

[81] A. P. Davila, J. Jang, A. K. Gupta, T. Walter, A. Aronson, and R. Bashir, "Microresonator mass sensors for detection of Bacillus anthracis Sterne spores in air and water.," *Biosensors & Bioelectronics*, vol. 22, no. 12, pp. 3028–3035, 2007.

[82] Y. Lee, G. Lim, and W. Moon, "A self-excited micro cantilever biosensor actuated by PZT using the mass micro balancing technique," *Sensors and Actuators A-Physical*, vol. 130, pp. 105–110, 2006.

[83] T. Xu, Z. Wang, J. Miao, L. Yu, and C. M. Li, "Micro-machined piezoelectric membrane-based immunosensor array.," *Biosensors & Bioelectronics*, vol. 24, no. 4, pp. 638–643, 2008.

[84] Y. Xiao, Y. Liu, G. Borg, R. L. Withers, Z. Li, Z. Xu, and C. M. Li, "Lead magnesium niobate-lead titanate piezoelectric immunosensors," *Sensors and Actuators A: Physical*, vol. 163, no. 1, pp. 82–87, 2010.

[85] J. Pepper, R. Noring, M. Klempner, B. Cunningham, A. Petrovich, R. Bousquet, C. Clapp, J. Brady, and B. Hugh, "Detection of proteins and intact microorganisms using microfabricated flexural plate silicon resonator arrays," *Sensors and Actuators B: Chemical*, vol. 96, no. 3, pp. 565–575, 2003.

[86] O. H. Willemsen, M. M. E. Snel, A. Cambi, J. Greve, B. G. D. Grooth, and C. G. Figdor, "Biomolecular interactions measured by atomic force microscopy," *Biophysical Journal*, vol. 79, no. 6, pp. 3267–3281, 2000.

[87] G. U. Lee, D. A. Kidwell, and R. J. Colton, "Sensing Discrete Streptavidin Biotin Interactions with Atomic-Force Microscopy," *Langmuir*, vol. 10, no. 2, pp. 354–357, 1994.

[88] Y. S. Lo, N. D. Huefner, W. S. Chan, F. Stevens, J. M. Harris, and T. P. Beebe, "Specific interactions between biotin and avidin studied by atomic force microscopy using the Poisson statistical analysis method," *Langmuir*, vol. 15, no. 4, pp. 1373–1382, 1999.

[89] O. H. Willemsen, M. M. E. Snel, K. O. van der Werf, B. G. D. Grooth, J. Greve, P. Hinterdorfer, H. J. Gruber, H. Schindler, Y. van Kooyk, and C. G. Figdor, "Simultaneous height and adhesion imaging of antibody-antigen interactions by atomic force microscopy," *Biophysical Journal*, vol. 75, no. 5, pp. 2220–2228, 1998.

[90] R. Merkel, P. Nassoy, A. Leung, K. Ritchie, and E. Evans, "Energy landscapes of receptor-ligand bonds explored with dynamic force spectroscopy," *Nature*, vol. 397, no. 6714, pp. 50–53, 1999.

[91] R. Ros, F. Schwesinger, D. Anselmetti, M. Kubon, R. Schafer, A. Pluckthun, and L. Tiefenauer, "Antigen binding forces of individually addressed single-chain Fv antibody molecules," *Proceedings of the National Academy of Sciences of the United States of America*, vol. 95, no. 13, pp. 7402–7405, 1998.

[92] C. H. Hodges and J. Woodhouse, "Vibration Isolation from Irregularity in a Nearly Periodic Structure - Theory and Measurements," *Journal of the Acoustical Society of America*, vol. 74, no. 3, pp. 894–905, 1983.

[93] P. Thiruvenkatanathan, J. Yan, and A. A. Seshia, "Common mode rejection in electrically coupled MEMS resonators utilizing mode localization for sensor applications," *2009 Joint Meeting of the European Frequency and Time Forum and the IEEE International Frequency Control Symposium*, pp. 358–363, 2009.

[94] C. Zhao, G. S. Wood, J. Xie, H. Chang, S. H. Pu, and M. Kraft, "A force sensor based on three weakly coupled resonators with ultrahigh sensitivity," *Sensors and Actuator A: Physical*, vol. 232, pp. 151–162, 2015.

[95] M. Spletzer, A. Raman, H. Sumali, and J. P. Sullivan, "Highly sensitive mass detection and identification using vibration localization in coupled microcantilever arrays," *Applied Physics Letters*, vol. 92, no. 11, 2008.

[96] P. Thiruvenkatanathan, J. Yan, J. Woodhouse, and A. A. Seshia, "Enhancing Parametric Sensitivity in Electrically Coupled MEMS Resonators," *Journal of Microelectromechanical Systems*, vol. 18, no. 5, pp. 1077–1086, 2009.

[97] P. Thiruvenkatanathan, J. Yan, and A. A. Seshia, "Differential Amplification of Structural Perturbations in Weakly Coupled MEMS Resonators," *IEEE Transactions on Ultrasonics, Ferroelectrics, and Frequency Control*, vol. 57, no. 3, pp. 690–697, 2010.

[98] P. Thiruvenkatanathan, J. Woodhouse, J. Yan, and A. A. Seshia, "Limits to mode-localized sensing using micro- and nanomechanical resonator arrays," *Journal of Applied Physics*, vol. 109, no. 10, 2011.

[99] P. Thiruvenkatanathan, J. Yan, J. Woodhouse, A. Aziz, and A. A. Seshia, "Ultrasensitive mode-localized mass sensor with electrically tunable parametric sensitivity," *Applied Physics Letters*, vol. 96, no. 8, 2010.

[100] P. Thiruvenkatanathan, J. Yan, and A. A. Seshia, "Ultrasensitive Mode-Localized Micromechanical Electrometer," *2010 IEEE International Frequency Control Symposium*, pp. 91–96, 2010.

[101] P. Thiruvenkatanathan and A. A. Seshia, "Mode-localized Displacement Sensing," *Journal of Microelectromechanical Systems*, vol. 21, no. 5, 2012.

[102] Coventor, "Coventorware 2012 user manual," 2012.